FERROELECTRET NANOGENERATOR (FENG) FOR MECHANICAL ENERGY HARVESTING AND SELF-POWERED FLEXIBLE ELECTRONICS

By

Wei Li

A DISSERTATION

Submitted to
Michigan State University
in partial fulfillment of the requirements
for the degree of

Mechanical Engineering – Doctor of Philosophy

2017

ABSTRACT

FERROELECTRET NANOGENERATOR (FENG) FOR MECHANICAL ENERGY HARVESTING AND SELF-POWERED FLEXIBLE ELECTRONICS

By

Wei Li

Harvesting energy from our natural environment has been the focus of multiple research efforts in the past decades. Progress in this field has far-reaching implications for the growing environment problems resulting from greenhouse gas emission of fossil fuels. Furthermore, advances in portable energy scavenging devices will shed light on the development of self-powered and autonomous electronics; which will impact a broad range of applications in wireless sensors, biomedical implants, infrastructure monitoring, and portable/wearable electronics. This thesis research explores the designs, fabrications, simulations, characterizations and applications of flexible thin film nanogenerator based energy harvesting technologies. Materials and designs for flexible nanogenerator based on nanocrystalline aluminum nitride (AlN) thin film are reported. AlN nanoparticles were grown on aluminum layer by pulsed laser deposition (PLD) at room temperature. Piezoresponse force microscopy (PFM) indicates that their electromechanical energy conversion metrics are as high as highly c-axis oriented AlN or ZnO thin film. Polyimide thin film encapsulated the entire structure of flexible nanogenerator to further improve mechanical robustness, protecting the device from invasive chemicals and enhance its potential biocompaibility. Besides, this thesis research introduces polypropylene ferroelectret (PPFE) as the active material in an efficient, flexible, and biocompatible ferroelectret nanogenerator (FENG) device. PPFE is a type of charged polymers with empty voids and inorganic particles that create giant dipoles across the material's thickness. The mechanical-electrical energy conversion mechanism in PPFE films is verified by finite element method (FEM). Investigation of the developed device shows that the magnitudes of the generated voltage and current signals are doubled each time the device

is folded, and an increase with magnitude or frequency of the mechanical input is observed. The developed FENGs is sufficient to light twenty commercial green and blue light-emitting diodes (LEDs), and realize a self-powered liquid-crystal display (LCD) that harvests energy from user's touch. A self-powered flexible/foldable keyboard is also demonstrated. Furthermore, this thesis reports the device's intrinsic properties which allow for the bi-directional conversion of energy between electrical and mechanical domains; thus extending its potential use in wearable electronics beyond the power generation realm. This electromechanical coupling, combined with their flexibility and thin film-like form, bestows dual-functional transducing capabilities to the device that are used in this research to demonstrate its use as a thin, wearable, and self-powered loudspeaker or microphone patch. To determine the device's performance and applicability, sound pressure level is characterized in both space and frequency domains for three different configurations. The confirmed device's high performance is further validated through its integration in three proposed systems: a music-playing flag, a sound recording film, and a flexible microphone for security applications.

To my family and friends, for their unconditional support.

ACKNOWLEDGMENTS

Many people deserve my heart-felt thanks for their great helps during my Ph.D. study in United States. First and foremost, I would like to express my sincere thanks to my advisor, Dr. Nelson Sepúlveda, for his visionary guidance, continuous inspiration, enduring support and encouragement, meticulous care and attention. For me, studying aboard to pursue my second Ph.D. degree alone in United States is not that easy. From the first day I came to United States, to last day I finish Ph.D. study, I've spent almost all my time doing research in university without having any vacations back to hometown and visiting parents. Luckily, I have such a great advisor who give me endless love, making me feel home-like warmth in this lovely lab. Whenever I experienced hard time during research, Dr. Sepúlveda's wisdom, kindness, enthusiasm, mindset, charisma are shining forth as a beacon of light amidst the chaos. His words have been deeply impacting on me and his acts set such a high standard which I would never be able to catch up. It's my great honor to join Dr. Sepúlveda's wonderful research group.

Besides, I owe a great debt of gratitude to my thesis committee: Dr. Peter Lillehoj, Dr. Chuan Wang and Dr. Junghoon Yeom (in alphabetical order of last name), for their invaluable supervision and generous supports. I feel so honored to have you as my committee. Furthermore, I am deeply obliged to Dr. Zhong Lin Wang from Georgia Institute of Technology, Atlanta, for our pleasant cooperation.

I would like to thank my fellow labmates in this lovely group: David Torres, Tongyu Wang (Tony), Yunqi Cao (Steven), Rafmag Cabrera and José Figueroa for all the fun we enjoy together; I would also like to thank fellows in Dr. Chuan Wang's lab: Le Cai, Suoming Zhang and Jinshui Miao for their selfless assistance.

Last but not least, I would like to thank my spiritual pillar of hardworking – my parents: Siqing Li and Qiangwei Pan. Spending years on pursuing another Ph.D. degree in United

States is one of most critical decisions that I've made in my life. My parents give me a hundred percent support no matter what decision I make and always encourage me to follow my heart. Their unconditional loves have been giving me courage to optimistically face any challenges in my life.

TABLE OF CONTENTS

LIST OF TABLES

LIST OF FIGURES

CHAPTER 1

INTRODUCTION

Within human society when complexity increases there is a matching rise in energy use and, as we can see all around us, modern civilization is becoming more complex by the day. With the increased energy usage, mankind has more power to alter the environment around to produce more food, build bigger and better shelters, and devote more time to leisure. As the anthropologist Leslie White once wrote "the degree of cultural development varies directly as the amount of energy per capita per year put to work"[1].

For all mankind's 50,000 year history, the utilization of energy has been closely linked to the level of civilization. For most of it, the only source of energy human could draw upon was the most basic – human or animal muscle. Near the end of 18th century, in a wave of unprecedented innovation and advancement, Europeans began to unlock the potential of fossil fuels. All these new fossil-fuel based technologies unleashed creative energies and allowed an exponential increase in the populations, as well as the standards of living in industrialized society. Later, the 20th century witnessed the amplification of those trends, with rapid improvements in technology and exponential increases in energy consumption in every field.

However, fossil fuels burn inefficiently, which produce a lot of pollutants and toxins. Fossil fuels are the largest source of carbon dioxide – a greenhouse gas which contributes to climate change, and their production causes both environmental and human health impacts. But, it's not only that. It will come as a surprise to no one that fossil fuel is a finite resource – it's only a matter of when they run out – not if.

Sustainable, environmentally benign energy can be derived from two way – nuclear fission or captured from ambient sources. In the early 1970s, when the war in the Middle East caused oil prices to skyrocket worldwide, nuclear energy ushered its finest hour. Subsequently, the

Three Mile Island nuclear plant accident in 1979, the Chernobyl nuclear catastrophe in 1986 and the Fukushima Daiichi nuclear disaster in 2011 sparked globally violent controversy on nuclear plant. As anti-nuclear movement has been sweeping the world, more and more people have been joining the anti-nuclear protest and demonstration. As of 2016, industrialized countries such as Australia, Austria, Denmark, Greece, New Zealand, and Norway have no nuclear power stations and remain opposed to nuclear power. Germany, Italy, Spain, Sweden and Switzerland are phasing-out nuclear power. Globally, more nuclear power reactors have closed than opened in recent years [2, 3, 4].

In contrast, renewable energy resources are constantly replenished and will never run out. Renewable energy is the energy that is generated from natural processes which are continuously replenished, such as sunlight, wind, geothermal heat, tides, water, and various forms of biomass [5]. Large-scale ambient energy (e.g. solar, wind and tide) is widely available and technologies are being developed to efficiently capture it. Since renewable energy cannot be exhausted and is constantly renewed, it has been continuing its rapid growth, providing multiple benefits to human society. A new high of $329 billion U.S. dollar for global renewable energy was invested in 2015 [6, 7, 8]. At the other end of the scale, there are also small amounts of wasted energy that could be useful if captured. Recovering even a fraction of this energy would have both economic and environmental impact. The technologies of scavenging energy from ambient environment can also be used for the development of self-powered electronics by greatly extending the lifetime of batteries, so as to supply power to the devices or sensor networks in the case when renewing batteries are beset by difficulties.

1.1 Development of Energy Harvesting

1.1.1 Basis of Energy Harvesting

Energy harvesting is the process by which energy is derived from external sources (e.g. solar power, wind energy, thermal energy, salinity gradients, and kinetic energy, also known as

ambient energy), captured, and stored for autonomous devices, like those used in wearable electronics and wireless sensor networks. Energy harvesting materials and systems have become a prominent research area and keeps growing at rapid pace. A wide range of applications are targeted for the energy harvesters, including distributed wireless sensor nodes for structural health monitoring, embedded or implanted sensor nodes for medical applications, recharging the batteries of large systems, powering unmanned vehicles, monitoring tire pressure in automobiles, and running security systems in household conditions. Recent development includes the components and devices at micro-macro scales covering materials, electronics, and integration [7]. Energy harvesting technologies have a huge potential for replacing batteries of small, low power electronic devices, which have several benefits [8]:

- *Maintenance free* – no need to replace batteries;
- *Environmentally friendly* – disposal of batteries is tightly regulated because they contain chemicals and metals that are harmful to the environment and hazardous to human health;
- *Opens up new applications* – such as deploying energy harvesting sensors to monitor remote or underwater locations.

Developing energy harvesting technology requires expertise from various aspects of physics, including: energy capture (sporadic, irregular energy rather than sinusoidal), energy storage, metrology, material science, systems engineering. Generally speaking, there are five representative energy sources in the environment – mechanical energy, thermal energy, chemical energy, solar energy, and nuclear energy, which are all represented in various forms, as shown in Figure 1.1.

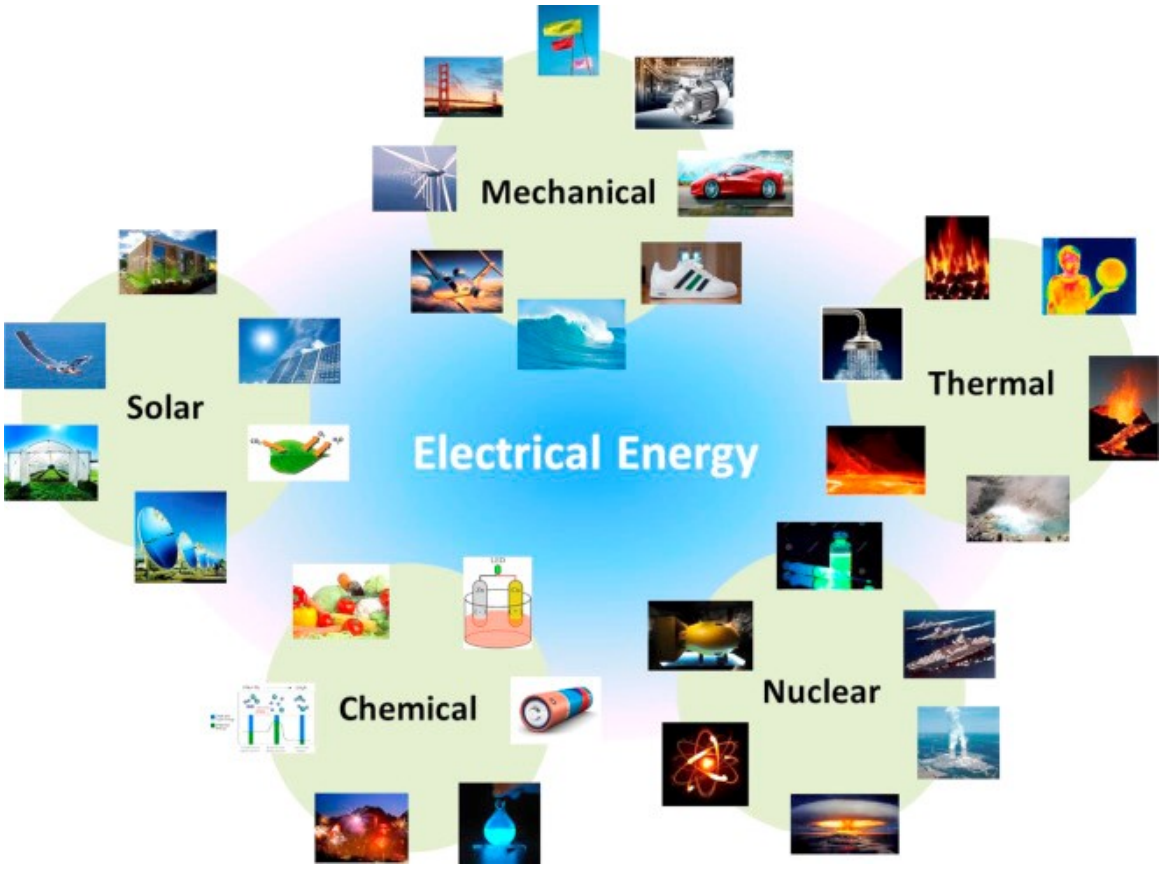

Figure 1.1 Various available energy sources in the environment and their representative forms. [9]

1.1.2 Methods to Harvesting Energy

For harvesting ambient energy from different sources, a variety of device based on different physic principle are proposed. There are five typical physical principles are employed for the development of energy harvesters.

1.1.2.1 Electromagnetic Energy Harvesting

Electromagnetic energy harvesters are able to harvest energy by using rotational or linear devices. A typical example is SEIKO Kinetic watch which can generate electricity from the kinetic movement of the wearer's wrist. The design consists of a rotating pendulum mass, a gear box train with a ratio of 1:100, and a small permanent magnet generator,

as shown in Figure 1.2. The motion from wearer provides a rate of change of flux, which results in some induced electromotive force on the coils. The concept is simply related to Faraday's Law. According to Paradiso and Starner [10], 5-10 μW of power was estimated to be produced when the watch was worn, and 1 mW could be obtained when it was forcibly shaken [10, 11]. This electricity is stored in a self-recharging battery which needs much less frequent replacement than the conventional cell battery in a quartz watch.

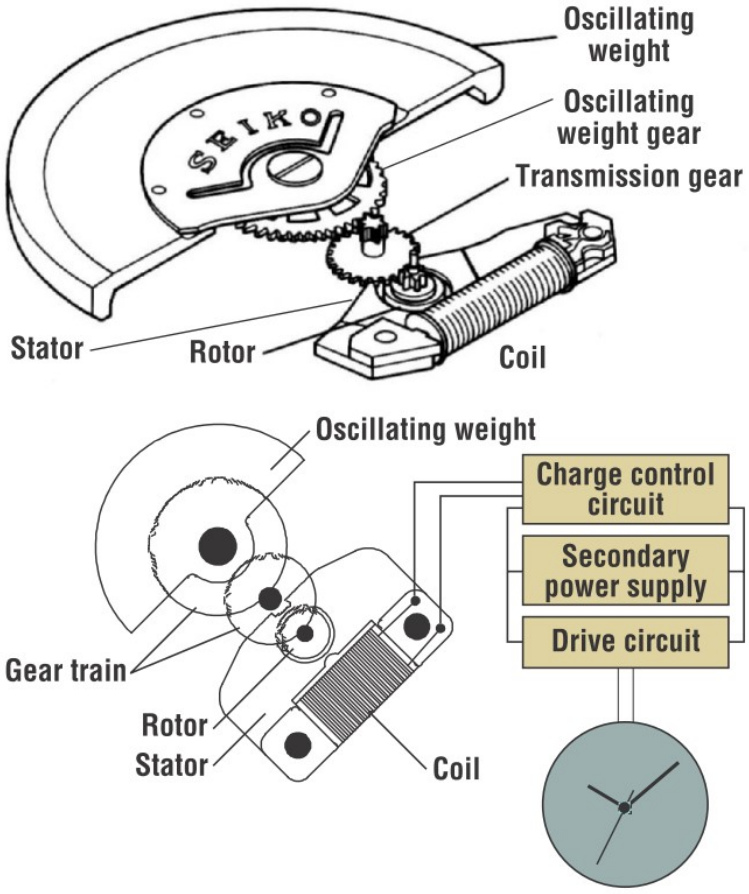

Figure 1.2 Seiko AGS (Automatic Generating System) generator for the Kinetic series. [10]

1.1.2.2 Photovoltaics

Photovoltaics is a technology involving the direct conversion of solar radiation into electricity using solar cells. Interest in photovoltaics has grown dramatically in many countries over the past decade, with worldwide photovoltaic sector growth since 1997 ranging from 30% to

58% [12]. A solar cell is essentially a specialized semiconductor diode with a large barrier layer which, when exposed to light, allows for direct conversion into direct current electricity of a portion of the energy in the photons arriving at the cell, as shown in Figure 1.3.

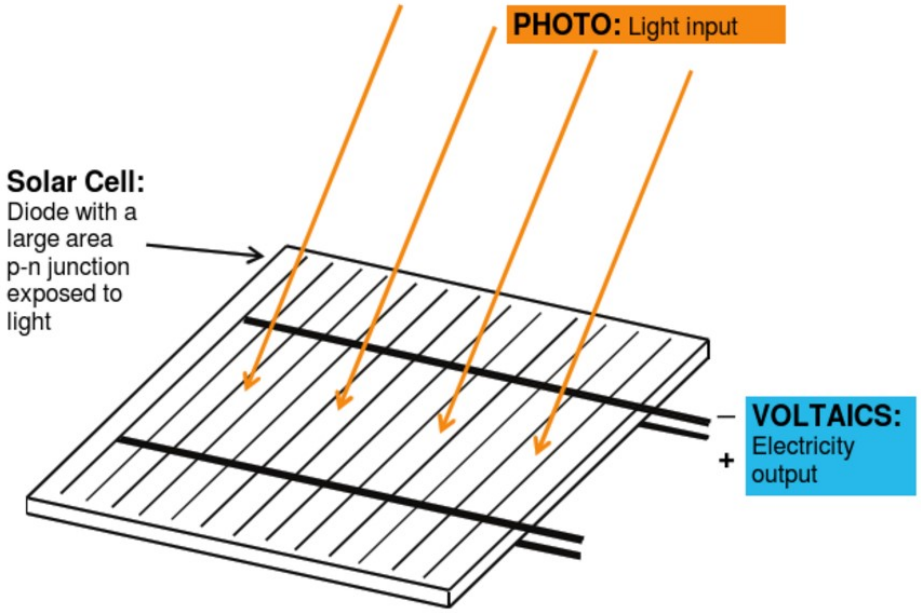

Figure 1.3 Solar cells convert light into electricity. [12]

1.1.2.3 Thermoelectric Generator

Environments that naturally contain temperature gradients and heat flow have the potential to generate electrical power using thermal-to-electric energy conversion. The temperature difference provides the potential for efficient energy conversion, while heat flow provides the power. For systems with low-power requirements (e.g. remote wireless sensors) , or those direct waste heat (e.g. automobile exhaust), thermoelectric energy harvesting would be a viable technology and promise to become more prevalent as the power requirements for such applications. Figure 1.4 show a typical thermoelectric device based on Seebeck effect.

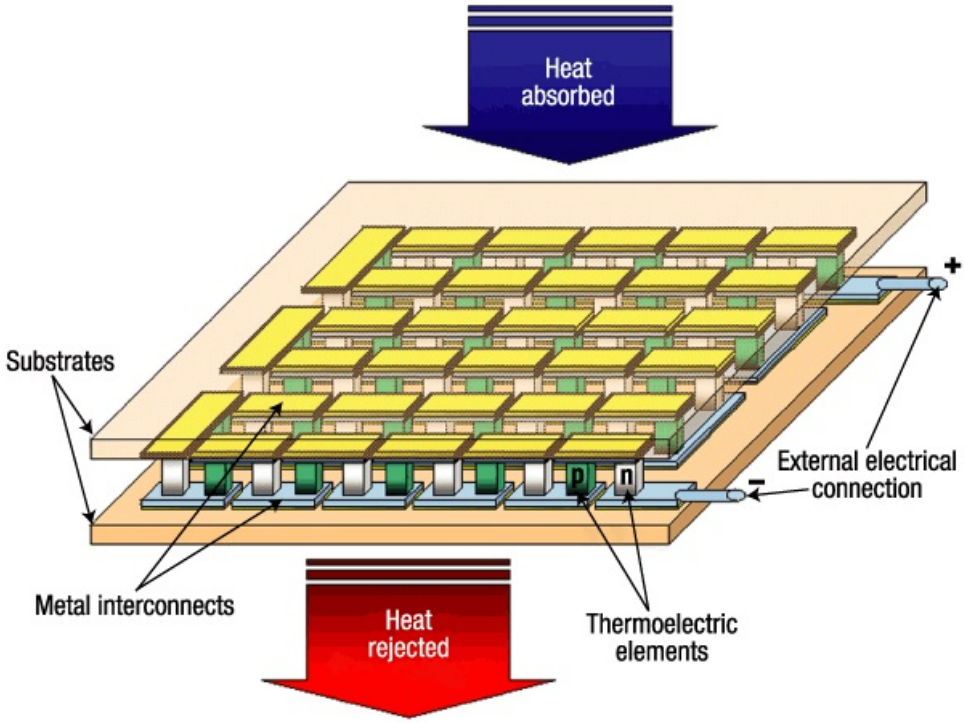

Figure 1.4 A typical thermoelectric device based on Seebeck effect. [13]

1.1.2.4 Electrostatic Generator

Electrostatic generator consists of a charged capacitor with moving plates. Unlike magnetic generators, electrostatic generator needs to be "jump-started" with an initial voltage before producing power. Because the force between the electrodes of capacitor increases with the square of the applied voltage, the generated electrical energy correspondingly increases as more charge is loaded onto the capacitor. Electrostatic generator tends to be small (often MEMS-scale) device, where it benefits significantly from being able to increase energy density with applied voltage [14]. Figure 1.5 shows such a MEMS-scale electrostatic generators.

1.1.2.5 Piezoelectric Energy Harvester

Piezoelectricity, whose prefix "piezo" in Greek means to press or squeeze, translates to "electricity from pressure". Piezoelectric materials exhibit two reversible piezoelectric effects:

- *Direct piezoelectric effect* – Internal generation of electrical charge resulting from an

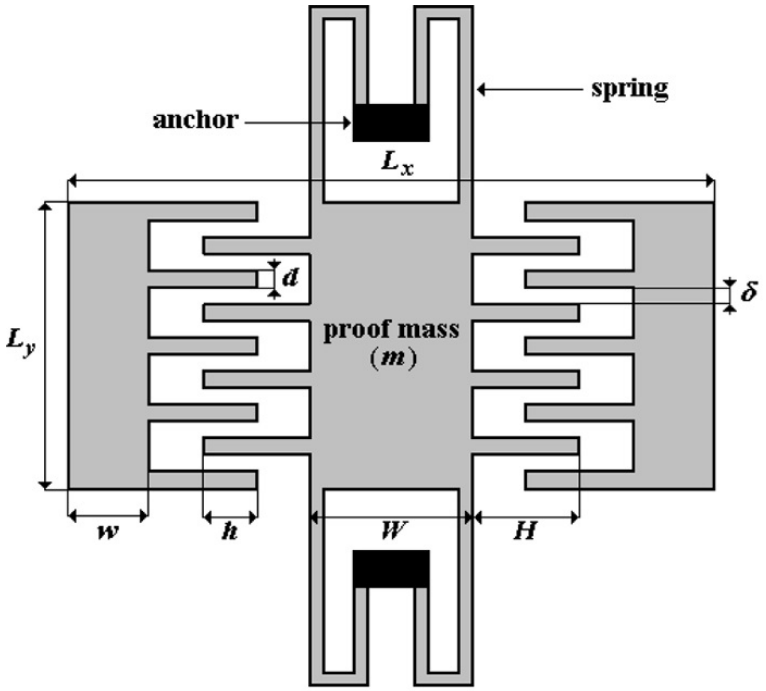

Figure 1.5 A typical MEMS electrostatic generator. [15]

applied mechanical force;

- *Reverse piezoelectric effect* – Internal generation of a mechanical strain resulting from an applied electrical field.

Piezoelectric energy harvester takes advantage of the direct piezoelectric effect, which allows a mechanical force to be applied to the material to deform it slightly and the material will then produce an output electric power. This is achieved by rearranging the dipoles of the piezoelectric material, which causes a change in the dipole density and therefore a change in the electric field between the dipoles. Because of this change in the electric field, the piezoelectric material produces an output electric power. Basic structures of piezoelectric energy harvesters are shown in Figure 1.6.

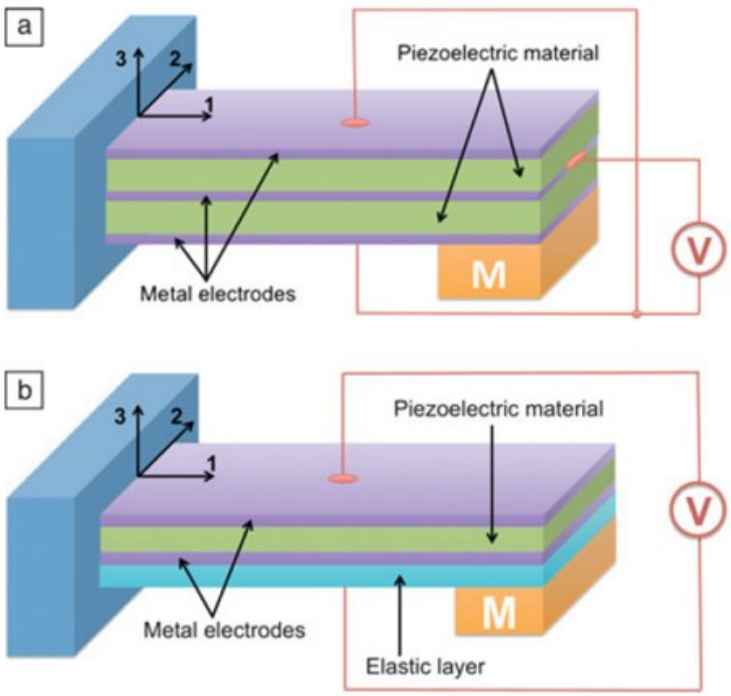

Figure 1.6 Basic structures of piezoelectric energy harvesters. (a) Bimorph structure. (b) Unimorph structure [16]

1.2 Outline

The remaining of this dissertation is organized as follows: in Chapter 2, related background literature supporting the main work of the dissertation is reviewed; in Chapter 3, development of a flexible nanogenerator based on nanocrystalline aluminum nitride (AlN) thin films developed at room temperature by pulsed laser deposition (PLD) is reported; in Chapter 4, a different operating mechanism to the field of flexible thin film nanogenerators based on Ferroeletret nanogenerators (FENGs) which is able to harvest mechanical energy from human motion is introduced; in Chapter 5, a dual-functional and self-powered thin film flexible acoustic transducer, which operates as both loudspeaker and microphone is reported; finally, Chapter 6 summarizes the contributions of this work, and gives possible investigations of future research.

CHAPTER 2

BACKGROUND

Mechanical energy is ubiquitous day and night in our daily life – on the one hand, they are shown in some violent and enormous ways, such as tidal wave, fierce gales, seismic wave, skyscrapers or bridges' vibration; on the other hand, they can be found in tiny and sometimes even unnoticed forms, such as human walking, light breeze, rotating tires, keyboard typing. Even simple body movement [17, 18, 19] or biological functions (e.g. heartbeats or diaphragm activities [20, 21, 22, 23, 24]) involve mechanical energy that has recently been tapped as renewable energy sources. The development of flexible nanogenerators that enables mechanical-to-electrical energy conversion not only could yield breakthroughs in active wearable or implantable biomedical devices which rely on battery power for diagnostics or operation, but also has a potentially bright prospects of using ocean wave or wind energy to supply power in a low-cost, simple and practical way.

This chapter presents related background literatures supporting the main work of the dissertation. First, the idea of developing flexible nanogenerator based on piezoelectric inorganics with flexible substrate is presented. PZT, ZnO and AlN are the typical piezoelectric inorganics which are detailed reviewed respectively. Besides, three different type of pieoelectric polymer – bulk piezoelectric polymer, piezoelectric polymer composite, and voided charged polymer, which can be directly used as an active material in a variety of transduction applications are also presented. In addition, this chapter gives an overview of one of the most prestigious nanogenerator – triboelectric nanogenerator (TENG).

2.1 Piezoelectric Inorganics with Flexible Substrate

2.1.1 PZT-based Energy Harvesting

Lead zirconatetitanate ($PbZr_{0.52}Ti_{0.48}O_3$, PZT) is an intermetallic inorganic compound showing a remarkable piezoelectric effect. Owing to its large piezoelectric and electromechanical coupling coefficients, high dielectric permittivity and significant remnant polarization [25], PZT has been widely used in a variety of practical applications such as ultrasonic transducers [26], MEMS devices [27], precision actuators [28], as well as pressure [29] and strain sensors [30],

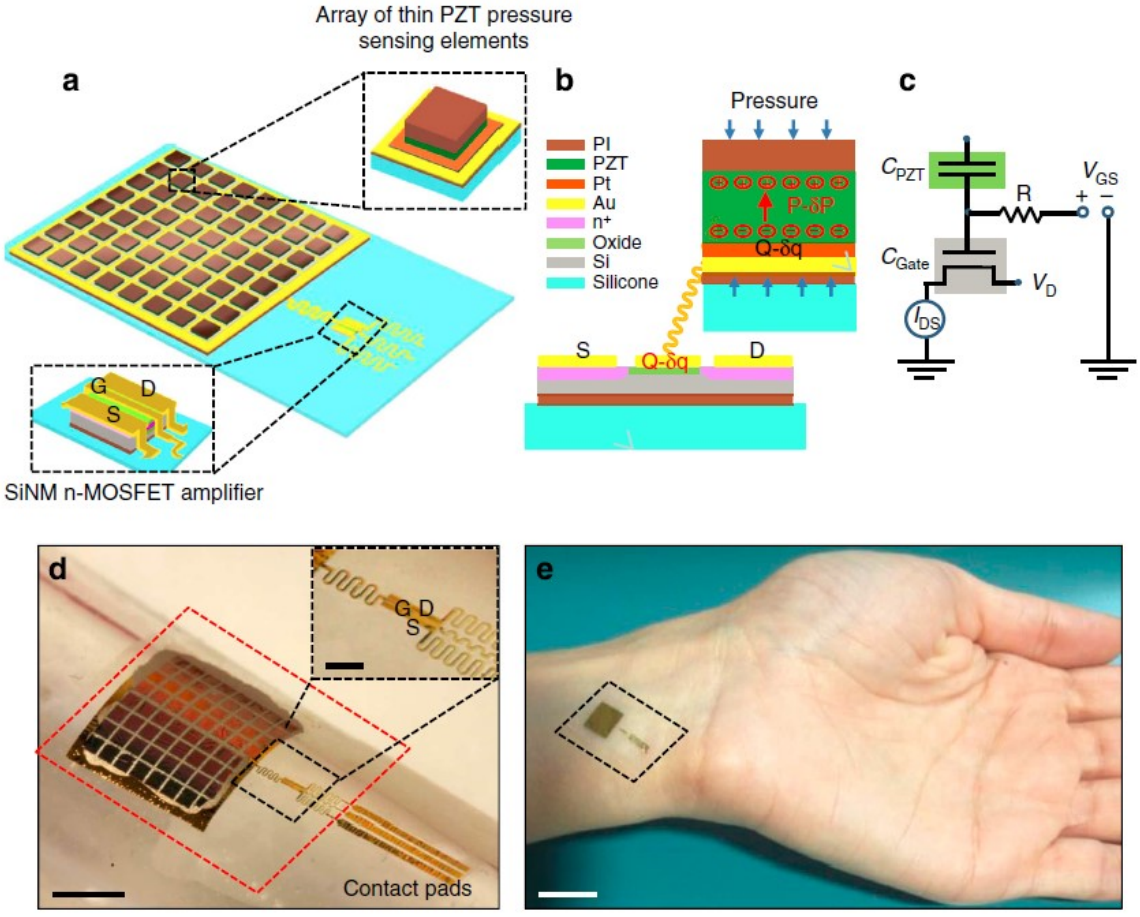

Figure 2.1 Schematic illustrations and photographs of a thin conformable piezoelectric pressure sensor. (a) Illustration of the device. (b) Cross-sectional schematic illustration. (c) Equivalent circuit. (d) Photograph of a device wrapped on a cylindrical glass support. Scale bar, 5 mm. (e) Photograph of a device laminated on a wrist. Scale bar, 2 cm. [31]

Dagdeviren et al. [31] reported inorganic materials, heterogeneous designs and theoretical models for an ultrathin, compact device which is capable of softly laminating on the skin. Ultrathin (400 nm) sheets of high-quality PZT serve as the active components of capacitor-type structures that connect to the gate electrodes of MOSFETs based on nanomembranes of silicon (SiNMs). The developed small ($\sim$ 1 cm^2), lightweight (2 mg), thin (25 μm) systems are capable of stretching (to $\sim$ 30%), with system-level effective modulus ($\sim$ 60 kPa) to conform to the skin, while providing high levels of pressure sensitivity ($\sim$ 0.005 Pa), fast response times ($\sim$ 0.1 ms), low hysteresis, superior operational stability and excellent fatigue properties. The developed thin conformable piezoelectric pressure sensor is shown in Figure 2.1.

Chen et al. [32] demonstrated a piezoelectric nanogenerator based on PZT nanofibers with a diameter and length of approximately 60 nm and 500 μm, respectively. The peak output voltage from this nanogenerator was 1.63 V, and the output power was 0.03 μW with a load resistance of 6 MΩ. The piezoelectric voltage constant and dielectric constant of PZT nanofibers were much higher than those of the semiconductor type of piezoelectric nanowires or nanofibers, allowing this material for nanogenerator or nanobattery applications. Besides, the flexible PZT nanofibers were embedded into a soft polydimethylsiloxane (PDMS) polymer matrix, which prevent the PZT nanofibers from being damaged so as to extending its life cycle. The simple fabrication and assembly process would allow for the facile mass production of this type of nanogenerator. Schematic illustrations and power generation mechanism of this developed PZT nanofiber generator are shown in Figure 2.2.

Park et al. [33] reported a highly-efficient, lightweight, flexible, and large-area piezoelectric PZT thin film nanogenerator. By adopting the laser lift-off (LLO) process, the entire area of a flexible PZT thin film obtained by sol-gel method with a subsequent crystallization step at 650 °C was transferred to a plastic substrate from a sapphire substrate without any mechanical damage. During periodical bending/unbending motions, the measured output voltage and current signals reached up to $\sim$ 200 V and 150 μA cm^{-2}, respectively, showing

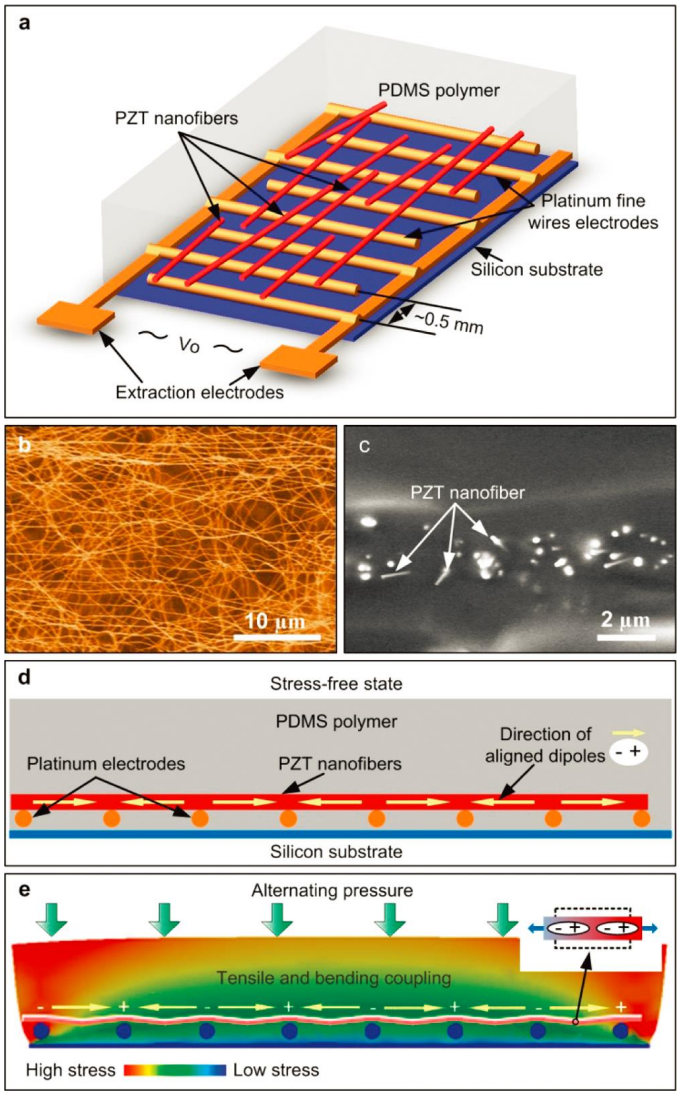

Figure 2.2 Schematic illustrations and power generation mechanism of the PZT nanofiber generator. (a) Schematic illustration. (b) Scanning electron microscopy (SEM) image of the PZT nanofiber mat across the interdigitated electrodes. (c) Cross-sectional SEM image. (d) Cross-sectional schematic illustration. (e) Schematic view explaining the power out mechanism. [32]

outstanding output performance. The high energy sources harvested from a large-area thin film NG (3.5 cm × 3.5 cm) by irregular human finger motions were used directly to light LEDs without any external electric sources and circuits. The schematic illustration of the fabrication steps of flexible PZT thin film nanogenerator using the LLO process is shown in Figure 2.3.

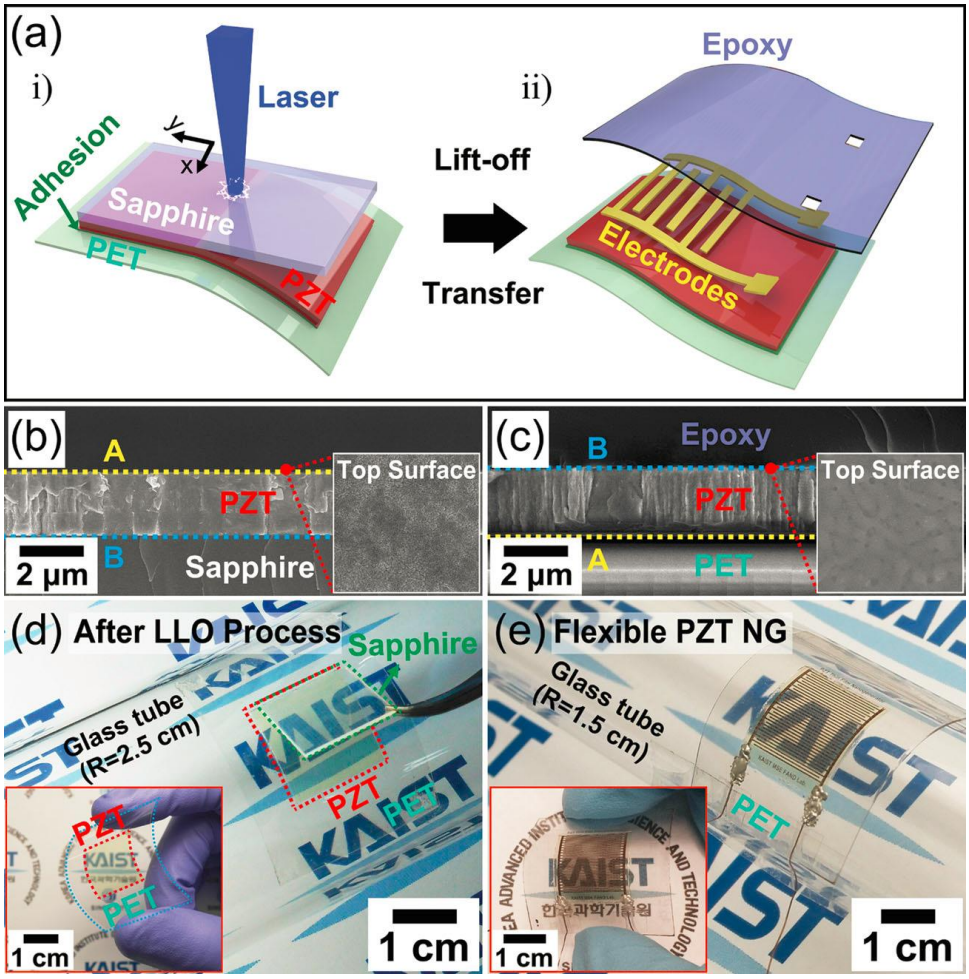

Figure 2.3 Schematic illustrations and photographs of flexible PZT thin film nanogenerator. (a) Schematic illustration of fabrication process. (b, c) Cross-sectional SEM images of PZT thin film on (b) Sapphire and (c) PET substrate. (d) A PZT thin film (1.5 cm × 1.5 cm) on a PET substrate being detached from a sapphire substrate after LLO process. (e) Final flexible PZT thin film NG attached to a glass tube and bent by human fingers. [33]

Qi et al. [34] reported an approach to implementing crystalline piezoelectric PZT ribbons with micrometer-scale widths and nanometer scale thicknesses on rubber substrate over large areas for flexible energy conversion. PZT films were first grown on a (100)-cleaved MgO crystal substrate and then postannealed to form the perovskite crystal substrate. Next, the film were patterned into nanothick ribbons and printed onto PDMS via dry transfer. The fundamental piezoelectric properties of the device were characterized on the rubber substrate using a nanoscale characterization method – piezoresponse force microscopy (PFM). It's

shown that these flexible piezo-assemblies were particularly efficient electromechanical energy converters for wearable or even implantable energy harvesters. Schematic illustrations and photograph of the printing process is shown in Figure 2.4.

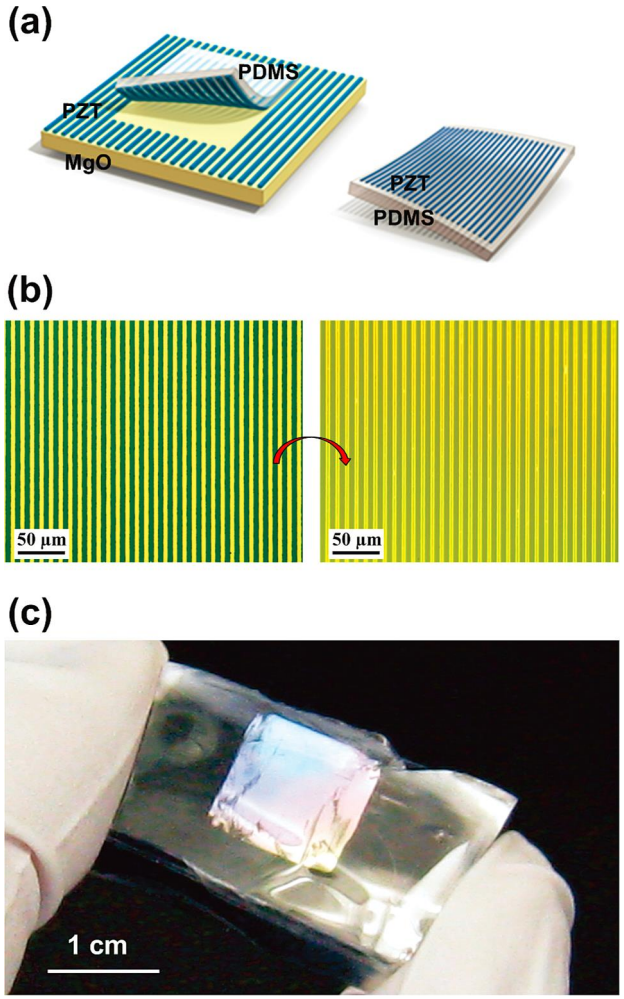

Figure 2.4 Schematic illustrations and photograph of printing process of PZT ribbons onto flexible rubber substrate. (a) Crystalline PZT ribbons are synthesized on an MgO host substrate which is subsequently etched, and the ribbons are transfer printed onto flexible PDMS rubber. (b) Optical micrograph of PZT ribbons before and after transferring. (c) Photograph of a piece of PDMS with PZT ribbons covering the top surface. [34]

Dagdeviren et al. [35] consequently reported devices that enable high-efficiency mechanical-to-electrical energy conversion from natural contractile and relaxation motions of organs(e.g. heart, lung, and diaphragm), demonstrated in several different animal models, each of which has organs with sizes that approach human scales. A cointegrated collection of such energy-

harvesting elements with rectifiers and microbatteries provided an entire flexible system, which is capable of viable integration with the beating heart via medical sutures and operation with efficiencies of $\sim 2\%$. Schematic illustrations and photograph of the flexible mechanical energy harvester based on thin ribbons of PZT are shown in Figure 2.5.

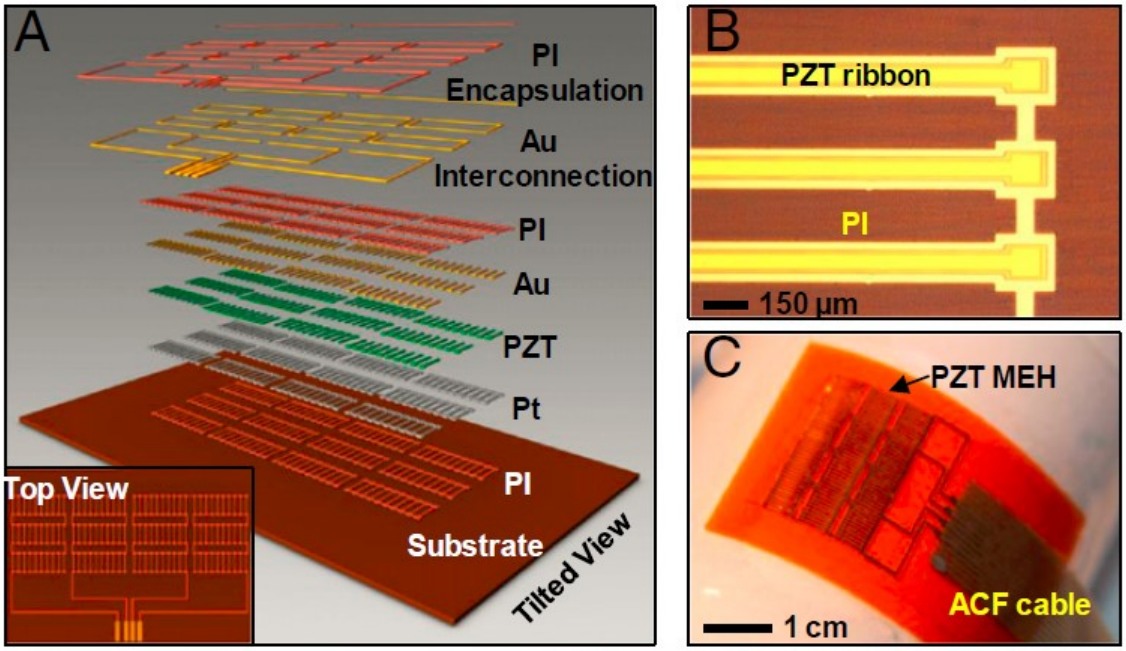

Figure 2.5 Flexible mechanical energy harvester based on thin ribbons of PZT. (a) Exploded-view schematic illustration with a top view (Inset). (b) Optical microscope image of PZT ribbons printed onto a thin film of polyimide. (c) Photograph of a flexible PZT mechanical energy harvester with cable for external connection. [35]

Dagdeviren et al. [36] further introduced a set of materials and device designs that allow for *in vivo* measurements of viscoelasticity in the near-surface regions of the epidermis through the use of ultrathin, stretchable networks of mechanical actuators and sensors constructed with nanoribbons of PZT. Applications *in vitro* with mock and *ex vivo* skin preparations under varying conditions and *in vivo* on human subjects, collected at various locations over all main regions of body, under both normal conditions. The thin, compliant modulus sensor based on nanoribbons of PZT and *ex vivo* and *in vivo* measurements on human subjects are shown in Figure 2.5.

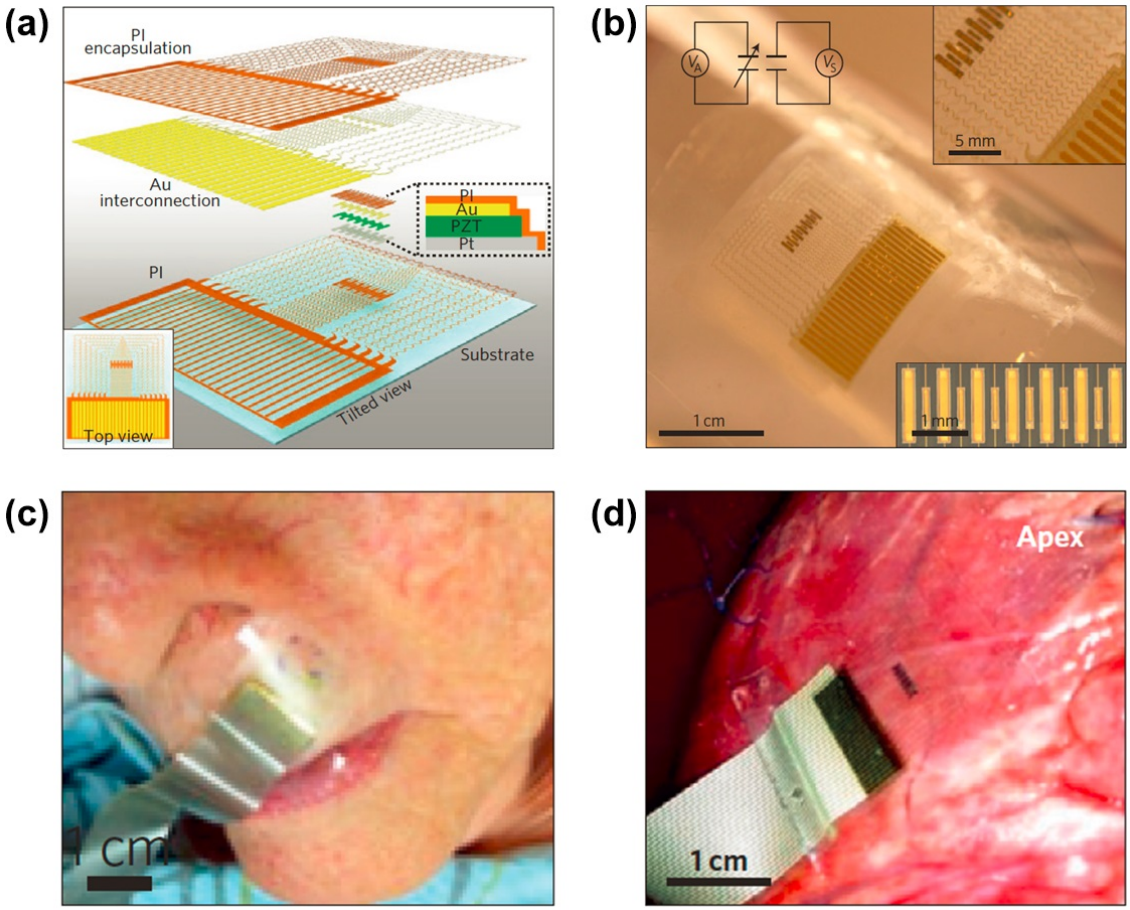

Figure 2.6 Thin, compliant modulus sensor based on nanoribbons of PZT and ex vivo and in vivo measurements on human subjects. (a) Exploded-view schematic illustration of the device, with a top view (inset). (b) Photograph of a device on a thin silicon substrate. (c) Photograph of a device placed on human skin near nose. (d) Photograph of a device placed on bovine heart. [36]

2.1.2 ZnO-based Energy Harvesting

The technology of ZnO-based piezoelectric nanogenerator, which was first proposed in 2006 by Prof. Wang et al. [37], converts random mechanical energy into electric energy by using piezoelectric ZnO nanowires, which can be triggered by tiny physical motions and work in a large frequency range. At the beginning, focuses were on the science behind this phenomenon for bringing this technology from a scientific concept into practical applications [38, 39, 40, 41, 42]. It took several years to increase the open-circuit voltage from the original 9 mV to over 1 V [43, 44, 45, 46]. The sophisticated device fabrication process

prevented the further development of this technology until a new device design based on a sandwich structure was proposed, by which high performance piezoelectric nanogenerator can be achieved with greatly simplified fabrication process and high mechanical stability by utilizing ZnO nanowires.

Xu et al. [44] reported a vertical and lateral integration of ZnO nanowires into arrays which are able to produce sufficient power for operating real devices. A lateral integration of 700 rows of ZnO nanowires produced a peak voltage of 1.26 V at a strain of 0.19%, which is potentially sufficient to recharge a battery. In a separate device, a vertical integration of three layers of ZnO nanowire arrays produces a peak power density of 2.7 mW/cm^3. The vertically integrated nanogenerator is used to power a nanowire pH sensor and nanowire UV sensor, so as to demonstrate a self-powered system composed entirely of nanowires. Fabrication steps of vertical nanowire array integrated nanogenerator is shown in Figure 2.7.

Zhu et al. [47] developed a type of integrated nanogenerator based on arrays of vertically aligned piezoelectric ZnO nanowires. The peak open-circuit voltage and short-circuit current reach a high level of 58 V and 134 μA, respectively, with a maximum power density of 0.78 W/cm^3. The generated electric signal was directly applied to a sciatic nerve of a frog, including innervation of the nerve. Vibrant contraction of the frog's gastrocnemius muscle was observed resulting from the instantaneous electric signal produced by the nanogenerator. Structure of the vertically aligned ZnO nanowires nanogenerator is shown in Figure 2.8.

Pradel et al. [48] demonstrated the applicability of ZnO homojunction nanostructures for enhanced mechanical energy harvesting. The optimum materials design was found by systematically designing and testing different material configurations and treatments. The depletion region formed at the p-n homojunction effectively reduces internal screening of strain-induced polarization charges by free carriers in both n-ZnO and Sb-doped p-ZnO, allowing for significantly enhanced piezoelectric output compared to a single layer device. The device was able to detect small-scale subdermal movement from the tendons in the human wrist and distinguish different motions and hand gestures, making it possible for

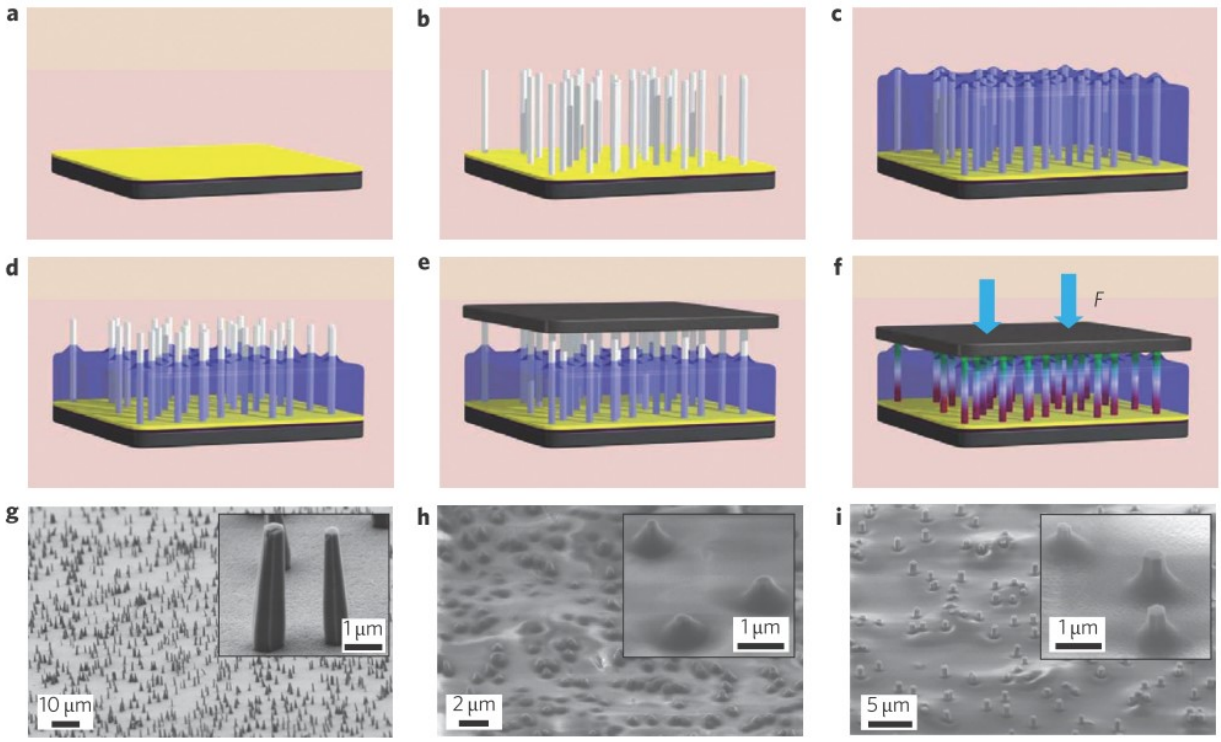

Figure 2.7 Fabrication steps of vertical nanowire array integrated nanogenerator. (a) Gold-coated silicon wafer. (b) ZnO nanowire arrays grown by low-temperature hydrothermal decomposition. (c) PMMA is deposited by spin coating. (d) Oxygen plasma etching. (e) A platimun-coated flat electrode is placed on top of the nanowires. (f) Nanowires are under compression. (g) SEM images of the as-grown ZnO nanowire arrays on the substrate. (h) SEM image after spin-coating with PMMA. (i) SEM image after oxygen plasma etching. [44]

the control of embedded electronics and sensors for intelligent and adaptive operations in human. Homojunction nanogenerator grown in the p-n configuration on silicone rubber for gesture recognition by measurement of flexor movement are shown in Figure 2.9.

Lee et al. [49] proposed a device composed of ZnO nanowires and polyvinylidene fluoride (PVDF) polymer around a conducting fiber, which is a hybridization of two piezoelectric materials. The ZnO nanowires served as a piezoelectric-potential generator and as an additive to enhance the surface-contact area in order to guide the formation of a uniform layer of piezoelectric polymer around the fiber during the dip-coating process. The PVDF polymer plays multiple roles, such as in the piezoelectric ensemble with the ZnO nanowires and as a protective material for high durability under deformation. Experiments reveals that me-

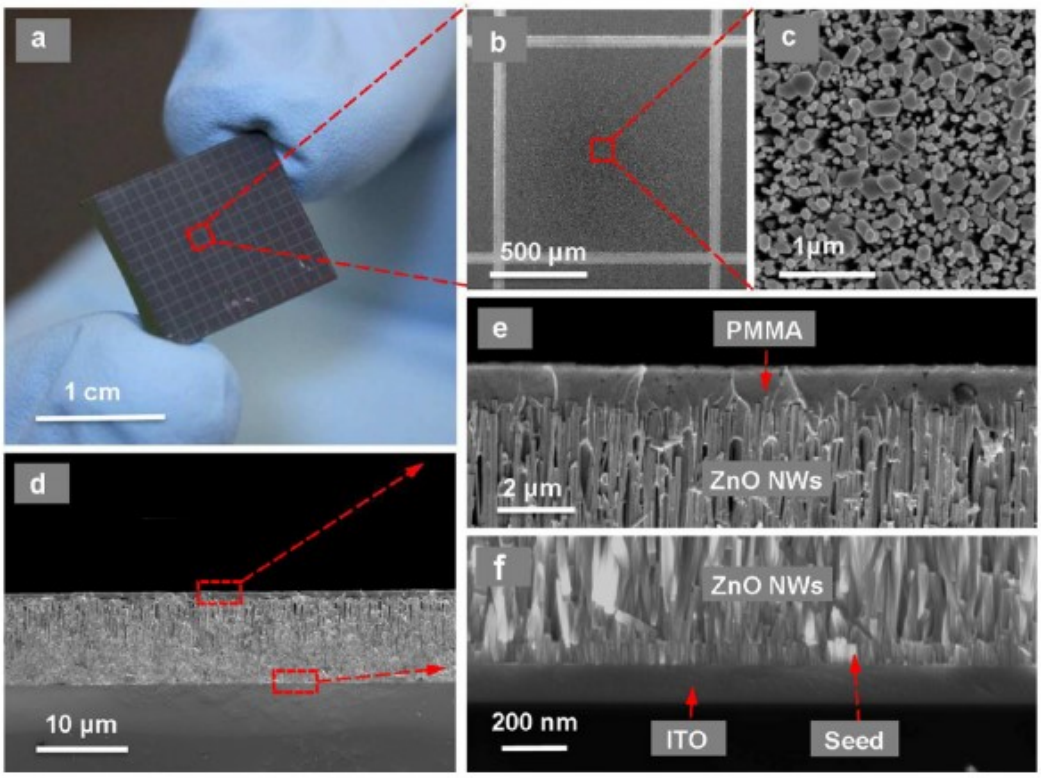

Figure 2.8 Structure of the nanogenerator. (a) Photograph of nanogenerator after position-controlled growth of ZnO nanowires. (b) SEM image of one segment of the nanogenerator that is well-defined by photolithography. (c) Enlarged top view of SEM image of the synthesized ZnO nanowires. (d) Cross-sectional view of SEM image of the device structure after spin-coating a PMMA on the grown nanowires. (e) Enlarged SEM image showing coverage of nanowires by the PMMA layer. (f) Enlarged SEM image of the seed layer and the ITO layer between NWs and the substrate. [47]

chanical energy is able to converted into electricity due to constructive piezoelectric-potential generation from the two components-PVDF and ZnO nanowires, when the hybrid fiber was under elongating or bending. Electrical measurements of the hybrid-fiber nanogenerator attached on a human arm is shown in Figure 2.10.

2.1.3 AlN-based Energy Harvesting

AlN is the most commonly used complementary metal-oxide-semiconductor (CMOS) compatible piezoelectric material, which is typically deposited on Si in order to enhance the c-axis (002) crystal orientation which gives AlN its high piezoelectric properties. Unlike other com-

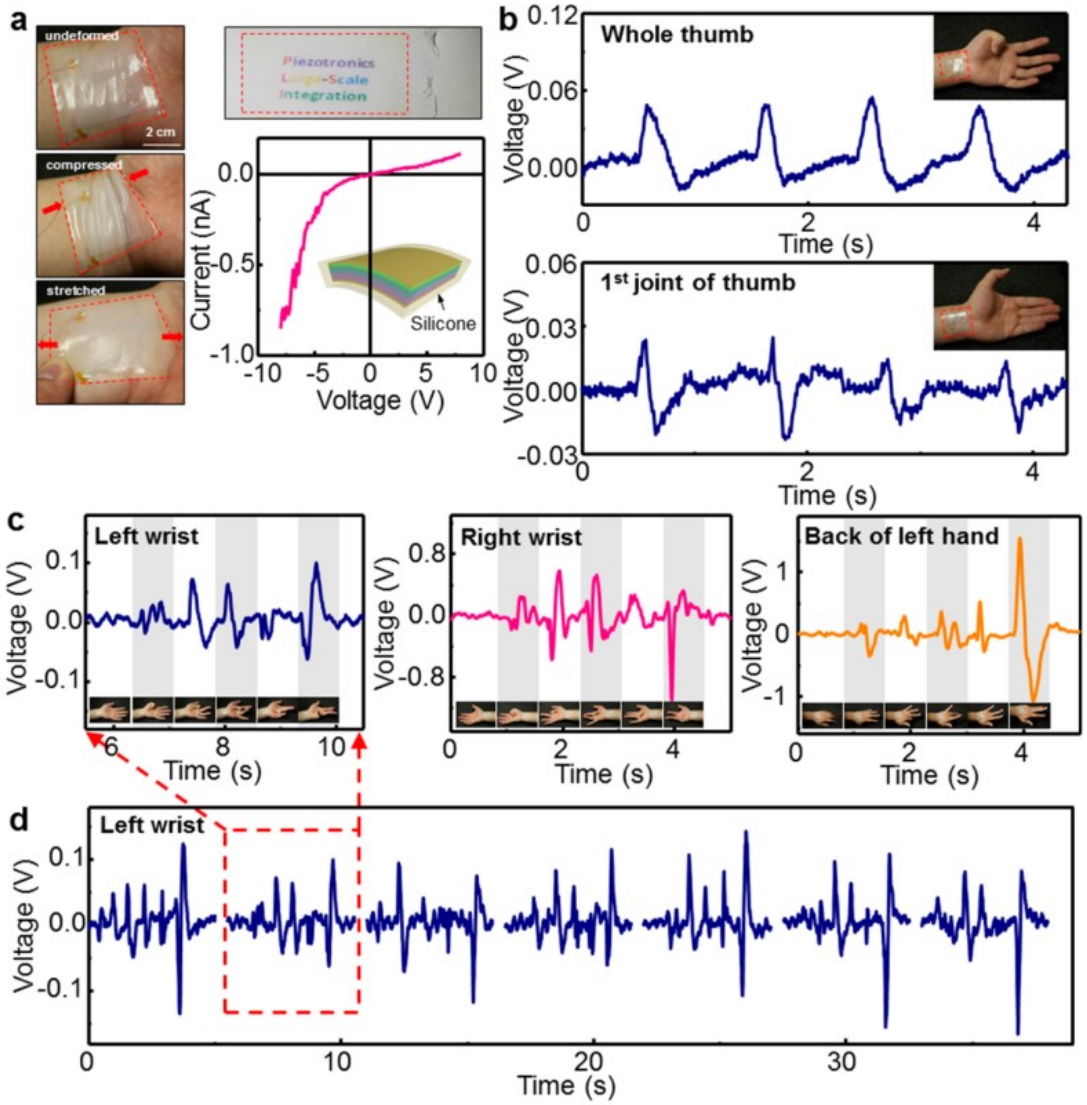

Figure 2.9 Homojunction nanogenerator grown in the pn configuration on silicone rubber for gesture recognition by measurement of flexor movement. (a) Photographs show the device mounted on a human wrist, and the IV characteristics. (b) Output voltage of the device as a function of the difference in flexion of the thumb. (c) Output voltage when fingers were individually flexed and extended starting with the left wrist. (d) Repeating the same gesture to show the stability of the device. [48]

monly used piezoelectric materials (e.g. PZT), AlN is not ferroelectric which means it does not require poling. PZT is a ceramic piezoelectric material with a high elastic modulus which is typically a disadvantage for flexible energy harvesting. Recently researchers have attempted to fabricate AlN-based flexible energy harvester and made continuous progress.

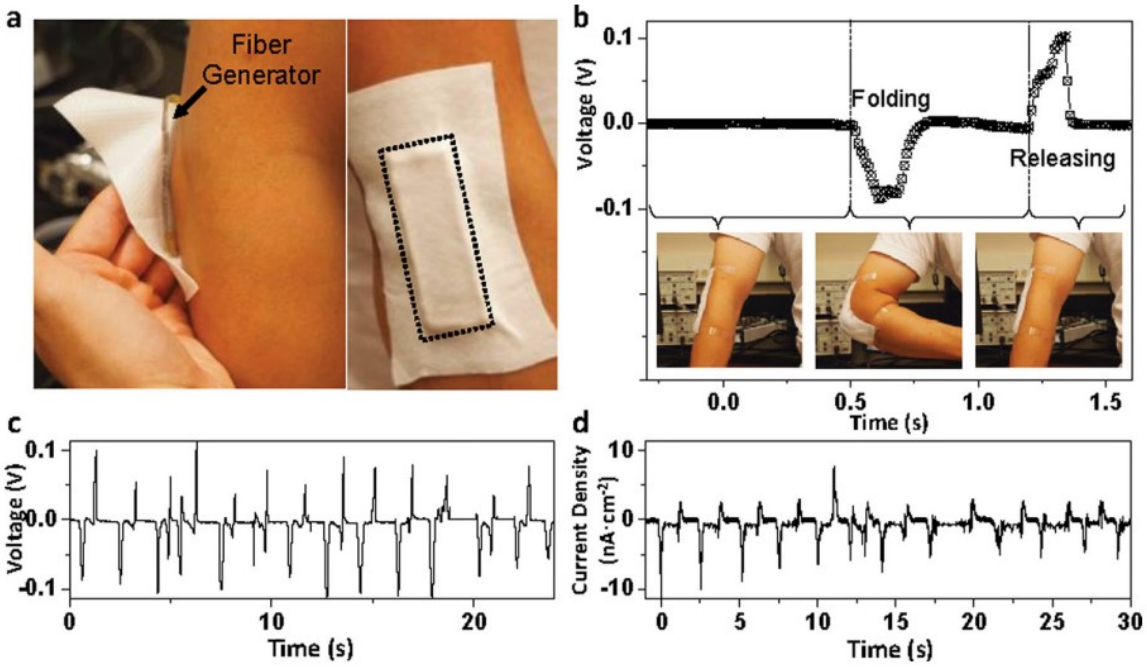

Figure 2.10 Electrical measurements of the hybrid-fiber nanogenerator attached on a human arm. (a) Photographs of hybrid-fiber device attached on a human elbow. (b) Open-circuit voltage output depending on the folding and releasing of the elbow. (c) Open-circuit voltage outputs of a fiber device during multiple folding-releasing events of the elbow. (d) Closed-circuit current density during multiple folding-releasing events of the elbow. [49]

Jackson et al. [50] investigated a polyimide/AlN flexible material which exhibited improved AlN crystallinity and piezoelectric properties along with being CMOS friendly and biocompatible. Piezoelectric coefficient d_{33} of the deposited AlN is 1.12 pm/V, and SEM images show high quality columnar grains. The highly crystalline AlN material is due to the semi-crystalline properties of the polyimide film used. In addition, the authors showed the films surface properties including surface roughness and contact angle which can affect cell adhesion, demonstrating that the material has potential of being used in biomedical or other MEMS applications. Photograph and generated voltage of the developed flexible AlN/polyimide material is shown in Figure 2.11.

Akiyama et al. [51] demonstrated c-axis oriented AlN thin films prepared on polyimide films for flexible composite piezoelectric materials. The AlN films can operate at a temperature range from -196 °C to 300 °C, as well as a wide pressure range from hundreds of

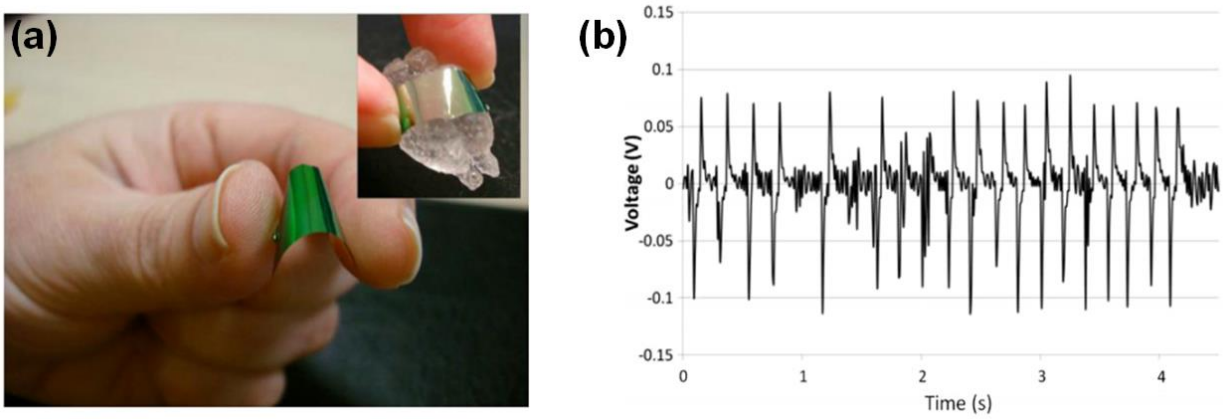

Figure 2.11 Photograph and generated voltage of the developed flexible AlN/polyimide material. (a) Photograph showing the flexibility of the material. (b) Voltage generated by tapping the material with a probe with electrodes connected to Ti layer and Au layer. [50]

pascals to 40 MPa. The sensitivity of the AlN films is able to be controlled by changing the geometric form. The AlN based laminate composite structure has potential to overtake PVDF in application with wide temperature range (e.g. from -20 °C to 70 °C), allowing it to be a promising material for new, flexible piezoelectric sensors. Photograph and output voltage of the developed AlN film for pulse waveform measurement is shown in Figure 2.12.

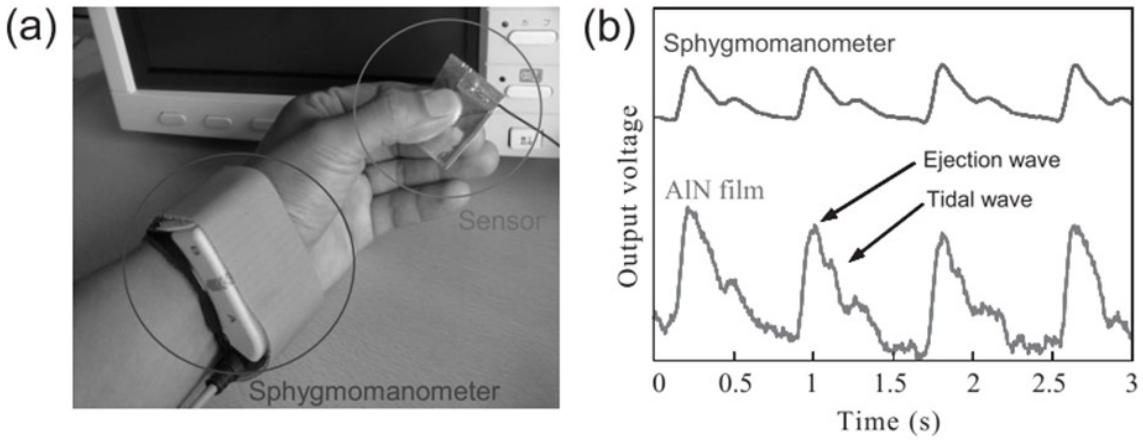

Figure 2.12 Pulse waveform measurement with the aid of the developed AlN film. (a) Photograph of the actual test setup. (b) Response of the electric sphygmomanometer (top) and AlN film (bottom) to the pulse wave on a finger. [51]

Petroni et al. [52] presented the fabrication and the characterization of flexible micro-cantilevers based on AlN as piezoelectric active layer and polyimide as elastic substrate. The

highly c-axis oriented hexagonal crystal structure of AlN thin film is grown by sputtering deposition and embedded into two layers of molybdenum. The flexible structures are fabricated by a two masks process, using a silicon support to perform device key steps together with optimized processes for peeling off and patterning. The mechanical response of the fabricated flexible cantilevers was investigated by piezoresponse measurements. Photograph of flexible cantilevers and experimentally obtained first resonance frequency are shown in Figure 2.13.

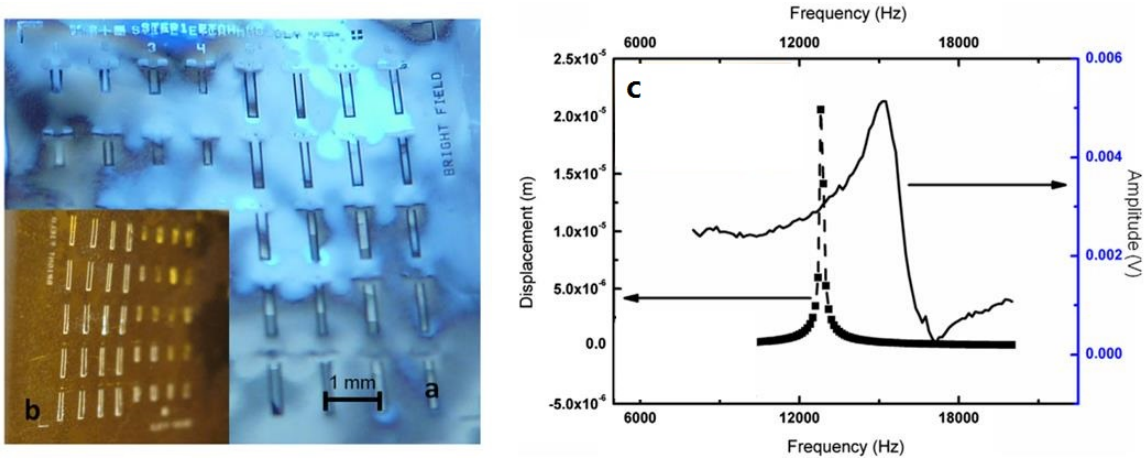

Figure 2.13 Photograph of flexible cantilevers and experimentally obtained first resonance frequency. (a) Front image of an array 5 × 8. (b) Back image of cantilever. (c) Measured voltage signal during deflection (solid) and simulated displacement with a maximum amplitude of 20.6 μm (square). [52]

Petroni et al. [53] further developed a small flag made by piezoelectric thin film on flexible polymers in order to resemble the dry leaves of trees. It is able to efficiently harvest energy from wind at extremely low speed (e.g. from a gentle blow or breath). By depositing a thin film of piezoelectric AlN sandwiched between metal electrodes with columnar grains coherent through the polycrystalline layers on Kapton substrates, piezoelectricity on flexible polymers was realized. A natural curling of developed flags can be observed due to the release of the residual stress of the layers. Since the curling is essential for the activation of the maximum flag oscillation, this system is elastic and light. Photograph of the flag and generated voltages by it in the wind tunnel is shown in Figure 2.14.

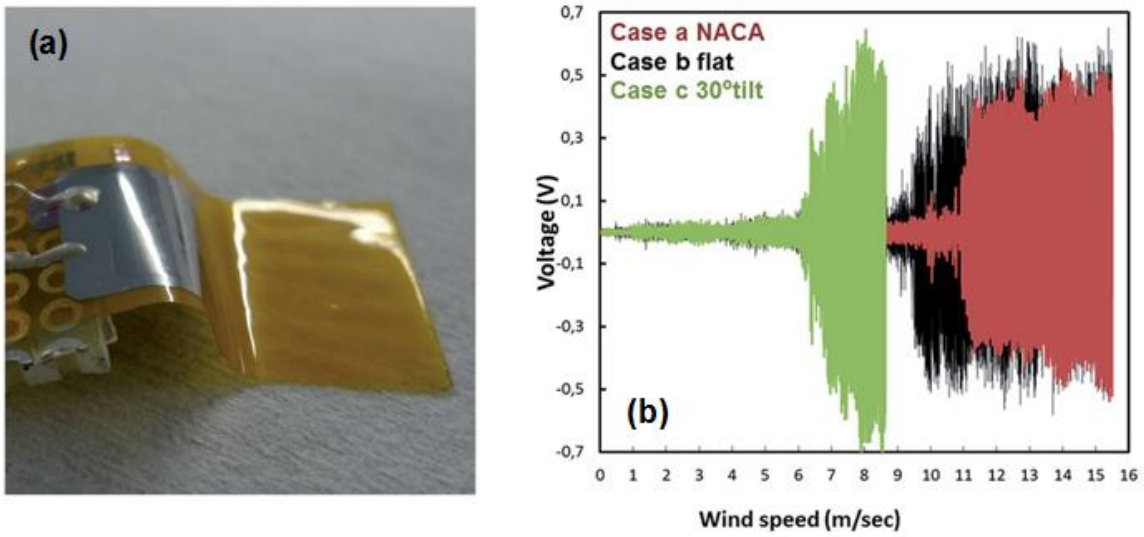

Figure 2.14 Photograph of the flag and generated voltages by it in the wind tunnel. (a) Flag prototype tested in the wind tunnel. (b) Comparison of generated voltages shows that the drag force need to fatten the flag is determined by the position of the flag. [53]

2.2 Piezoelectric Polymer

There are three main polymer categories that can be considered piezoelectric, as shown in Figure 2.15. The first category of piezoelectric polymer is the bulk polymer, which is solid polymer films that have the piezoelectric mechanism through their molecular structure and arrangement. The second category is the piezoelectric composite polymer, which is polymer structure with integrated piezoelectric ceramic (e.g. PZT) that originally has piezoelectric effect. This kind of composite takes advantages of both the mechanical flexibility of polymer and the high electromechanical coupling of the piezoelectric ceramic. The third type is the voided charged polymer which is a dramatically different type of piezoelectric polymer than the other two categories. This polymer film features artificial voids whose surfaces are charged in a way to form internal dipoles. State-of-the-art materials and applications of these three categories of polymers are discussed in the following subsections.

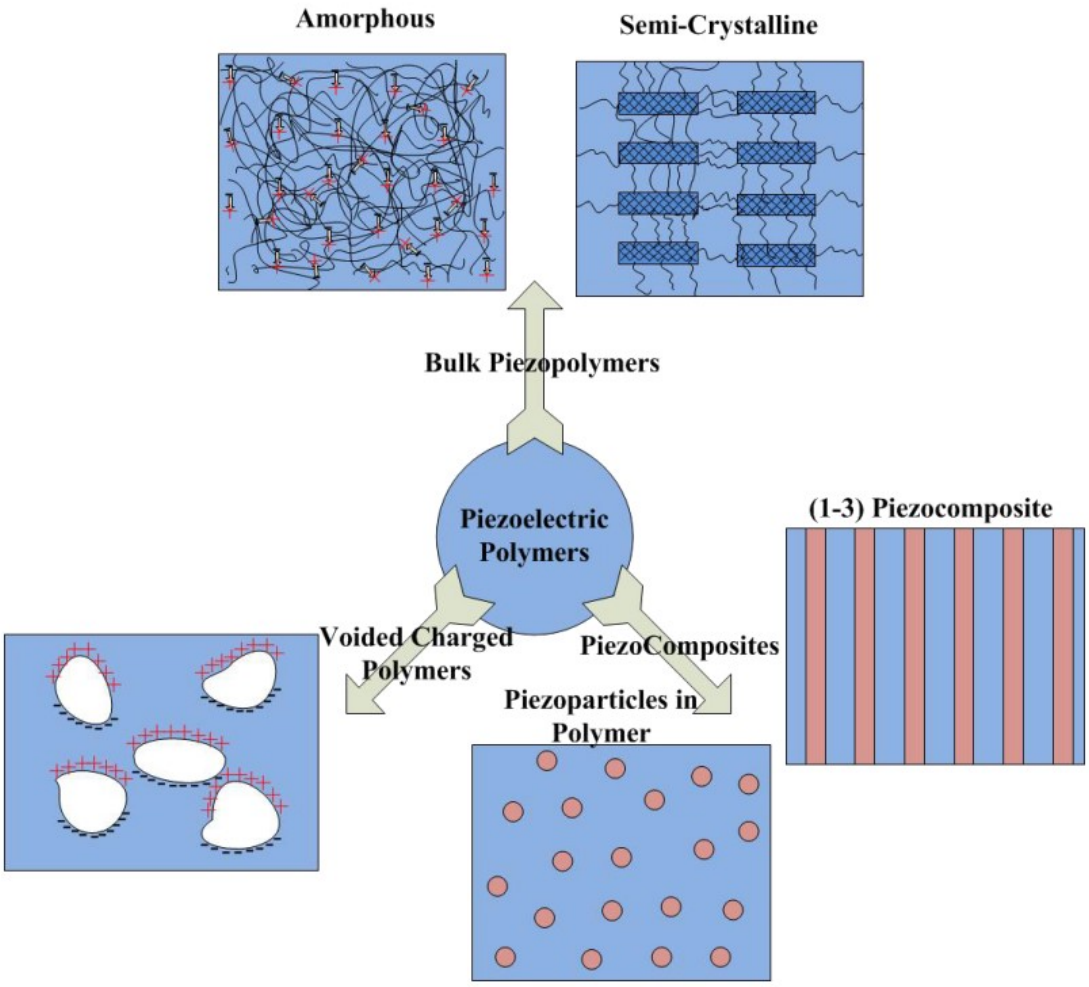

Figure 2.15 Graphical representation of the different catogories of piezoelectric polymers. [54]

2.2.1 Bulk Piezoelectric Polymer

The piezoelectric effect of the bulk piezoelectric polymers is due to the molecular structure and orientation of the polymer. There are two categories of bulk polymers with different operating principles: semi-crystalline polymers and amorphous polymers. In both categories, there are structural requirements that should exist for a bulk polymer material to be piezoelectric-molecular structure of the polymer should inherently contain molecular dipoles; dipoles can be reoriented with the bulk material and kept in preferred orientation state [54]. As a typical semi-crystalline polymer, PVDF is one of the most commonly used and widely

researched piezoelectric film which exhibits considerable flexibility when compared to PZT.

Li et al. [55] proposed a bio-inspired PVDF-leaf architecture which converts wind energy into electrical energy by wind-induced fluttering motion. A dangling cross-flow stalk arrangement is explored rather than fluttering devices that arranged in parallel with the flow direction. Since this architecture amplifies the vibration by an order of magnitude, it is potentially appropriate for low-cost organic piezomaterial. A prototypes using flexible piezoelectric materials as stalks and polymer film as leaves were fabricated. A series of experiments demonstrated a peak output power of approximately 600 μW with the maximum power density of approximately 2 mW/cm^3 from a single device. Photographs and measured power harvested by the developed devices are shown in Figure 2.16.

Fang et al. [56] demonstrated that needless electrospinning is able to fabricate piezoelectric nanofibers not only on higher productivity than needle electrospinning, but also having better energy harvesting performance. The power generated from needleless electrospun nanofiber webs is shown to be used for running electric coolers, which indicated that needleless electrospun nanofiber webs may represent a practical candidate for producing piezoelectric power generators for energy-harvesting applications. They demonstrated that needleless electrospun PVDF nanofiber revealed enhanced piezoelectric performance, and the operating voltage for electrospinning had a significant effect on the piezoelectric properties of the nanofibers. Figure 2.17 shows the purpose-built needleless electrospinning setup used for producing PVDF nanofibers and the fabricated PVDF nanofiber mat.

2.2.2 Piezoelectric Polymer Composite

Piezoelectric polymer composite or piezocomposite is a polymer material with embedded inorganic piezoelectric material, while polymer usually does not have electromechanical effect. By mixing piezoelectric ceramics with polymer, the advantages of both materials that include the higher coupling factor and dielectric constant of ceramics and the mechanical flexibility of polymers are achieved at the same time. There are different combinations of the

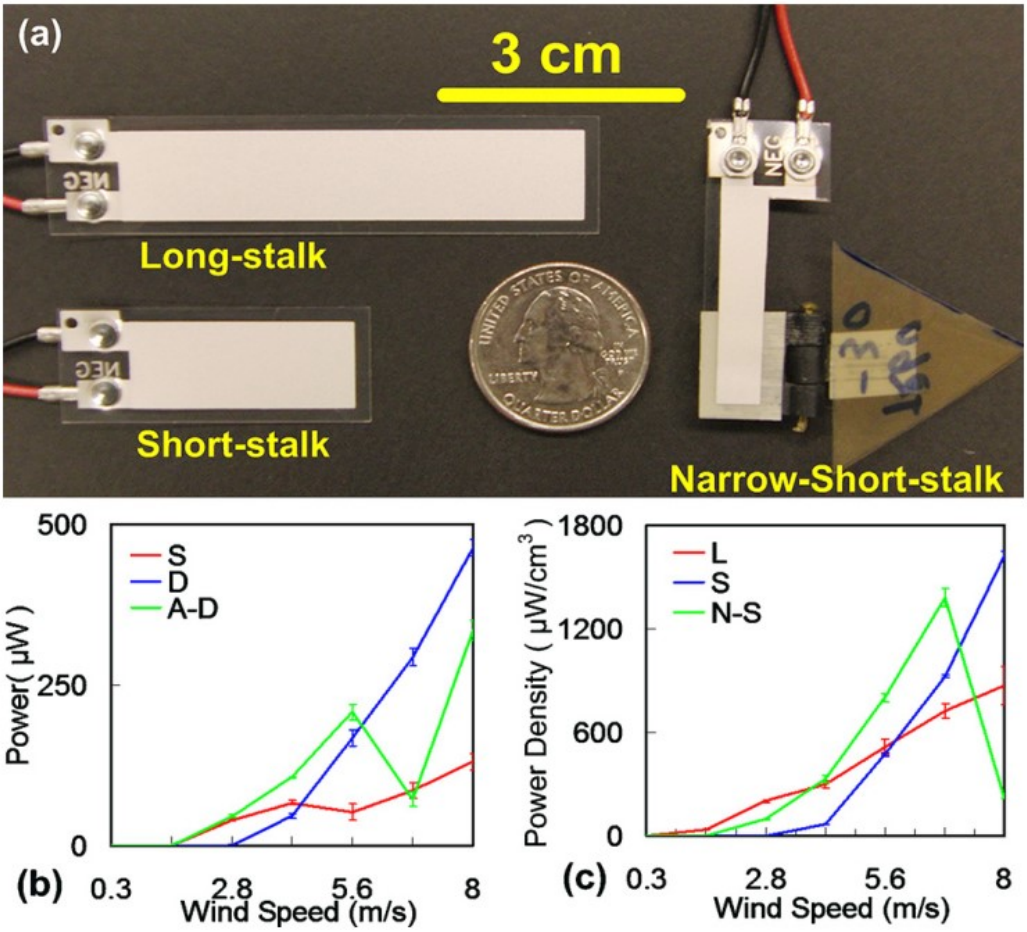

Figure 2.16 Photographs and measured power harvested by the developed devices. (a) Three PVDF stalks (long, short, and narrow-short) with thickness of 205 μm used in experiments. (b) Output power of three configurations (single-layer, adhered double-layer, and air-spaced double-layer). (c) Power density of long, short and narrow-short stalk. [55]

ceramic/polymer composites. One typical approach is to impinge microscale or nanoscale particles inside a polymer matrix.

Park et al. [57] reported a nanocomposite generator which achieved a simple, low-cost and large area fabrication based on $BaTiO_3$ nanoparticles synthesized by hydrothermal reaction and graphitic carbons, such as single-walled and multi-walled carbon nanotubes, as well as reduced graphene oxide. The $BaTiO_3$ nanoparticles can carbon nanomaterials are dispersed in PDMS by mechanical agitation to produce a piezoelectric nanocomposite which is spin-casted onto metal-coated plastic substrates and cured in oven. It showed that under periodic

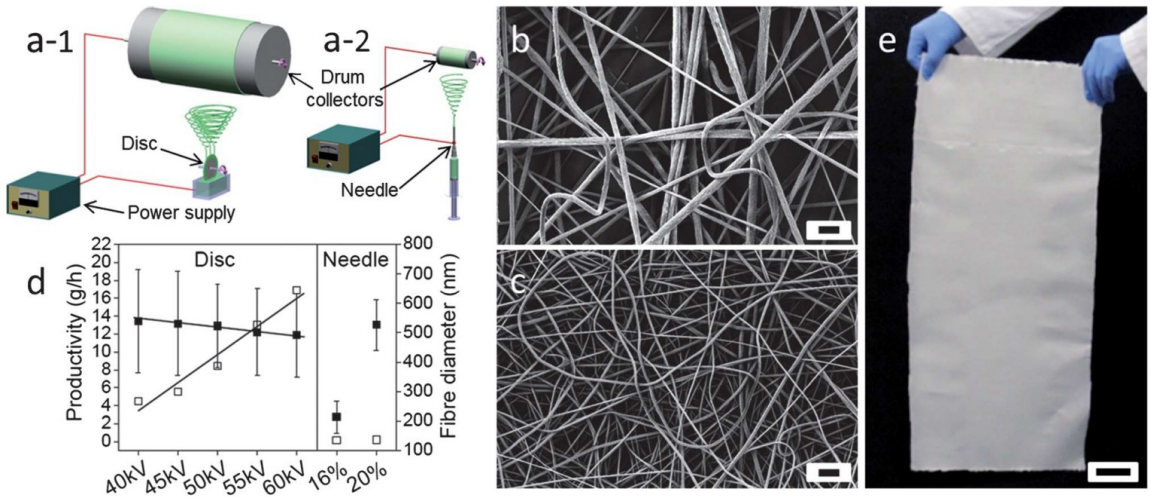

Figure 2.17 Purpose-built needleless electrospinning setup and the fabricated PVDF nanofiber mat. (a) Apparatus for disc and needle electrospinning. SEM images of (b) the PVDF nanofibers electrospun by disc and (c) needle. Scale bar, 2 um. (d) Diameter and productivity under different spinning conditions. (e) Photograph of a large piece of PVDF nanofiber mat prepared by disc electrospinning. Scale bar, 5 cm. [56]

external mechanical deformation by bending stage or biomechanical movements from human finger, electric signals can be repeatedly generated from the developed device and used to operate a commercial red LED. The flexible nanocomposite generator made of $BaTiO_3$ nanoparticles and graphic carbons are shown in Figure 2.18.

2.2.3 Voided Charged Polymer

Voided charged polymer or cellular polymer is the polymer materials that contain internal gas voids. When the polymer surfaces surrounding the voids are charged, the voided charged polymer behaves like a piezoelectric material, coupling electrical and mechanical energy. Such a structure can have a high piezoelectric coefficient d_{33} reaching up to 20,000 pC/N, a comparably higher value than that of piezoceramics [58]. Voided charged polymer behaves like piezoelectric material; however, the piezoelectric coefficient in this hybrid material depends on factors different from that of regular piezoelectric materials. The shape and density of the voids affect the distribution of the formed dipoles; the type and pressure

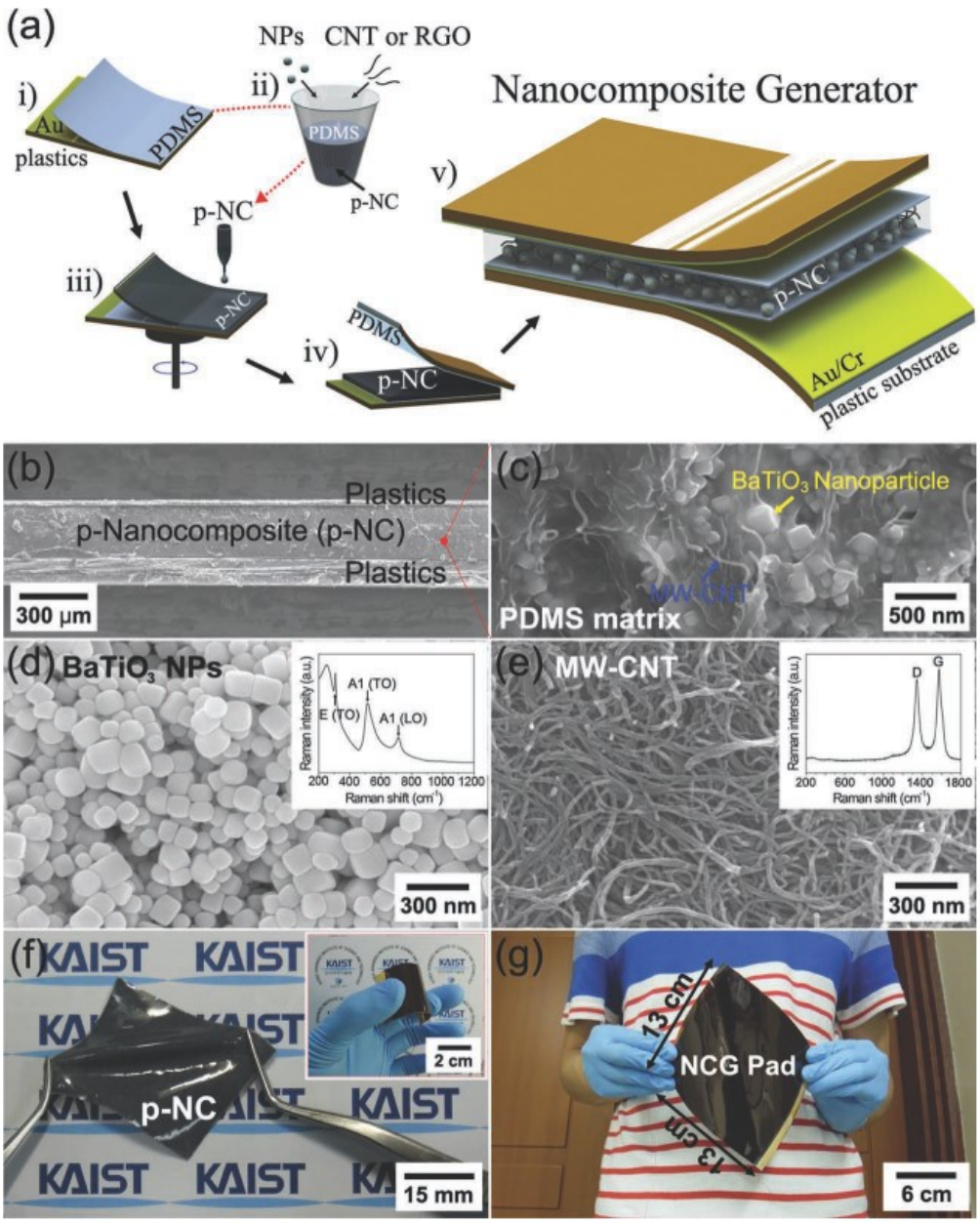

Figure 2.18 Flexible nanocomposite generator made of $BaTiO_3$ nanoparticles and graphic carbons. (a) Fabrication process. (b) A cross-sectional SEM image. (c) A magnified cross-sectional SEM image. (d) SEM image of the $BaTiO_3$ nanoparticles. (e) Multi-walled carbon nanotubes. (f) Photograph of the nanocomposite generator stretched by tweezers. (g) A large-area (13 cm $\times$ 13 cm) type of nanocomposite generator. [57]

of gas inside the voids affects the amount of ionization occurring during the poling process [54]. All these factors have great influence on the value of its piezoelectric coefficient.

Wang et al. [59] demonstrated the fabrication of piezoelectric PDMS films using multi-

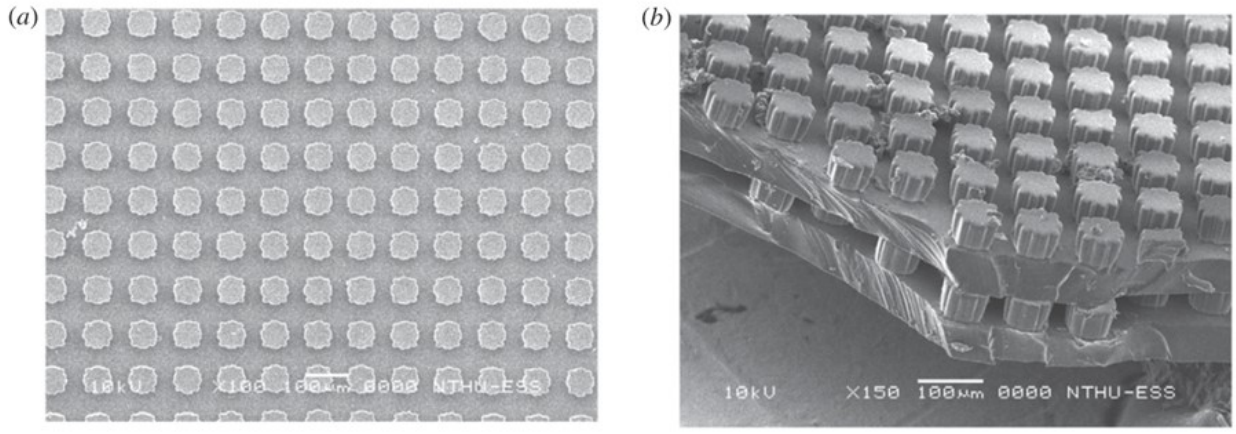

Figure 2.19 SEM images of the fabricated PDMS microstructures with void geometry. (a) Top view. (b) 3D view. [59]

layer casting, stacking, surface coating and micro plasma discharge process. Cellular PDMS structures with micrometer-sized voids are implanted with bipolar charges on the opposite inner surfaces to achieve the desired electromechanical sensitivity. The implanted charge pairs function as giant dipoles that respond promptly to diverse electromechanical stimulation. The fabricated charge-implanted, cellular PDMS films show a low effective elastic modulus of $\sim$ 500 kPa, and a high piezoelectric coefficient $d_{33} \sim 300$ pC /N, which is much higher than those of common piezoelectric polymers (e.g. PVDF). Thus, the demonstrated piezoelectric PDMS films could potentially be used as flexible and sensitive electromechanical materials for a variety of sensor and energy harvester. The SEM images of the fabricated PDMS microstructures with void geometry is shown in Figure 2.19.

Feng et al. [60] micro-fabricated a high-density cellular piezoelectret with high-aspect-ratio polymer structures based on the trench-filled parylene technology. Vertical walls of the parylene structures were charged by using soft X-ray to realize uniform artificial dipoles whose moments could vary along with parylene structural deformation driven by the inertia of a seismic mass. Measurements showed that the charge and voltage sensitivities are 9600 pC/N and 960 V/N, respectively, with respect to the in-plane resonant oscillation that achieved at 149 Hz. SEM images and the overview of the fabricated device is shown in

Figure 2.20.

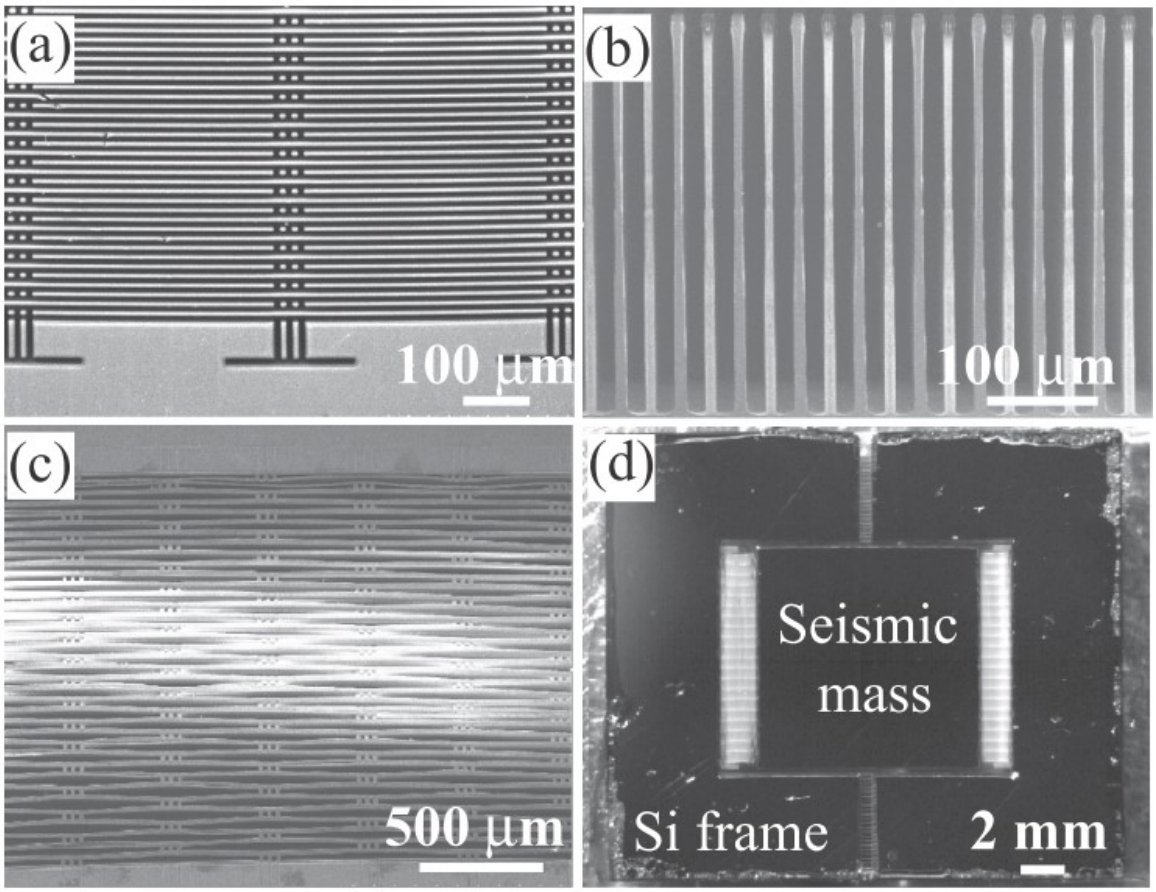

Figure 2.20 SEM images and the overview of the micro-fabricated device. (a) Top view of DRIE silicon trenches. (b) Cross section of the 350 μm deep trenches. (c) Free-standing parylene-C cellular structure. (d) Prototype of the fabricated MEMS transducer. [60]

2.3 Triboelectric Nanogenerator

Since 2012, based on triboelectric effect [61, 62], a revolutionary invention–triboelectric nanogenerator (TENG) has been launched by Prof. Zhong Lin Wang as a new energy harvesting technology which owns unique figure of merits: large output power, high efficiency, low weight and cost effective material, simple fabrication, high adaptability to different applications [63]. The first triboelectric nanogenerator is shown in Figure 2.21.

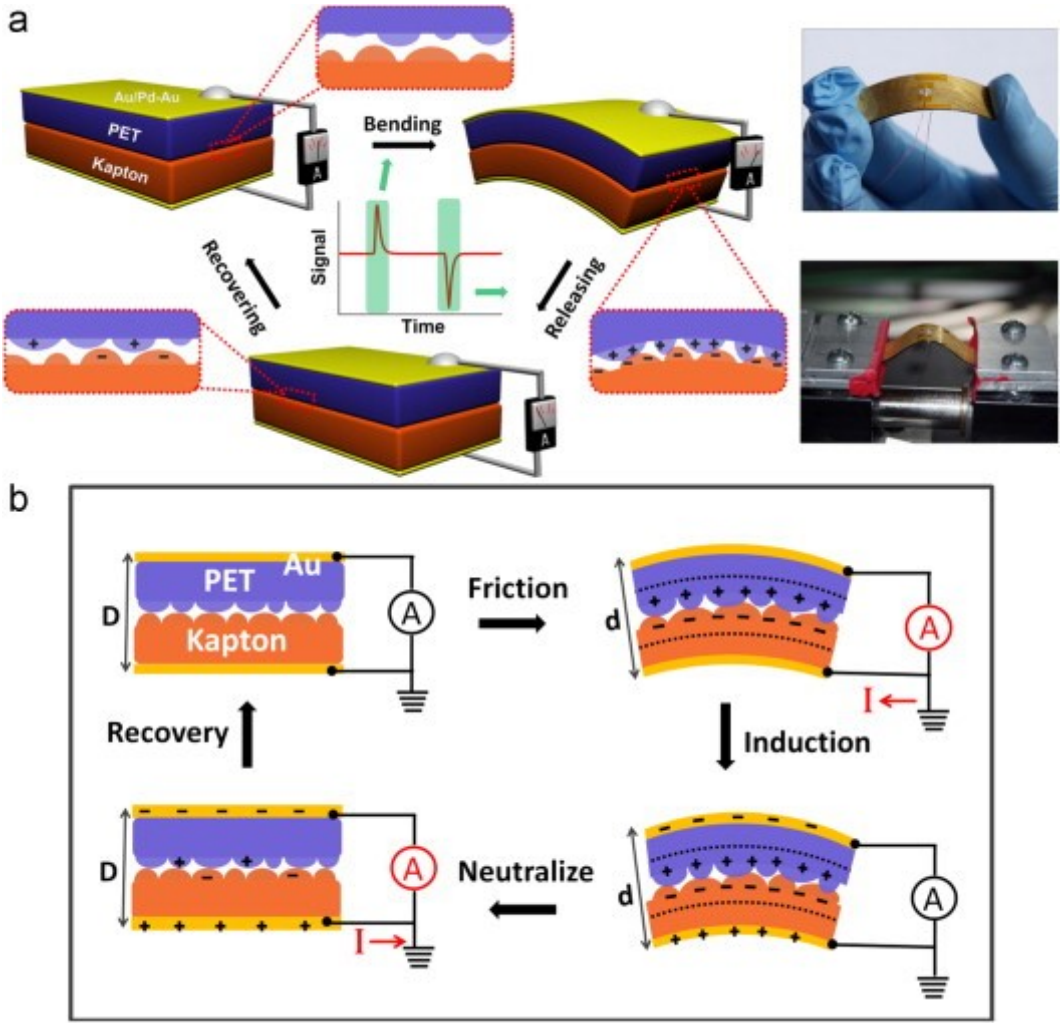

Figure 2.21 Schematic illustration of the structure and working principle of the first triboelectric generator. (a) The structure of the triboelectric nanogenerator under bending and releasing and experimental setup for electrical measurement. (b) An illustration of the working principle of the first triboelectric nanogenerator. [63]

The first-reported triboelectric nanogenerator has a multi-layers structure. Due to the coupling between triboelectric effect and electrostatic induction, the periodic contact and separation between Kapton and PET, triggered by external mechanical motion, alternatingly drives the induced electrons between electrodes. And a peak voltage of 3.3 V, a current of 0.6 A with a peak power density of 10.4 mW/cm^3 was delivered. In this process, the mechanical energy is effectively converted into electricity. Since the invention of the first triboelectric nanogenerator, remarkable progress has been made in the fields of energy harvesting, self-

powered devices and systems [64, 65, 66]. There are four fundamental operation modes of the triboelectric nanogenerator systematically developed: vertical contact-separation mode [67, 68, 69], in-plane linear sliding mode [70, 71], single electrode mode [72, 73], and freestanding triboelectric-layer mode [74], as summarized in Figure 2.22.

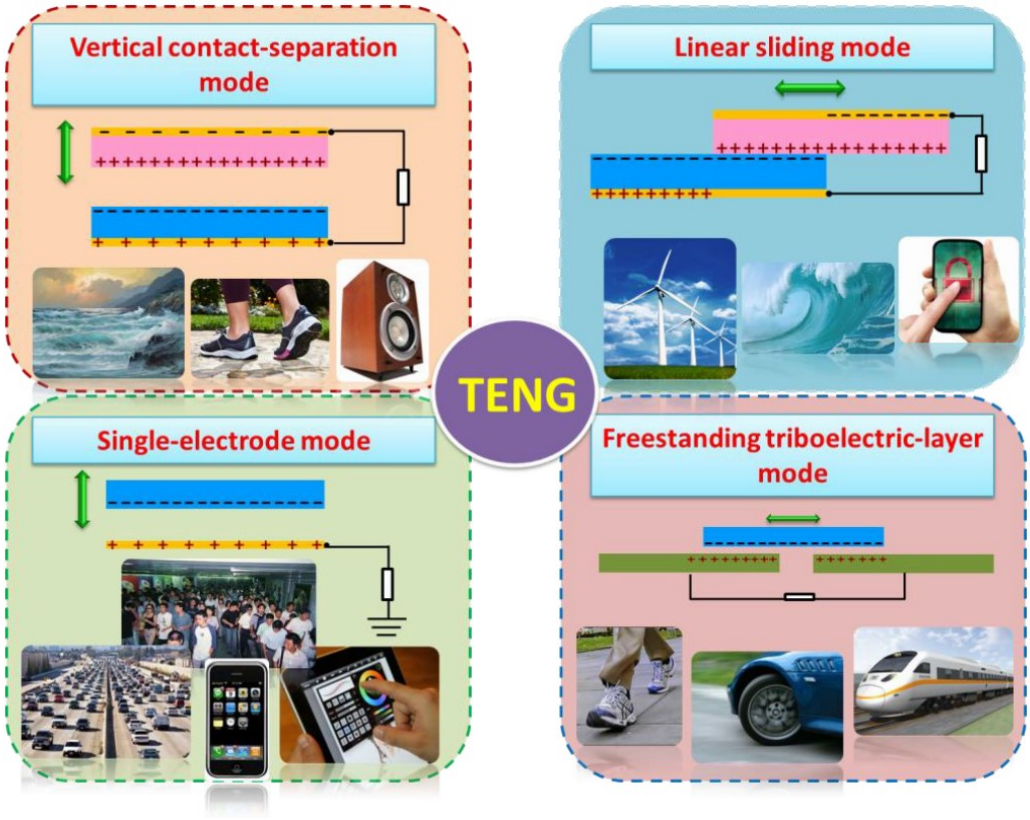

Figure 2.22 Four fundamental modes of triboelectric nanogenerators: vertical contact-separation mode, in-plane contact-sliding mode, single-electrode mode, and freestanding triboelectric-layer mode. [66]

Based on the four modes, various triboelectric nanogenerators have been fabricated for specific applications. A collection of photographs of the triboelectric nanogenerators fabricated by Prof. Zhong Lin Wang's group for harvesting various types of energy are shown in Figure 2.23. These structures are the fundamental units for providing micro-scale power for small electronics; however, their assembly and integration can be the basis for harvesting mega-scale energy.

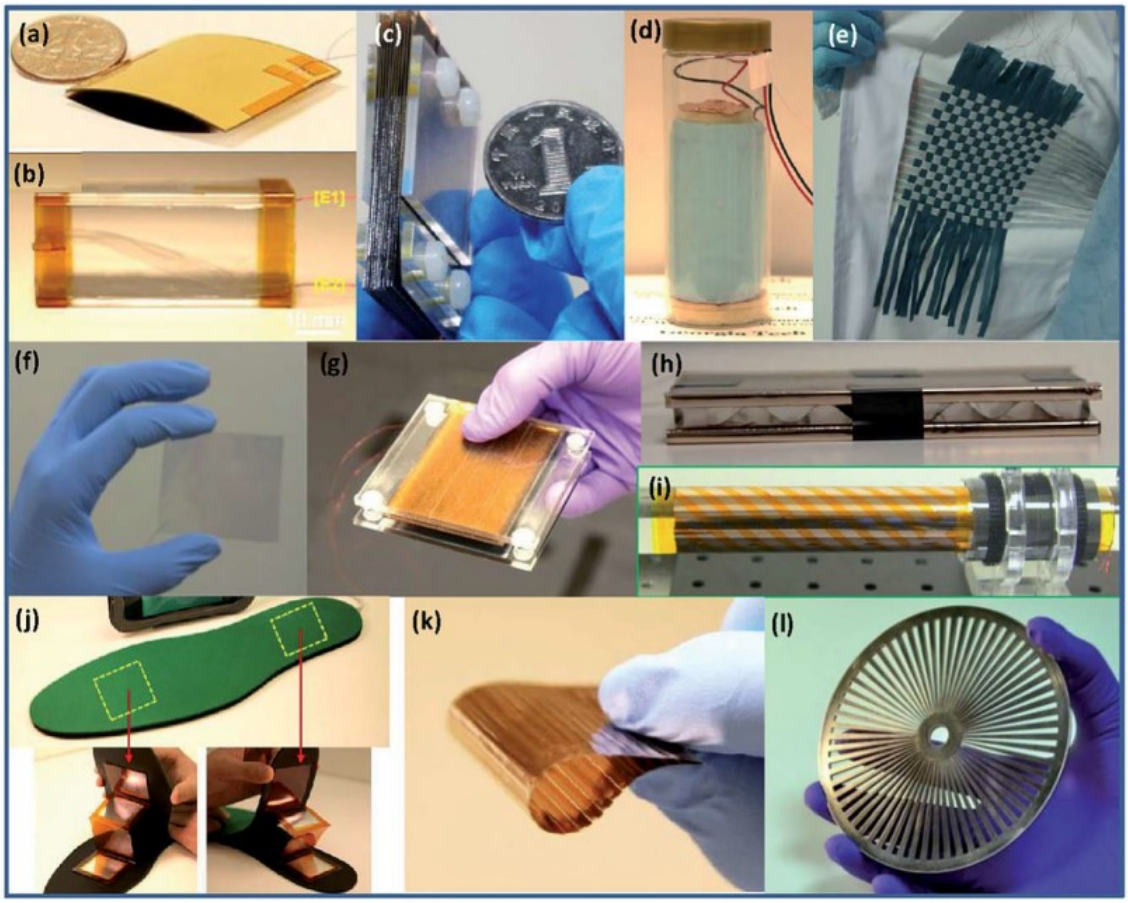

Figure 2.23 Photographs of some triboelectric nanogenerators fabricated for harvesting: (a) finger tapping energy; (b) air-flow/wind energy; (c) relative in-plane sliding energy; (d) enclosed cage for harvesting oscillating/disturbing energy in water or mechanical vibration; (e) fabric for harvesting body motion energy; (f) transparent TENG for harvesting energy in touch pad; (g) foot/hand pressing energy; (h) water impact energy; (i) cylindrical rotation energy; (j) shoe insole for walking energy; (k) flexible grating structure for harvesting sliding energy; and (l) disc shape rotation energy. [66]

CHAPTER 3

PRELIMINARY WORK – FLEXIBLE NANOGENERATOR BASED ON NANOCRYSTALLINE ALN THIN FILM

In the early stages of MEMS development (starting around 1960), piezoelectric materials were rarely used and mostly restricted to ZnO, as it was hard to access deposition techniques that would guarantee repeatable results. Furthermore, the most common piezoelectric material used for the making of macroscale transducer was PZT, which was more difficult to process and integrate as a thin film on silicon though important progresses had been continuously made, let alone its quality factors are too low for some radio frequency (RF) applications, and especially was of concern to IC fabrication facilities because of contamination risks in CMOS lines. Thin film ZnO also suffered from silimar issues, and its reactivity with other IC materials made it hard to integrate with standard CMOS process [75].

With the introduction of AlN and especially the commercial success of the thin-film bulk acoustic resonator (FBAR), interest in piezoelectrics for MEMS blossomed. It is fair to state that industry drives for more compact and cheaper radio frequency (RF) duplexers, and the consequenct investments in the development of repeatable physical vapor deposition (PVD) techniques for the growth of AlN films on silicon have spurred a great deal of activities in the field of piezoelectric and espectially AlN MEMS. Practically, most conventional MEMS devices that used to be made out of silicon have recently been reproduced (in most cases with enhanced performance) by using AlN thin-film piezoelectric technology. For example, resonators [76, 77, 78, 79], filters [80, 81, 82], switches [83, 84, 85], energy harvesters [86, 87, 88], ultrasonic transducers [89, 90], microphones [91, 92], strain sensors [93], chemical sensors [94], and accelerometers [95] have been demonstrated using AlN thin film.

Here, this chapter report the development of a flexible nanogenerator based on nanocrystalline aluminum nitride (AlN) thin films developed at room temperature. The AlN thin

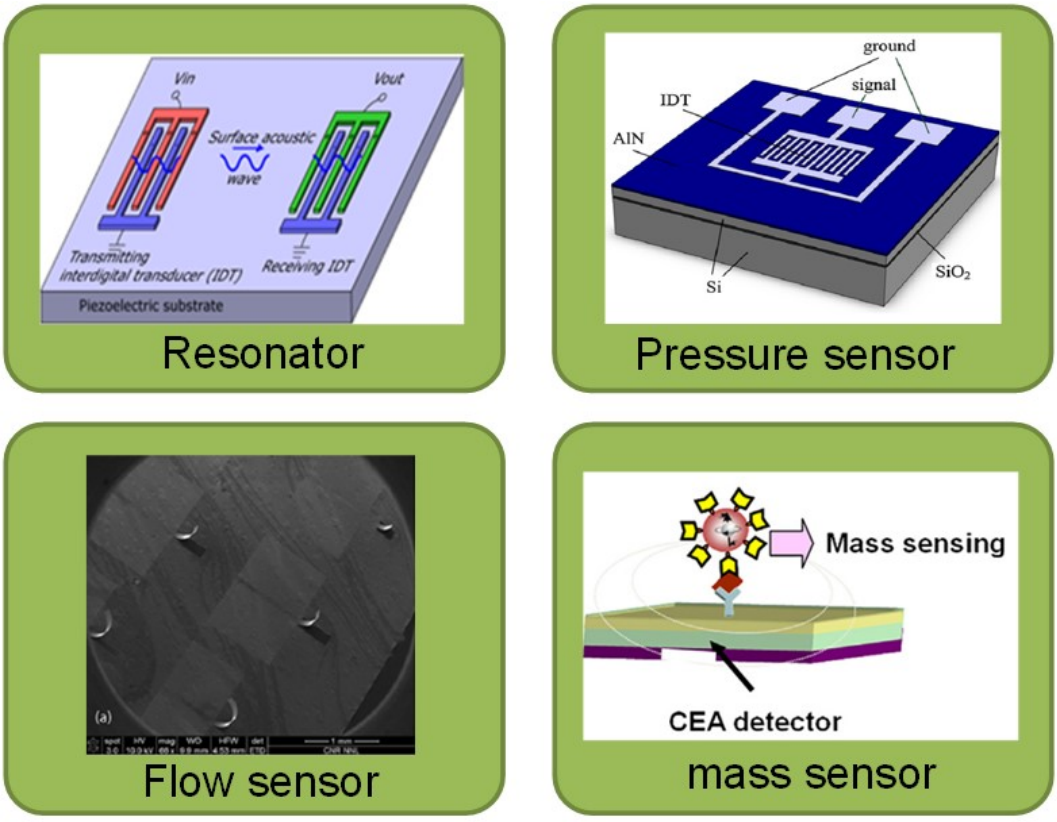

Figure 3.1 Applications of piezoelectric aluminum nitride thin film. [96, 97, 98]

film was grown by pulsed laser deposition (PLD) on a thin aluminum layer. X-ray diffraction and transmission electron miscroscope images show that the AlN films consist of crystalline columnar grains oriented in the (100)-direction. A polyimide thin film encapsulated the flexible NG to further improve mechanical robustness, protect the device from abrasion, and enhance its potential biocompaibility.

3.1 AlN Thin Film Grown by PLD

PLD is a physical vapor deposition process, carried out in a vacuum system, that shares some process characteristics common with molecular beam epitaxy and some with sputter deposition [99]. Typically, PLD system comprises a laser source, a set of optical components used to focus the laser beam onto a target of the material to be deposited, and an ultra-high

vacuum chamber where the target and substrate are located opposite to each other [100]. One of the major benefits of the PLD techniques is separating the ultra-high vacuum chamber and the evaporation power source, allowing for the selection of different ambient background gas and pressure during the deposition process. For instance, during the deposition process of VO_2, oxygen is introduced to assure sufficient oxygen in the nano-structure [101, 102, 103].

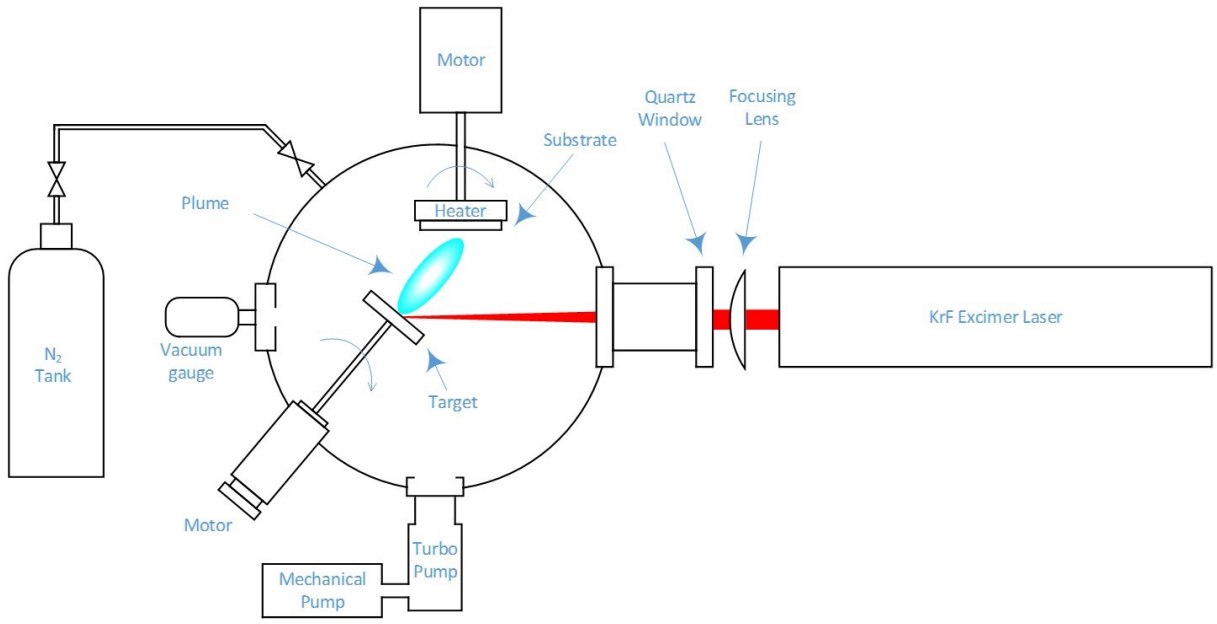

Figure 3.2 Schematic illustration of PLD system for piezoelectric AlN thin film growth.

Schematic illustration and photograph of PLD system for AlN thin film growth are shown in Figure 3.2 and 3.3, respectively. It can be seen that a pulsed laser is focused onto a target of the material (AlN in this case) to be deposited. During the growth process, each laser pulse with sufficiently high laser energy density ablates or vaporizes a small amount of the AlN to create a plasma plume. The ablated AlN is ejected from the target in a highly forward-directed plasma plume which provides the material flux for film growth (Figure 3.4). Since the substrate temperature is typically much lower than the melting temperature of the target material, the thin film growth usually takes place far from the thermodynamic equilibrium. This enables growth of metastable phases and artificial structure [104]. Typical PLD system has been effectively limited to small substrate (2-inch silicon wafer in this case);

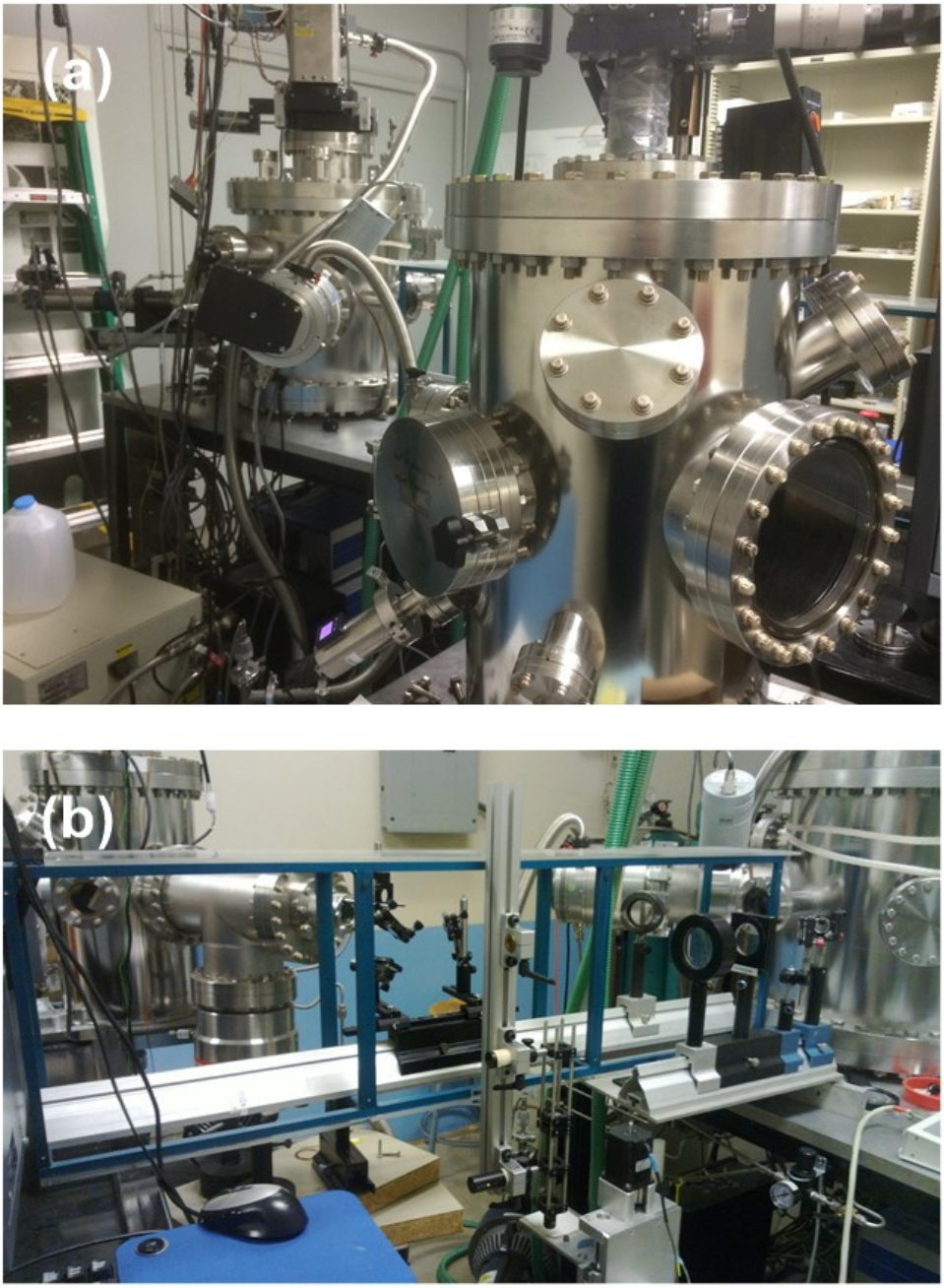

Figure 3.3 Photograph of PLD system for piezoelectric AlN thin film growth. (a) Ultra-high vacuum chamber. (b) Optical components.

large area PLD system now allows for the deposition on larger substrates (e.g. 8-inch silicon wafer [105]) by using dynamic mirrors and lenses. It should be mentioning that PLD process also allows for the stoichiometric transfer of the target material onto the substrate. This is because the pulsed laser beam heats the target so quick with all components of the target

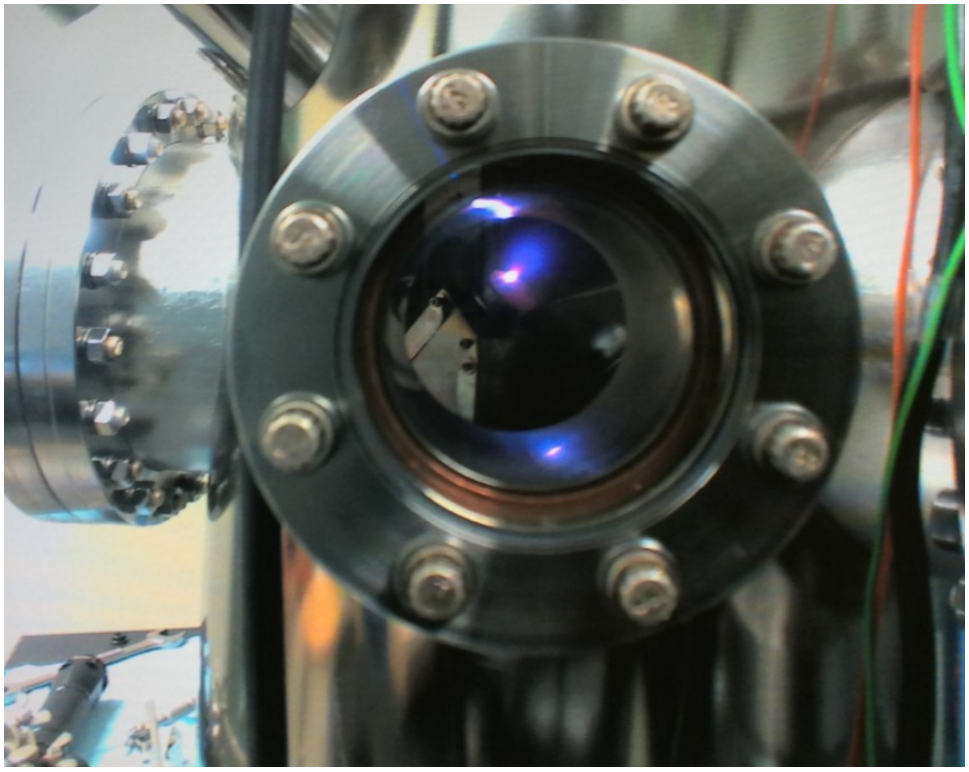

Figure 3.4 Photograph of PLD system for piezoelectric AlN thin film growth. (a) Ultra-high vacuum chamber. (b) Optical components.

material ablate at the same time regardless of the partial binding energies. Considering the flexibility of choosing the background gas in ultra-high vacuum chamber, it allows PLD for depositing various kinds of materials, such as high temperature superconductors, metals, oxides, nitrides, carbides, polymers, etc. [106].

In this case, AlN thin film growth takes place inside an ultra-high vacuum chamber stainless steel vacuum chamber by PLD. The chamber is continuously evacuated to a base pressure lower than 8×10^{-6} Torr by a mechanical pump connected with a turbo-molecular pump. A pulsed KrF excimer laser (LPX200, Lambda Physik) with a wavelength of 248 nm was used as the laser source to ablate a stoichiometric hot compressed AlN target (99.8% purity, Kurt J. Lesker). An external motor is used to rotate the AlN target holder at a constant speed during the PLD process. The laser energy at its output was fixed at 300 mJ and the repetition rate was set to 10 Hz. It is observed that the background pressure

quickly rose to 1.1×10^{-5} Torr once the ablation process took place and the plasma plume was generated in the vacuum chamber. The deposition temperature, which was set as room temperature (22°C), was measured in real-time by a thermocouple embedded in the substrate holder. The ablated plasma plume was ejected with the orientation of 45° to the target and deposited onto the substrate which was mounted 4 cm away. During the PLD process, the substrate was also rotated by another external motor with a constant speed in order to obtain uniformly grow AlN thin film on the substrate. The AlN thin film growth by PLD system describe above on a 2-inch silicon wafer, as well as the stoichiometric hot compressed AlN target is shown in Figure 3.5.

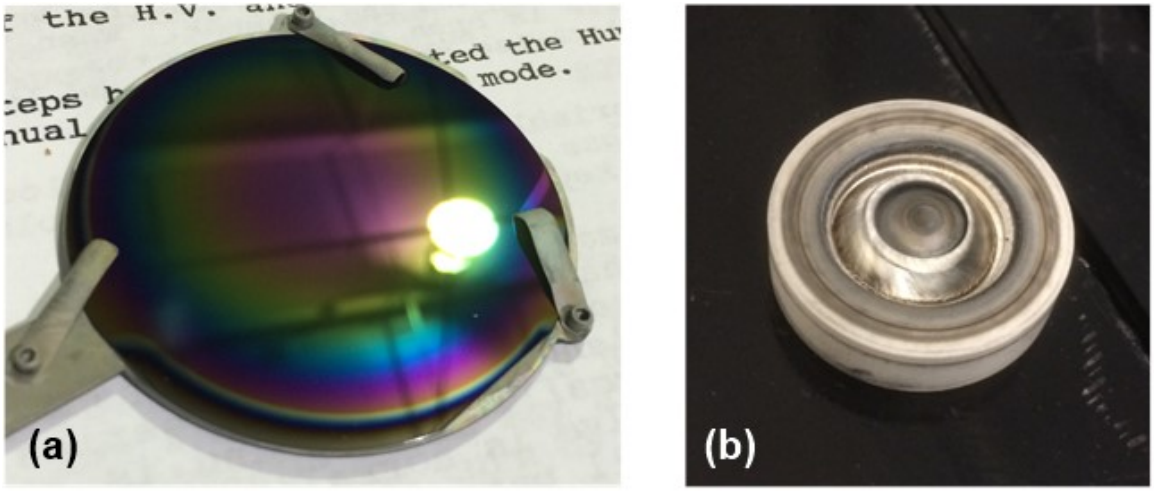

Figure 3.5 (a) AlN thin film grown on silicon wafer at room temperature. (b) Stoichiometric hot compressed AlN target which has experienced high energy pulsed laser ablation.

3.2 Characteristics of AlN Nanogenerator

In order to measure the thickness of AlN thin film growth by PLD, a 2-inch silicon wafer with half of the area covered by mask was used as a substrate for preparing the sample. In this case, an advanced stylus contact surface profiler (NanoMap-500LS, AEP Technology) was utilized to make a line scan across the border between silicon area and AlN area on the wafer (shown in Figure 3.6). When stylus scan across the border, there is a dramatic

change of the Z-position of the stylus, which indicated that the thickness of AlN thin film is around 400 nm. Besides, by using AFM (Nanoscope IV Multimode), the topography and a sectional profile of the grown AlN thin film obtained as shown in Figure 3.7.

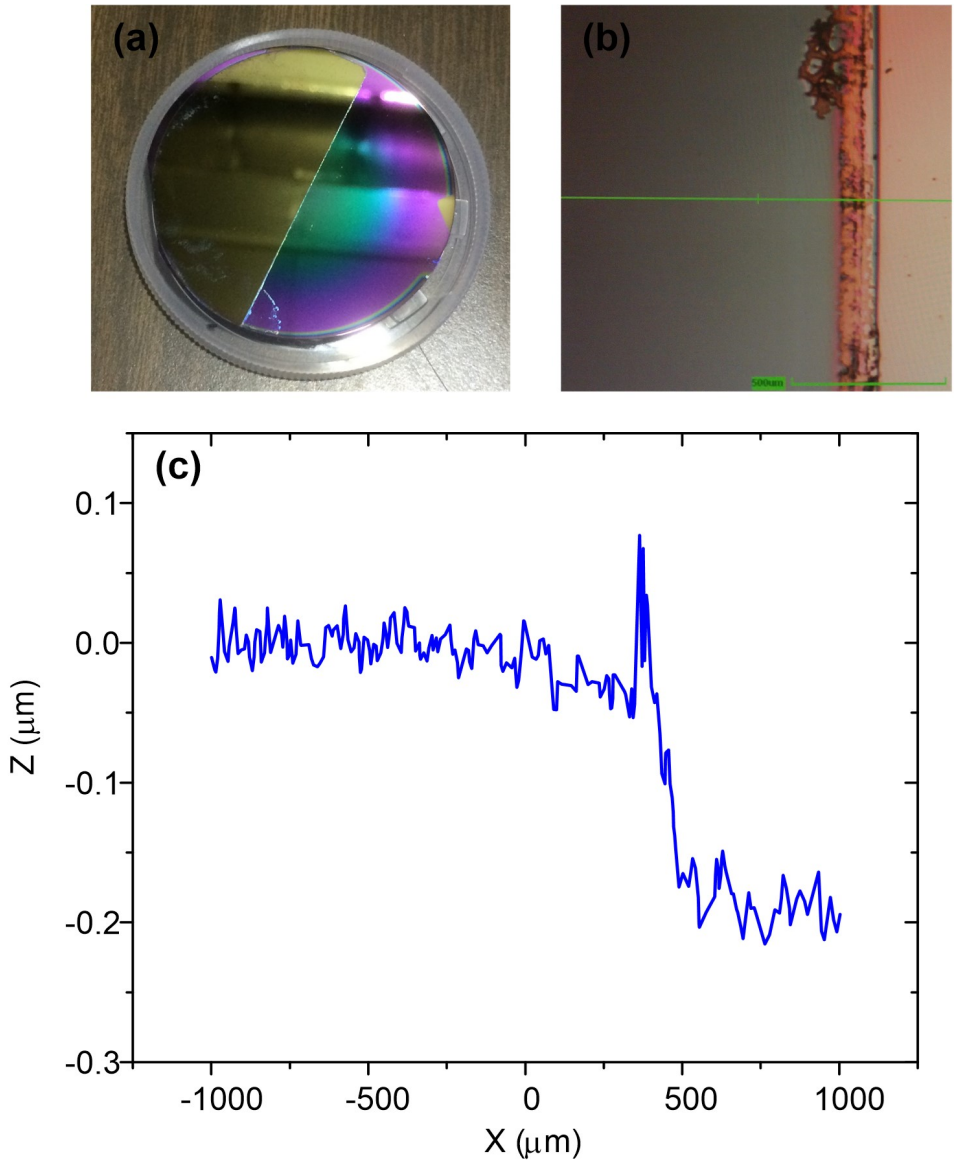

Figure 3.6 Thickness measurement of AlN thin film grown by PLD. (a) Sample for measurement. (b) Optical image showing the border on the sample. (c) Profile of the sample.

To determine the ATF-NG crystallographic characteristics, transmission electron microscopy (TEM, JEOL 2200FS) analysis was carried out. Figure 3.8 show a TEM image of AlN thin film growth by PLD at room temperature in the selected area, indicating AlN

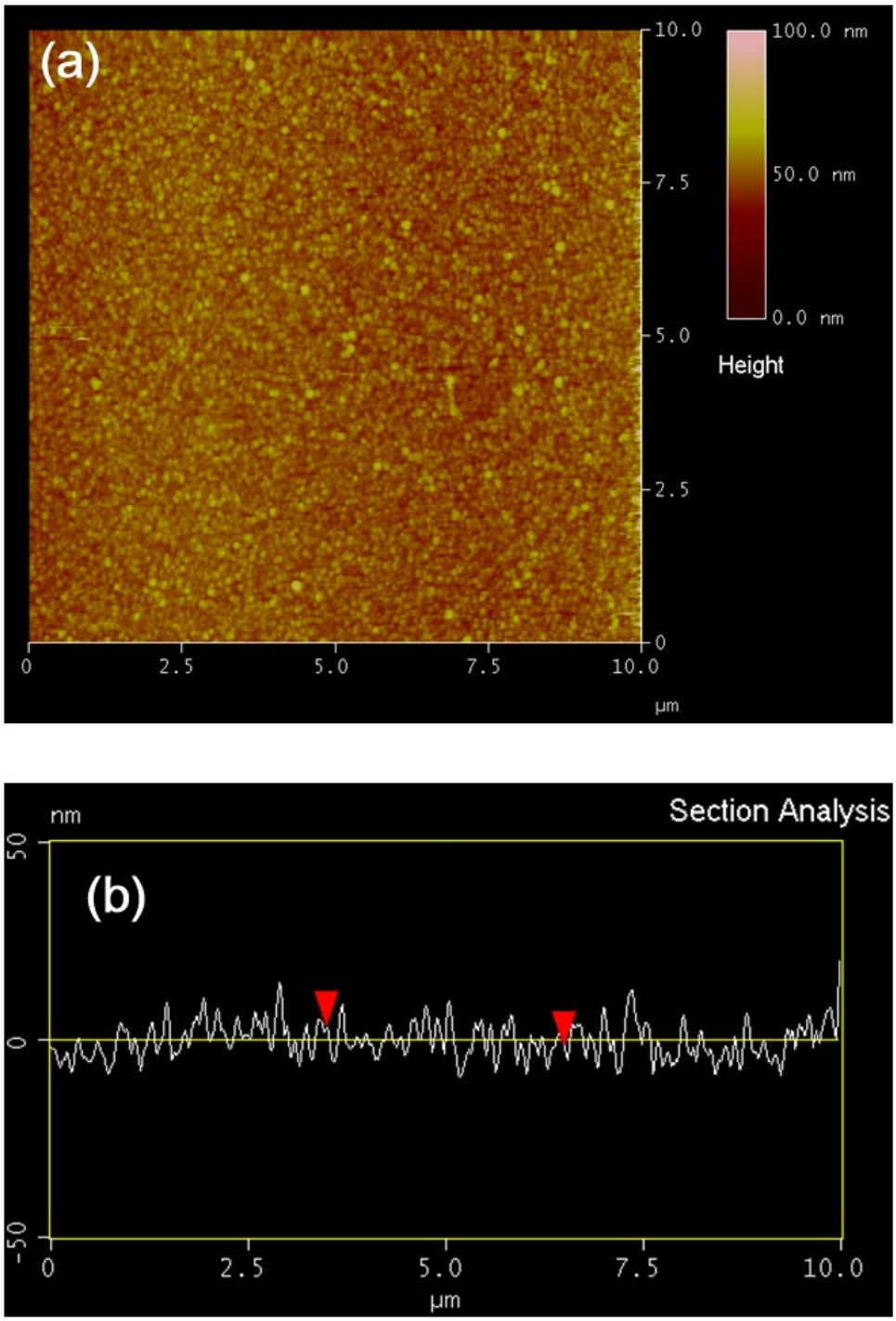

Figure 3.7 (a) Topography and (b) a sectional profile of the AlN thin film grown by PLD.

nanoparticles grown mainly along the [100] direction and the lattice parameter of a is around 2.3Å. The TEM results obtained for the AlN thin film reveals the presence of randomly oriented small crystallized particles with wurtzite structure of AlN embedded in an amorphous

matrix.

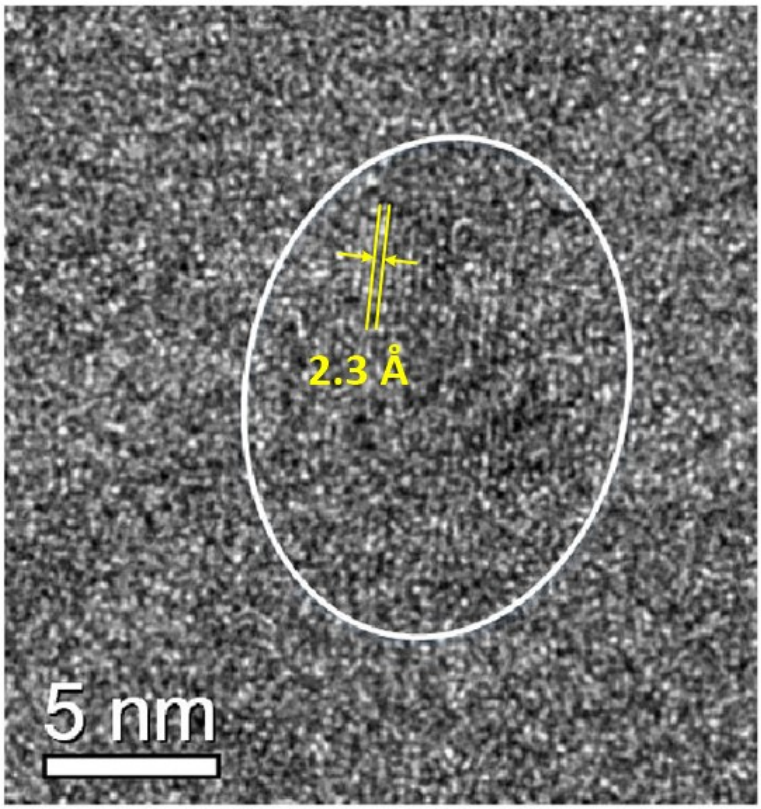

Figure 3.8 TEM image of the AlN thin film growth by PLD at room temperature.

In addition, crystal structure and crystallinity of AlN thin film was characterized by X-ray diffraction (XRD) by Bruker-AXS D8 Discover diffractometer with Cu K-α_1 radiation. XRD spectrum of the AlN thin film growth by PLD at room temperature is shown in Figure 3.9.

3.3 Piezoelectric Response Calibration by PFM

To characterize the fundamental piezoelectric properties of ATF-NG, we measured the magnitude of the effective longitudinal piezoelectric constant d_{33} of the AlN thin film using piezoresponse force microscope (PFM) (NanoMan AFM, Bruck). PFM techniques have been used in the past to study piezoelectric phenomena [107]. The photograph and the schematic

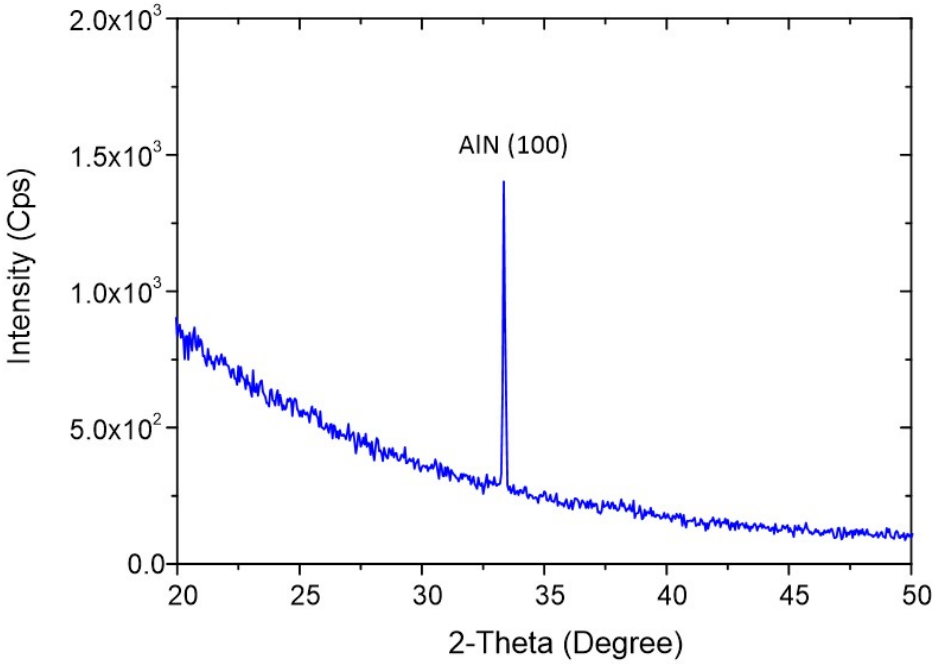

Figure 3.9 XRD spectrum of the AlN thin film growth by PLD at room temperature.

illustration of the PFM measurement for the fabricated AlN thin film is illustrated in Figure 3.10.

An alternating voltage was applied to a platinum-iridium coated conductive tip (radius 25 nm, Bruker CONTV-PT) in contact with a AlN sample induces mechanical vibrations in the sample, which can be demodulated with lock-in techniques. An AC bias voltage with amplitude ranged from 0 to 10 V was applied the tip and the bottom electrode. The frequency is set to 2 kHz in order to avoid mechanically oscillating of tip at its resonant frequency (13 kHz). Since both electrostatic forces and the electromechanical response of the surface could contribute to the measured signal, a silicon sample is measured in order to estimate background in PFM. Silicon does not exhibit the inverse piezoelectric effect, thus the amplitude measured on silicon sample was considered as the background. The slope of the piezoresponse amplitude versus modulation voltage amplitude (Figure 3.11) was determined by eliminating the effect of background, resulting in an effective piezoelectric coefficient d_{33}^{eff}. Most application of piezoelectric thin films are based on structure, where

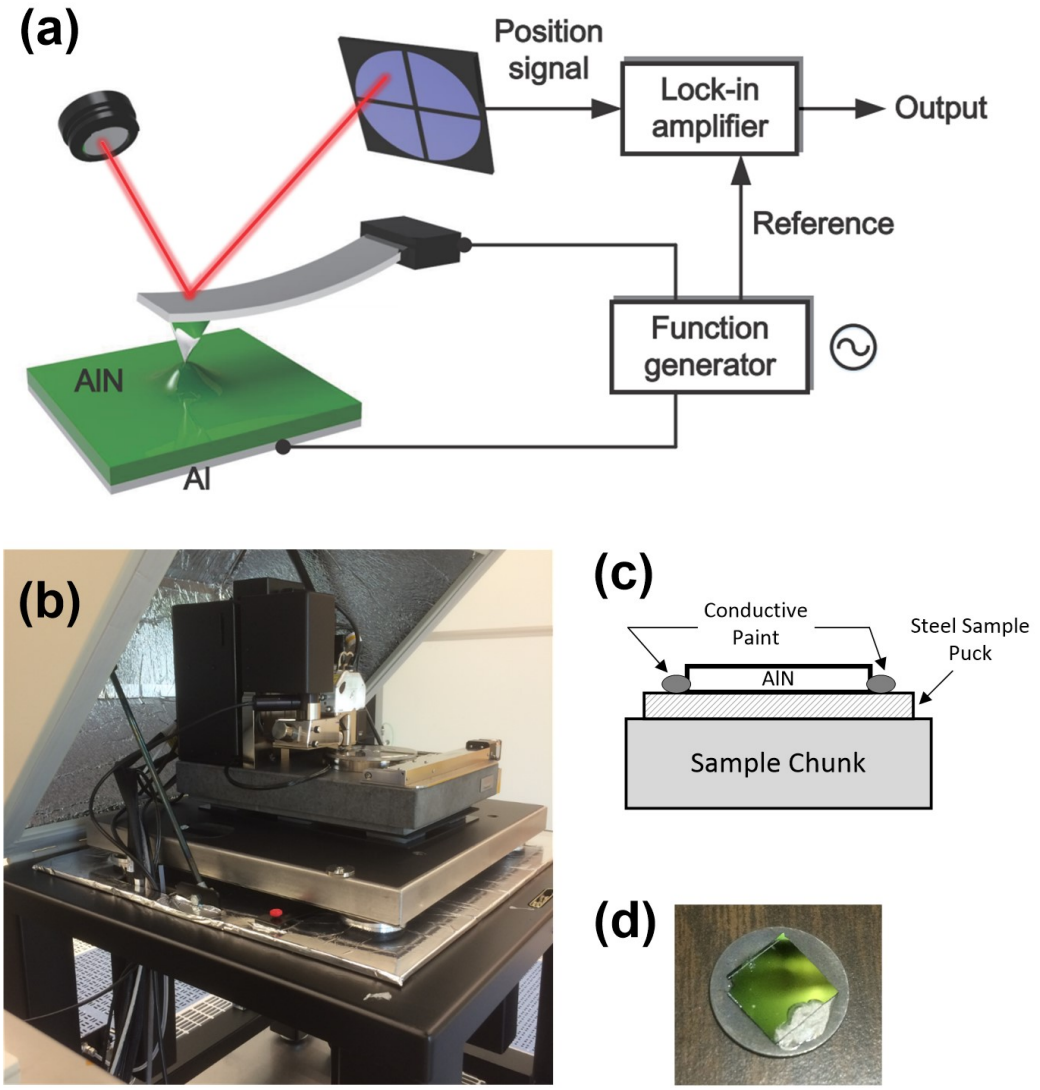

Figure 3.10 PFM measurement for AlN thin film. (a) Schematic illustration of the principle of PFM. (b) Photograph of PFM setup. (c) Structure of the prepared sample. (d) Photograph of the prepared sample.

the piezoelectric film is rigidly clamped to a substrate. The substrate then constrains the in-plane contraction and expansion of the film. Thus, only an effective value of d_{33}^{eff} instead of d_{33} is measured. The effective piezoelectric coefficient of (100)-oriented AlN thin film under lateral full constraint boundary conditions is given by [108]

$$d_{33}^{eff} \cong d_{33} - \frac{2S_{13}}{S_{11}+S_{12}} d_{31} \tag{3.1}$$

According to Tonisch et al. [109], the values of elastic constants are $S_{11} = 3.0$, $S_{12} = -0.9$

and $S_{13} = -0.6$ in $10^{-12}m^2/N$;d_{31} is assumed to be $d_{33}^{eff}/2$. Thus, using Equation 3.1, the unclamped value d_{33} of (100)-oriented AlN thin film is calculated to be 8.2 pm/V. The study of piezoelectric properties of AlN sample with PFM allowed the observation of a strong piezoelectric response.

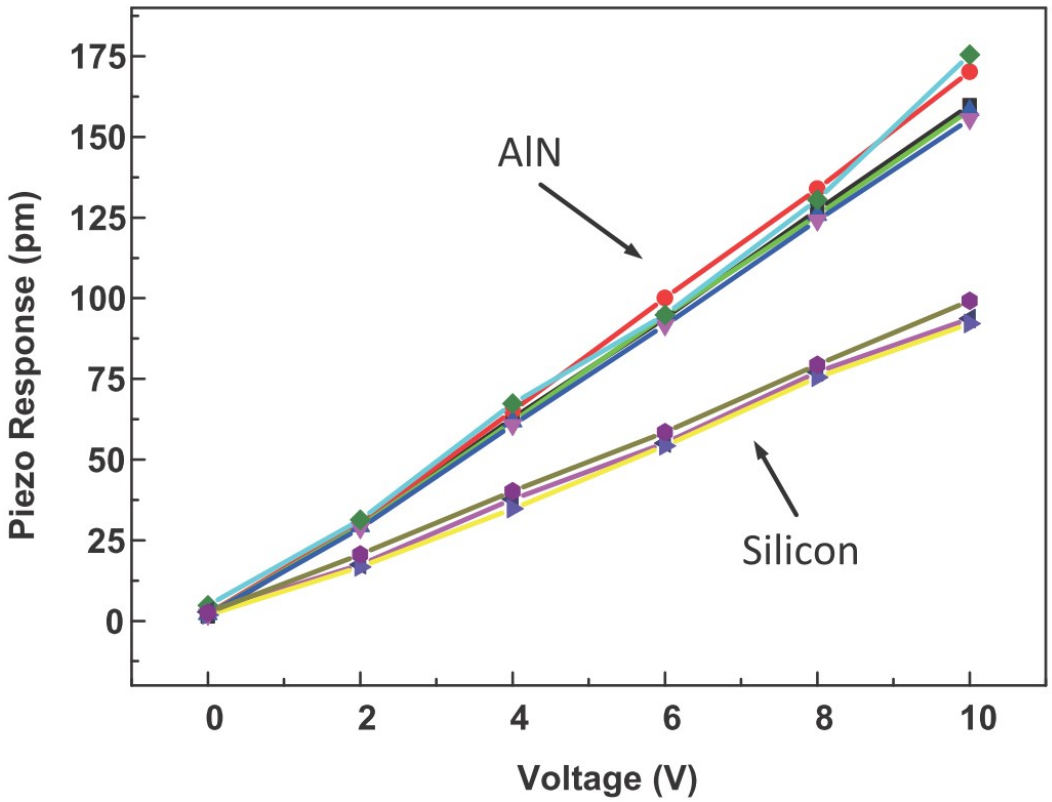

Figure 3.11 Piezoresponse amplitude vs. modulating AC bias voltage amplitude for AlN thin film.

Table 3.1 presents the values of the piezoelectric coefficient of the (002)-oriented AlN and (002)-oriented ZnO thin film. As can be seen in the literatures that the d_{33} piezoelectric constant of (100)-oriented AlN thin film deposited by PLD at room temperature in vacuum environment is as high as those obtained in the case of (002)-oriented AlN thin films [110, 111, 112], and is also comparable to those (002)-oriented ZnO thin films [113, 114, 115].

Table 3.1 Measured effective piezoelectric coefficient

	$d_{33}(pm/V)$	*Literature*
AlN(002)	5.4	Tonisch et al.[110]
	3.4	Dubois et al.[111]
	$4.6 - 5.2$	Mortet et al.[112]
ZnO(002)	11.7	Ellmer et al.[115]
	13	Christman et al.[114]
	5.9	Gualtieri et al.[113]
AlN(100)	$2.3 - 3.8$	Cibert et al.[116]
	5.9	This work

3.4 Fabrication of AlN-based Thin Film Nanogenerator (ATF-NG)

Herein, the fabrication process of a bio-compatible flexible nanogenerator based on (100)-orientation nanocrystalline AlN thin film grown by PLD at room temperature is described. The schematic illustration of the fabrication process of ATF-NG is shown in Figure 3.12.

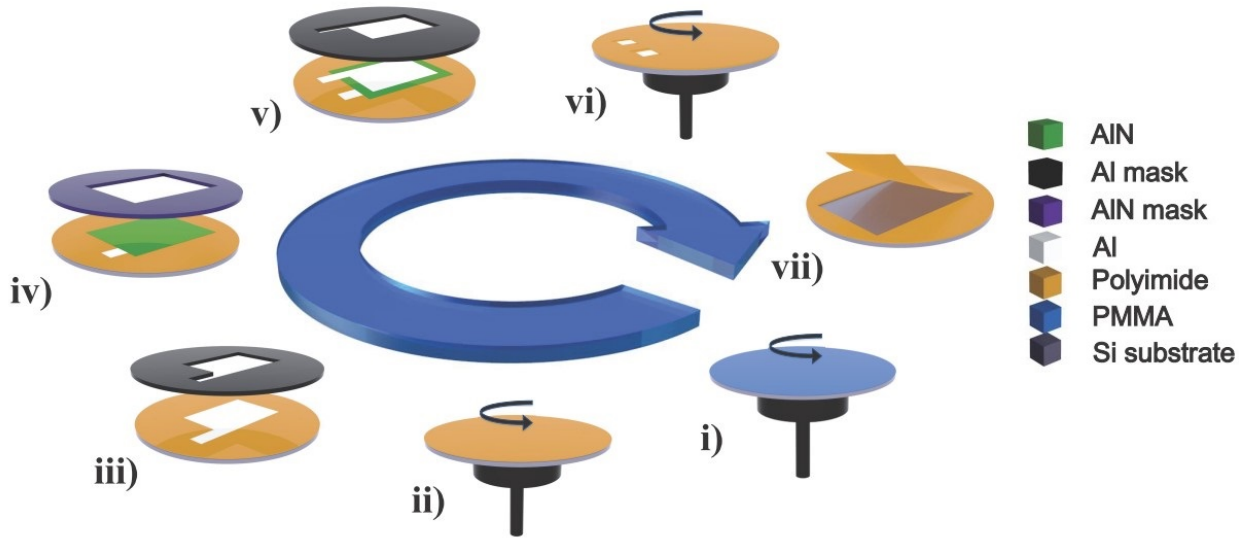

Figure 3.12 Schematic structure of the process for fabricating ATF-NG.

A 2-inch silicon wafer was first spin-coated a layer of PMMA (495 A6, MicroChem) at 3000 rpm for 1 min, followed by a layer of polyimide (PI-2525, HD MicroSystem) at 1500 rpm for 1 min. After curing, a layer of aluminum thin film was deposited by a thermal

evaporation system, as shown in Figure 3.13. Evaporation takes place in a vacuum chamber which was evacuated by a turbo-molecular pump to a base pressure of 7 mTorr. After that, the AlN thin film was deposited inside the stainless steel vacuum chamber by PLD process as described before.

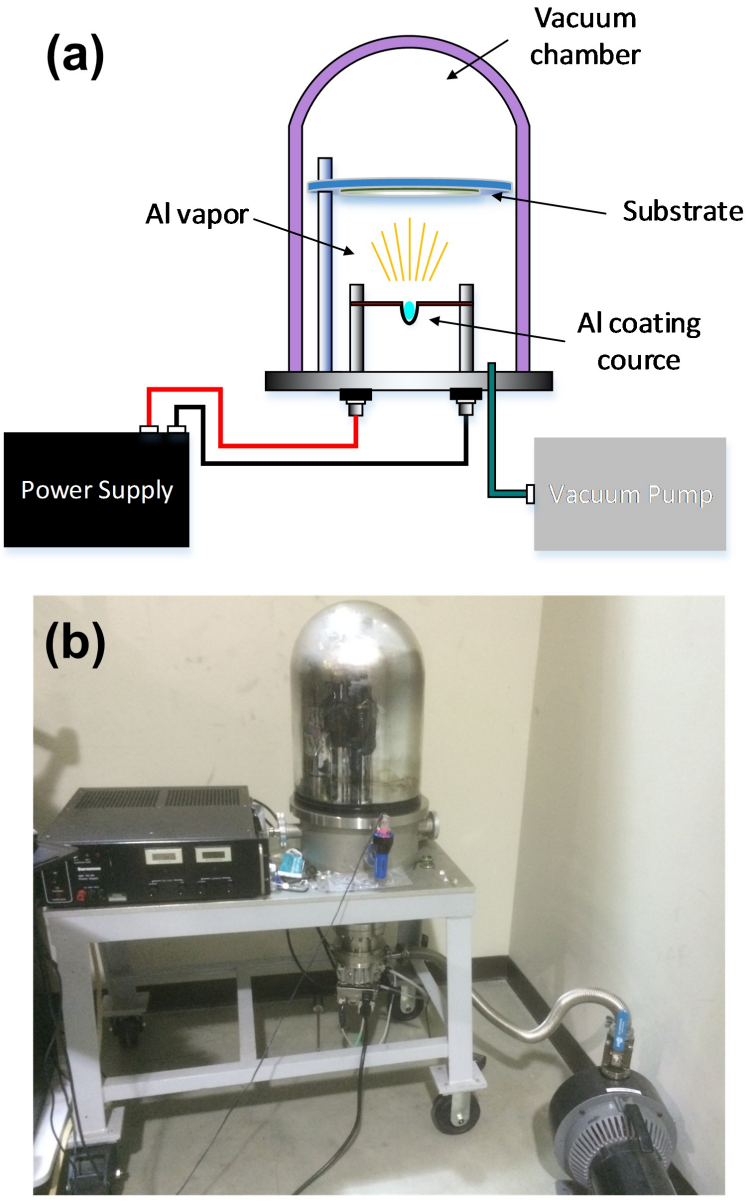

Figure 3.13 Thermal evaporation system for Al thin film deposition. (a) Schematic illustration. (b) Photograph of the system.

Then, the second layer of aluminum thin film was deposited on top of the AlN thin film,

followed by spin-coating the second layer of polyimide at 1500 rpm for 1 min. Before spin-coated the top polyimide, both electrode part of the two aluminum layers were covered with PTFE tape, which would be removed before PI curing. This step opens two windows for wire leads which were connected to the two electrodes using silver paste. After immersing the wafer into acetone for 2 hours, the underlying PMMA layer was dissolved and the device was released from the wafer.

Exploded-view schematic illustration of ATF-NG is shown in Figure 3.14. The AlN thin film deposited at room temperature by PLD is sandwiched between two layers of Al. The top and bottom aluminum layers are used as the positive and negative electrodes, respectively. AlN has the advantage of a much higher electric resistance, high breakdown voltage and low dielectric loss. Lee et al. used of one or more AlN interlayers to provide high potential barriers, and help to prevent short circuits between the ZnO nanowires and the upper deposited electrode [117]. Herein, the AlN layers in the developed ATF-NG not only generate piezoelectric potential under external stress and act as an energy generation source, but also serves as insulating interlays which provides a high potential barrier for preventing undesirable current leakage through the device interior. Polyimide films serves as the protective layer due to its outstanding reliability and durability, with a unique combination of electrical, thermal, chemical and mechanical properties. Polyimide packaging over the entire structure can further enhance mechanical robustness and protect the device from invasive chemicals, which is suitable for implantable biomedical devices.

Figure 3.15 shows an optical image of the developed ATF-NG along the axial of a glass tube. It can be seen the fabricated ATF-NG features a thin film structure with good flexibility, which allows for easily bending. In order to examine the cross-section of the Al-AlN-Al three layers structure, the same fabrication process described above was used to grow Al (by evaporation), AlN (by PLD) and Al (by evaporation) in consequence on a 2-inch silicon wafer. The cross-section of this sample was characterized by using a field-emission SEM (FE-SEM, Carl Zeiss AURIGA). The cross-sectional SEM image of Al-AlN-Al stacked structure

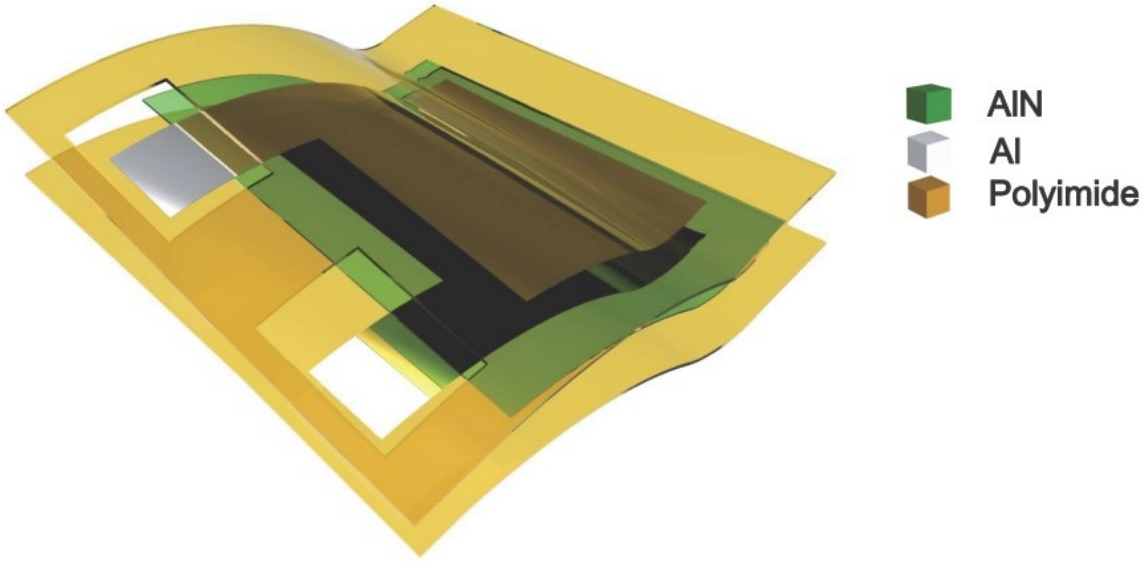

Figure 3.14 Exploded-view schematic illustration of the developed ATF-NG.

is shown in Figure 3.16.

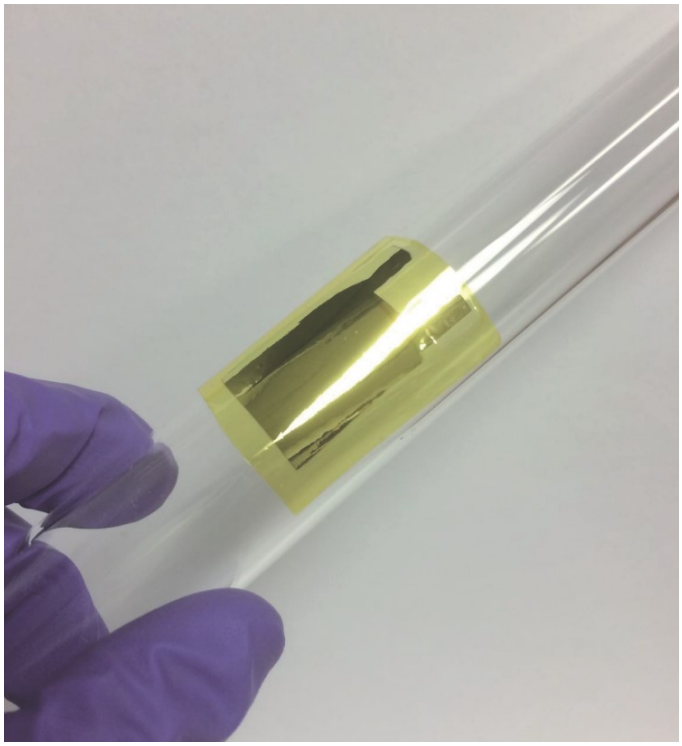

Figure 3.15 Optical image of the developed ATF-NG along the axial of a glass tube.

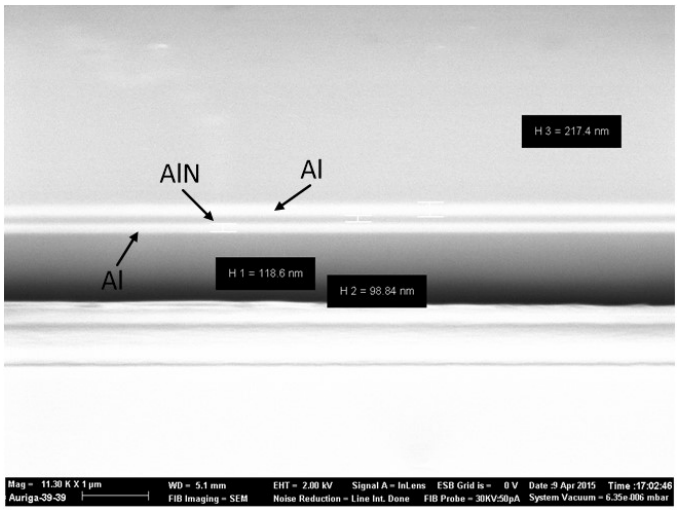

Figure 3.16 Cross-sectional SEM image of Al-AlN-Al stacked structure.

3.5 Performance of ATF-NG

To verify the performance of the ATF-NG, we measured the open-circuit voltage using a low-noise nanovoltmeter (2182A, Keithley). During the measurement, the ATF-NG was repeatedly deformed and restored in a cyclic stretching-releasing agitation (0.35 Hz) by using a linear motion stage. Photographs of ATF-NG in original state and bending state by the linear motion stage is shown in Figure 3.17.

Figure 3.18 shows the open-circuit voltages measured from ATF-NG when they were bent periodically under strain of 0.08% at a strain rate of 0.4% s^{-1} and subsequently released. A set of positive and negative pulses were generated during a single cycle of bending and release motions. ATF-NG shows open-circuit voltage of 10 mV. To ensure that the measured signals were not caused by the measurement instruments themselves but were induced purely by the ATF-NG alone, switching polarity tests were also carried out. As can be seen, the generated voltage pulses were inverted obviously with the same amplitude. The durability test and further characterization were performed, which prove the stability and robustness of the ATF-NG.

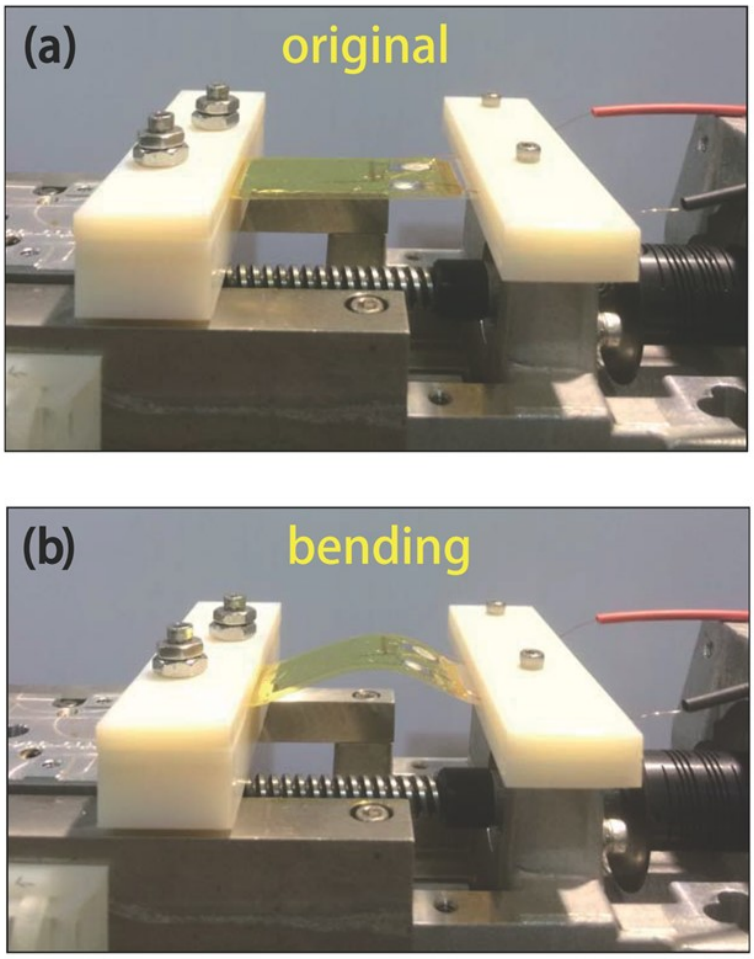

Figure 3.17 Photographs of ATF-NG in (a) original state and (b) bending state by the linear motion stage.

3.6 Summary

This chapter presents a bio-compatible, super-flexible, lightweight piezoelectric AlN thin film nanogenerator. By utilizing PLD, (100)-orientation AlN thin film is grown at room temperature without any background gas. TEM and XRD image reveals that unlike (001)-orientation AlN film which crystallizes and consists numerous oriented columnar grains that are perpendicular to the surface of the substrate, the deposited AlN crystallized particles randomly embedded in an amorphous matrix. PFM measurement indicated that the (100)-orientation AlN thin film exhibits a strong piezoelectric response, which is at the same level

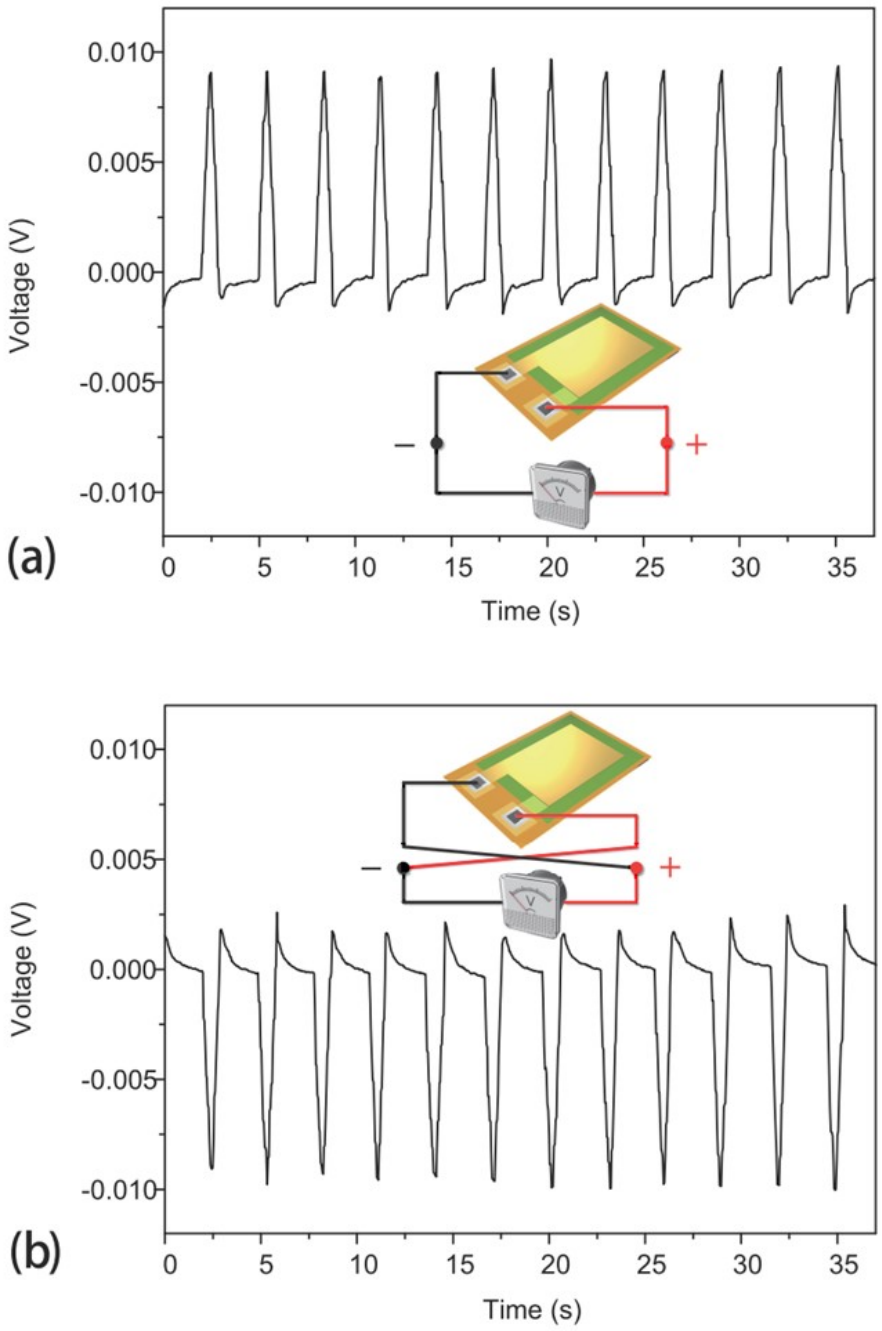

Figure 3.18 Open-circuit voltage measurement for ATF-NG in the (a) forward connection and (b) reverse connection.

of piezoelectric coefficient as the c-axis AlN and ZnO. The flexible nanogenerator based on (100)-orientation AlN was encapsulated by two layers of polyimide thin film. Periodical bending/unbending motions experiment validate that abilities of the developed nanogenera-

tor, which could opens a door towards the realization of self-powered flexible electronics and biomedical devices. It is worth mentioning that although the AlN thin film nanogenerator exhibits the same level of piezoelectric effect as its competitor ZnO. the goal of pursuing higher mechanical-electrical energy conversion efficiency guides more efforts to be made to develop new-style of flexible nanogenerators.

CHAPTER 4

FLEXIBLE AND BIOCOMPATIBLE FENG – RATIONALE & APPLICATIONS

Personal electronics are advancing toward an era where the pursuit of multifunctionality and wearability has become an important trend [118, 119, 120, 121, 122, 123]. Similarly to the recent developments in flexible light-emitting diodes (LEDs), artificial skin, and stretchable electronics [124, 125, 126, 127, 128, 129, 130], devices designed to harvest small sources of mechanical energy should address the issues of lightweight, flexibility, and biocompatibility. This will make the technology to be portable and compatible with smart electronics [118, 131, 132, 133], ultimately defining the path toward self-powered wearable devices. The prevailing mechanisms of thin film-based mechanical energy harvesting have been limited to conversion based on piezoelectric effect [134, 135, 136]. Recently, Wang and co-workers revolutionized the field by inventing triboelectric nanogenerators (TENGs) which are capable of generating very high voltages [137]. Their work is continuously advancing to further enhance efficiency of TENGs [138, 139, 140].

In this chapter, a different operating mechanism to the field of flexible thin film nanogenerators based on polypropylene ferroelectret (PPFE) which harvest mechanical energy from human motion is introduced. It demonstrate flexible, foldable, biocompatible, highly efficient thin film ferroelectret nanogenerators (FENGs). The devices comply with the flexibility, wearability, lightweight, and portability demands mentioned earlier. A FENG with surface area more than 300 cm^2 is demonstrated in this paper by using bar-coating technique [141]; they can also be folded to sizes smaller than 1 cm^2 and generate higher electric potentials. Furthermore, their simple fabrication allows for encapsulated low-cost devices. In view of the environment, health, and safety [142], the fabrication of encapsulated FENG avoids the use of harmful elements (e.g. lead) or toxic materials (e.g. carbon nanotubes),

making it more attractive for biocompatible and perhaps even implantable applications. Through finite element method (FEM), the mechanical-electrical energy conversion mechanism of FENG was studied; and the relationship between internal stress, change of electric filed, and charge transport are investigated. Due to its thin film structure, the device can be bent or even folded easily. Further experiments show that both the open-circuit voltage (V_{oc}) and short-circuit current (I_{sc}) are doubled with each folding along an axis of symmetry. Since V_{oc} and I_{sc} are doubled with each folding action, the output power of the FENG can be easily and significantly increased. We also study the electrical output produced by the device for time-dependent mechanical input. Additionally, device electrical output for different pressure input magnitudes (while keeping the frequency constant), and for different frequencies (while keeping the magnitude constant) are investigated. The results revealed the frequency- and pressure-dependent properties of the developed device. Finally, we developed FENG-based systems for three niche applications: *1) Illumination:* we demonstrate that the energy harvested by a stacked FENG (60 mm $\times$ 60 mm, 7 layers) is able to power 20 commercial green and blue LEDs connected in series; *2) Self-powered touch liquid crystal display (LCD):* this touch screen scavenges energy from finger touch to supply power during operation; and *3) Flexible/foldable keyboard:* this thin film-based keyboard is powered by harvested energy from each keystroke, and its size can be reduced by simple folding, thus enabling portability.

4.1 Operating Mechanism of FENG

Polypropylene (PP) foams are good thermal insulators with a high mechanical strength-to-weight ratio. The active material in the developed FENGs are prepared by starting with PP film containing tiny foreign inorganic particles (e.g. silicates). When the film experiences stretching in two perpendicular directions, the inorganic particles serve as a stress concentrator or microcracks resulting in lens-shaped voids in the PP film. During

this process, high pressure (e.g. 5 MPa) nitrogen or carbon dioxide diffuse into the film which is full of voids, so that the internal pressure within the voids becomes equal to the external pressure. Subsequently, the external gas pressure is suddenly released, resulting in dramatically swell of those voids in PP film. For the purpose of stabilizing and stiffening the swelling voids at room temperature, thermal treatment (usually higher than 100°C) is carried out to increase the crystallinity of the polymer matrix [143, 144, 145].

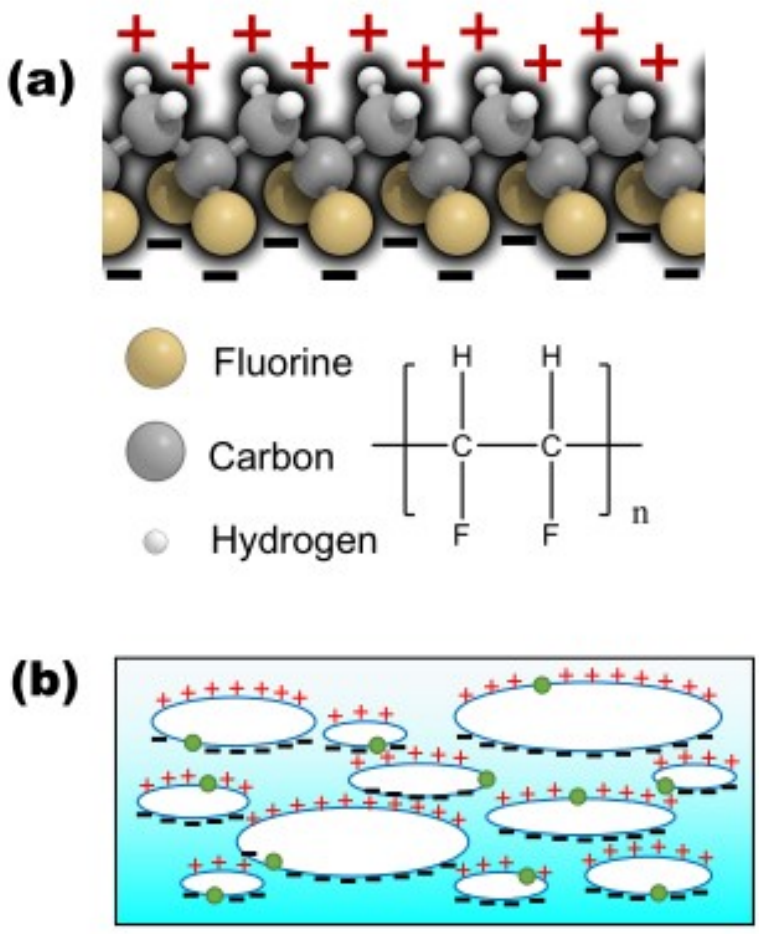

Figure 4.1 Schematic illustration of the comparison between polyvinylidene fluoride (PVDF) and FENG. (a) Molecular structure of piezoelectric β-phase PVDF. (b) Bipolar voids and charge distribution of PPFE after microplasma discharging, showing that the upper and lower surfaces of the voids are oppositely charged. Green spheres indicate foreign particles that facilitate void formation.

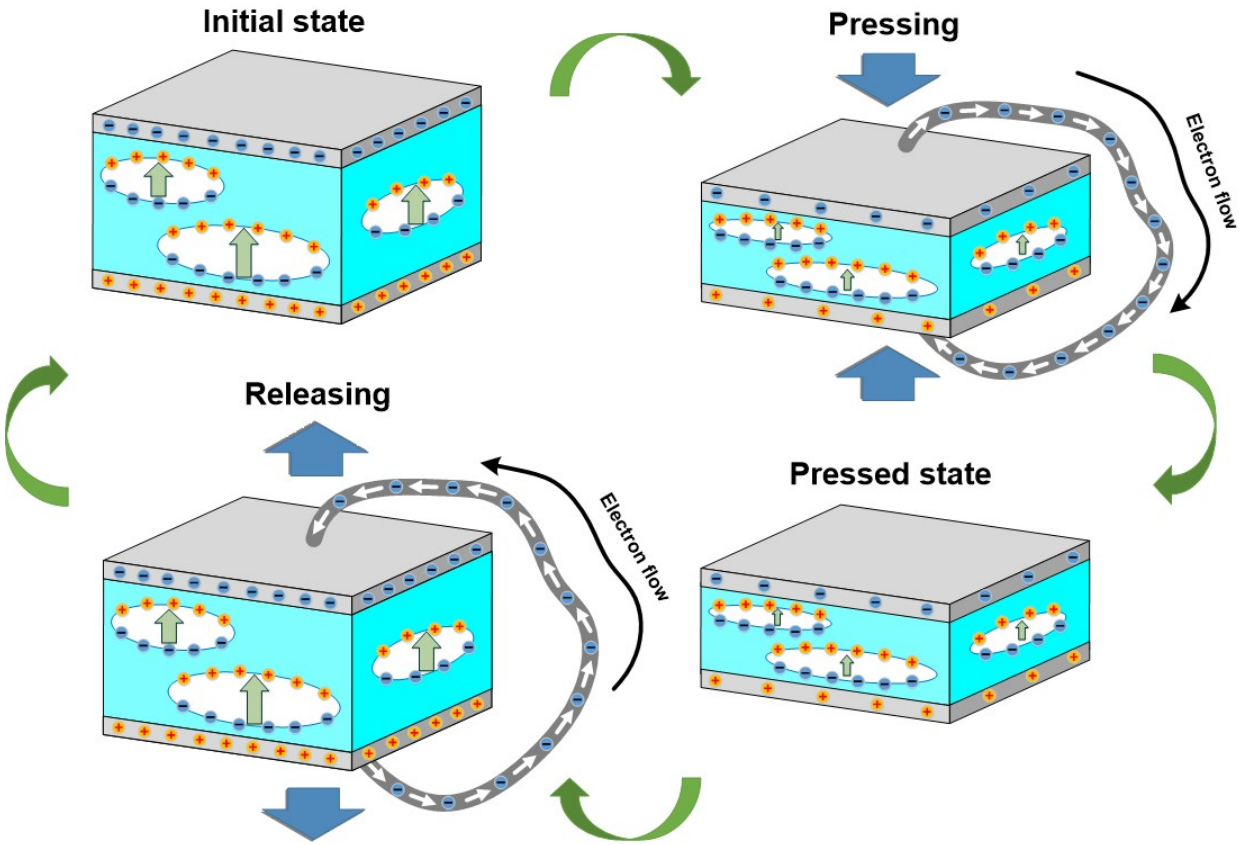

Figure 4.2 Schematic illustration of the operating principle of the FENG, showing the a press-release cycle and corresponding dipole and charge dynamics of FENG.

Unlike ferroelectric materials which have a spontaneous electric polarization, PP films are completely nonpolar materials unless the internal voids are charged by dielectric barrier microdischarges [144, 146]. By means of plasma discharges in the voids of PP foam, completely non-polar materials without any molecular dipole can behave like ferroelectrics. Although the PPFE would exhibit the same macroscopic behavior as traditional well-known piezoelectric polymers or piezocomposite [141, 147], their microscopic operating principles are different. For β-phase PVDF, which is the most commonly used piezopolymer in electromechanical devices [148], the hydrogen atoms have net positive charge and the fluorine atoms have net negative charge (Figure 4.1). The lattice parameters of β-phase PVDF are a=8.64 Å, b=4.82 Å and c=2.64 Å [149], whereas the dipole dimensions in the PPFE are determined by the sizes of the charged voids. By applying a large electric field to the PP film,

Paschen-breakdown occurs inside the voids [68]. The current within the air gap transfers a sheet charge density across the air gap. During microplasma discharges, charges separated by the ionization of the gas transportation under the charging field, and light flashes can be observed with the naked eye. PP foam is full of artificial voids with different size, ranging from ~ 1 μm scale to ~ 100 μm scale, which form highly oriented giant dipoles. If two conductive layers are deposited on the surfaces of the PPFE film, which functions as electrodes, then the giant dipoles in the PPFE induce charge of opposite polarity in each electrode.

The charged voids change their thickness and thus their dipole moments upon application of mechanical stress (Figure 4.2), i.e. compressing PPFE film will result in smaller dipoles moments. The change of dipole moments is capable of driving the electrons from the electrode with negative charge to the electrode with positive charge, generating a difference in potential between the electrodes (generated voltage under open circuit condition) or flow of charge from one electrode to the other (generated current under short circuit condition). This macroscopic behavior of PPFE films is very similar to that of well-known solid piezoelectric crystals, even though the microscopic origins of the observed phenomena are different. By comparison with traditional piezoelectric materials, PPFE films features with flexibility and internally charged cellular structures, which makes them highly efficient in charge storage and more sensitive to mechanical stress. More importantly, PPFE films have significantly greater piezoelectric coefficient ($d_{33} \sim 400$ pC/N) than typical piezopolymers like PVDF ($d_{33} \sim 15$ pC/N) [150], and parylene-C ($d_{33} \sim 2$ pC/N) [148].

4.2 Fabrication of Encapsulated Biocompatible FENG

The FENG is a sandwich-like metal-insulator-metal (MIM) structure which makes easy large-scale fabrication. The fabrication process of a FENG with an area of (35 mm $\times$ 25 mm) encapsulated by PI films is illustrated in Figure 4.3. A PPFE film fabricated by EMFIT Corporation with a nominal thickness of 80 μm and piezoelectric coefficient $d_{33} \sim 400$ pC/N

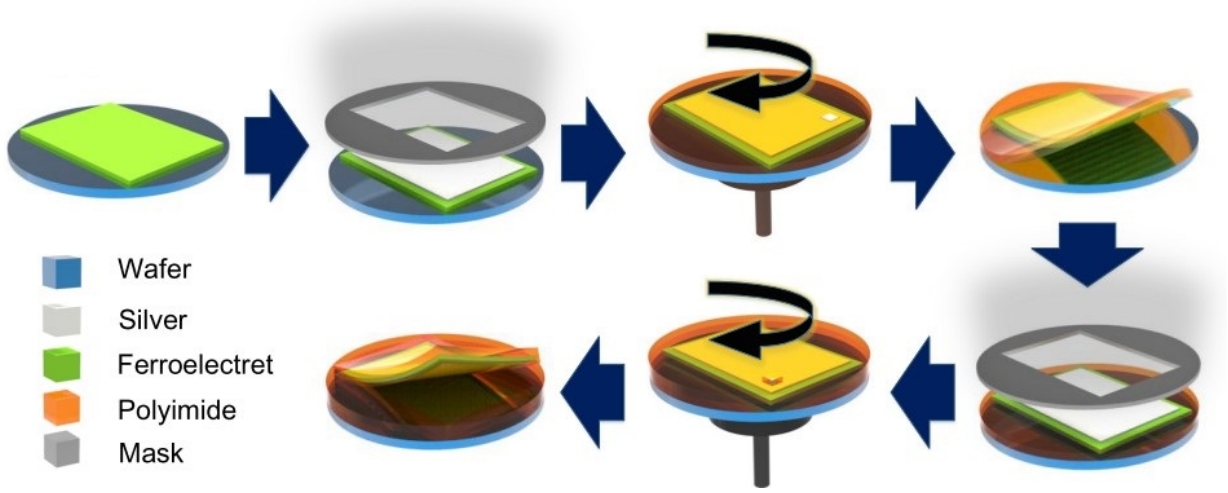

Figure 4.3 Schematic illustration of the fabrication process of encapsulated biocompatible FENG.

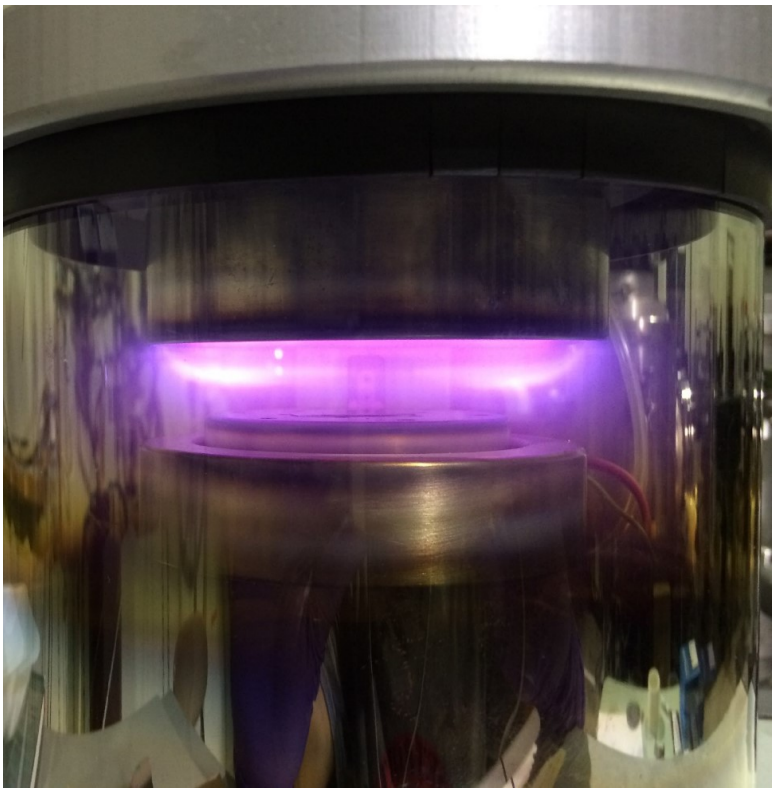

Figure 4.4 Growth of silver thin film deposition by sputtering.

serves as the insulator, and two thin silver films (500 nm in thickness) sputtered on the both sides of PPFE act as metal electrodes, as shown in Figure 4.4. Copper wires are fixed on the electrodes by using conductive paint and copper tape, providing electrical terminals

that allowed for external circuitry connections to the FENG. Due to the outstanding reliability, durability, mechanical and chemical properties, two thin spin-coated PI films serve as encapsulation layers that protect the FENG device from invasive chemicals and provide mechanical robustness. It has been demonstrated that encapsulation of a flexible device with biocompatible PI films isolates the functional part of the device from bodily fluids and tissue, thus minimizing the risks of failure or immune response in bioimplantable applications [20]. Furthermore, PI encapulation layer revealed no evidence of toxicity from *in vitro* studies with human epithelial keratinocytes [22]. Figure 4.5 provides an exploded-view schematic diagram of the fabricated FENG.

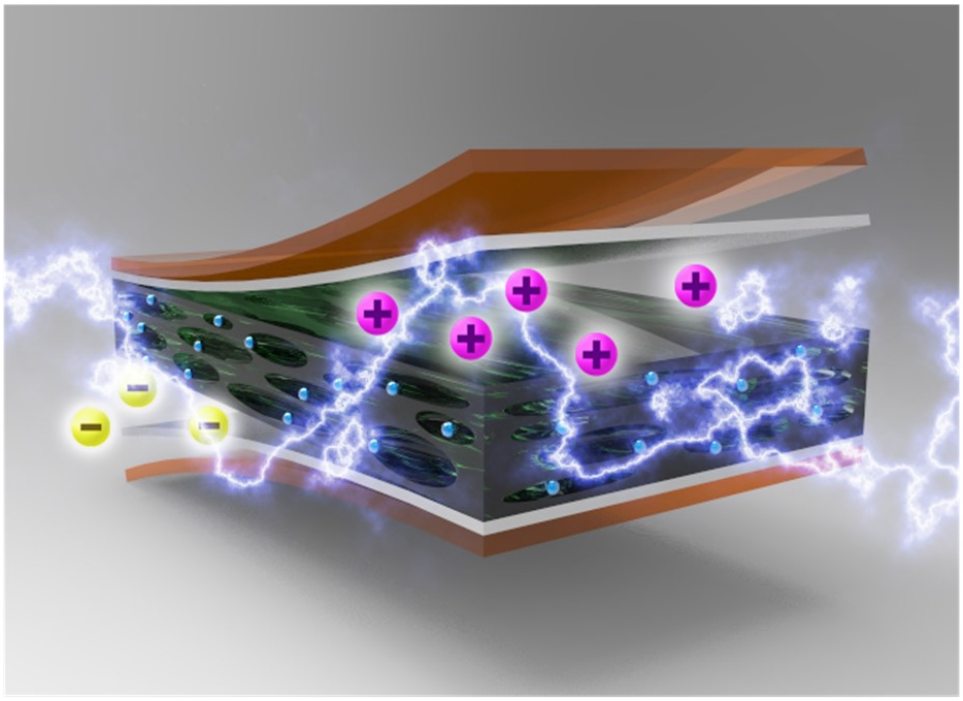

Figure 4.5 Exploded-view illustration of the encapsulated FENG, which consists of a stacked metal-PPFE-metal structure without moving parts or microfabricated features.

An SEM images of the cross-section of PP foam and an optical image of the FENG appear in Figure 4.6 (a) and (b), respectively. The use of backscattered electrons reveals good contrast and clear definition of the structure of PPFE foam film. Since the production of backscattered electrons is strongly dependent on the average atomic number of the sample,

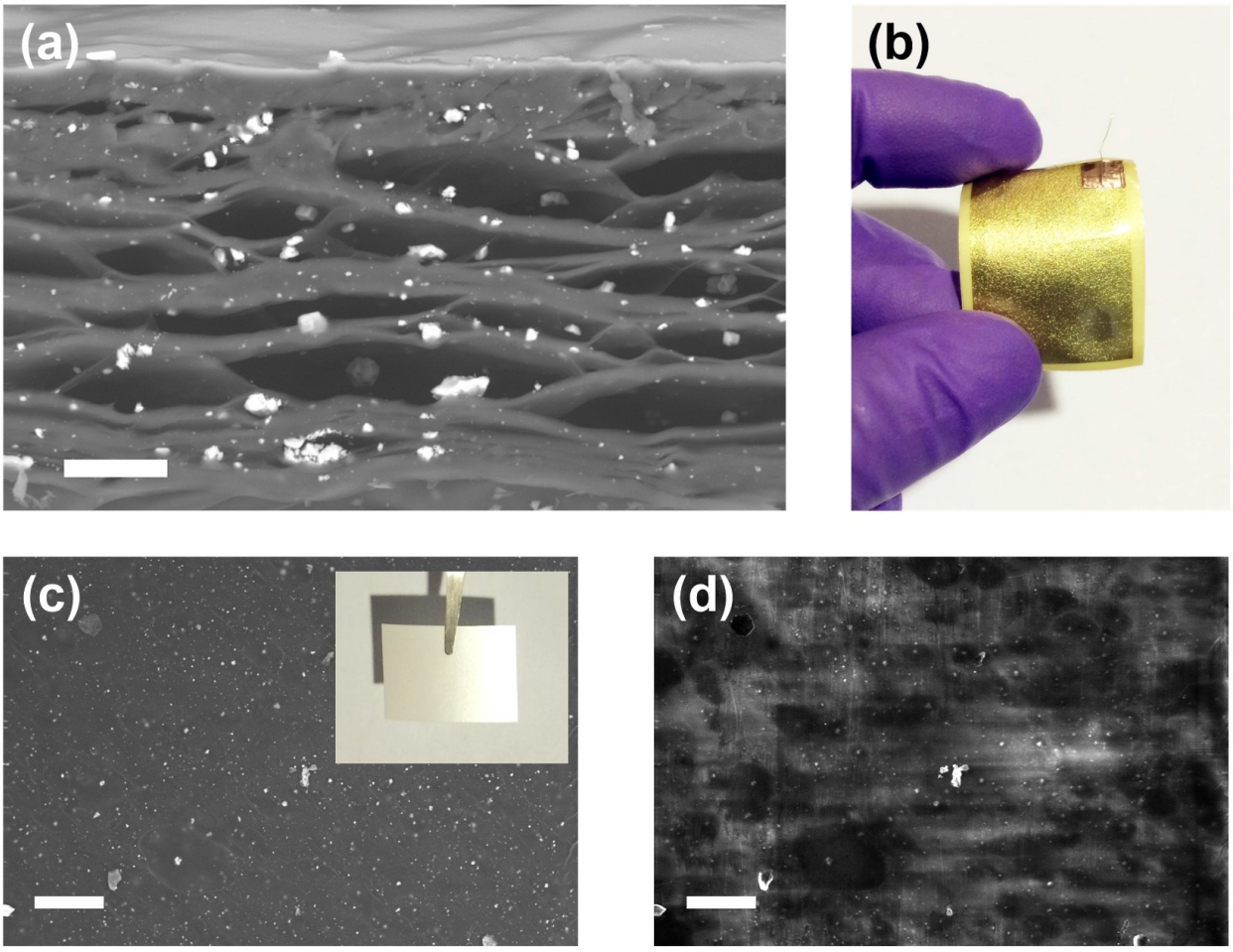

Figure 4.6 Optical and SEM images of FENG. (a) Cross-sectional backscattered electron SEM image of the PP foam, showing the cellular structure and silicate particles (brighter areas in the image). Scale bar, 20 μm. (b) Photograph of the fully encapsulated FENG bent by fingers. (c) Secondary electron SEM image of the surface of PPFE and the photograph of PPFE (inset). (d) Backscattered electron SEM image of the same area of (c). The darker regions corresponds to voids below the film's surface. Scale bar, 100 μm.

silicate particles appeared to be much brighter than their surrounding PP cellular film. The SEM image also clearly shows the bipolar voids described earlier. Figure 4.6 (c) and (d) show SEM images of the surface of the PPFE foam, using secondary and backscattered electrons, respectively. The voids in the PP foam can be identified at the dark regions in Figure 4.6 (d), where lower material density produces fewer backscattered electrons.

4.3 FEM Analysis of FENG

In order to obtain a more quantitative characterization of the energy generating ability of FENG, the electric potential and electric field distribution inside the FENG is analyzed by FEM (COMSOL Multiphysics 5.2). The model describes the charge transfer between two electrodes and it represents the first FEM model for a PPFE-based energy harvester. Figure 4.7 illustrates a schematic diagram of the constructed model. A 2-D section of FENG (80 μm $\times$ 300 μm) is filled with seven voids with different shapes and sizes and two silver electrodes (10 μm $\times$ 300 μm). The surface charge densities on the top and bottom surfaces of each void are set to 10^7 C/m^2 and -10^7 C/m^2, respectively. Both silver electrodes are set to an electric potential of 0 V (i.e. they are grounded). Figures 4.7 (b) and (c) show the calculated electric potential and electric field distribution inside the section without external pressure, respectively. It can be seen that due to the charged surfaces of each void inside the section, there is an electric potential across the surfaces of the voids as well as between them. Figure 4.7 (d) and (e) show the simulated resulting electric potential and electric field distribution when 1 MPa pressure is applied vertically to the upper surface of the film. The geometric shape of voids along with the electric potential and electric field distribution are changed due to the applied external pressure. The size, shape, and density of the voids determine the vertical stiffness of FENG, which plays an important role in its mechanical-electrical conversion ability [151, 152, 153].

Figure 4.8 (a) shows charge density distribution of the upper and lower surfaces before and after external pressure is applied. As can be seen, the upper surface accumulates negative charge while lower surface accumulates positive charge; and the shape of the charge distributions for both surfaces are the same due to the geometric symmetry of the model. Once the external pressure is applied to the upper surface, the charge distribution shape at both surfaces remains; but the absolute values of the accumulated charge at both surfaces decreased. When both electrodes are grounded, the negative charge on the upper electrode

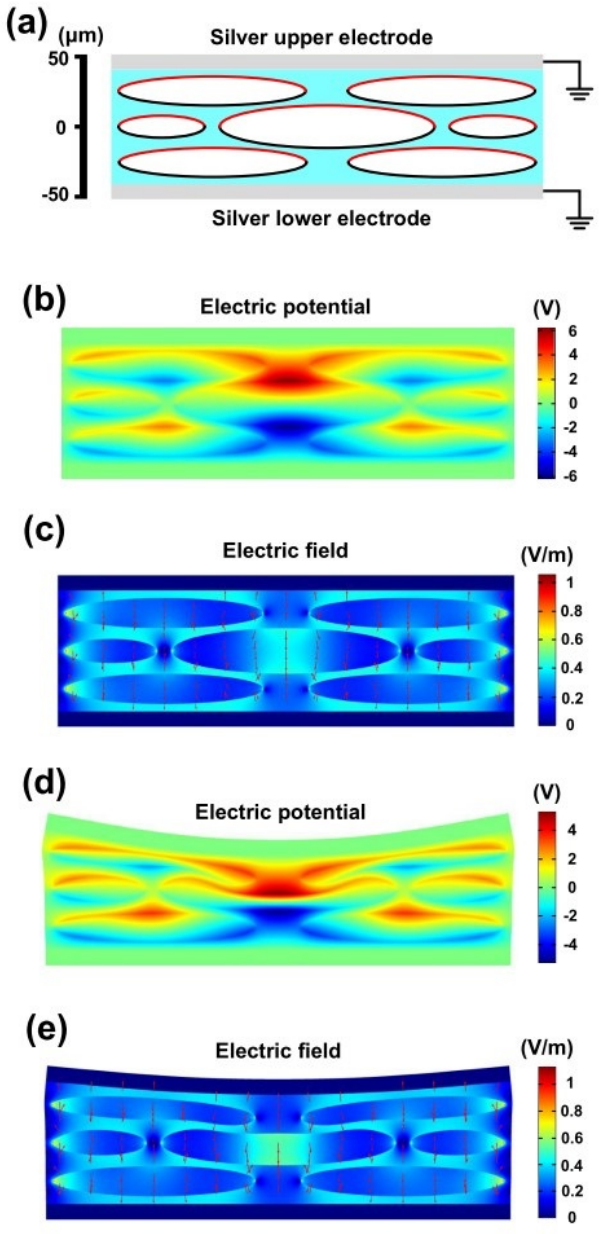

Figure 4.7 Theoretical model and study of FENGs by FEM calculation. (a) Schematic model of a section of FENG (80 μm $\times$ 300 μm). Simulation results of (b) electric potential distribution and (c) electric field distribution of the model without external pressure. Red arrows represent electric field vectors. Simulation results of (d) electric potential distribution and (e) electric field distribution of the model under 1 MPa pressure applied to the top surface.

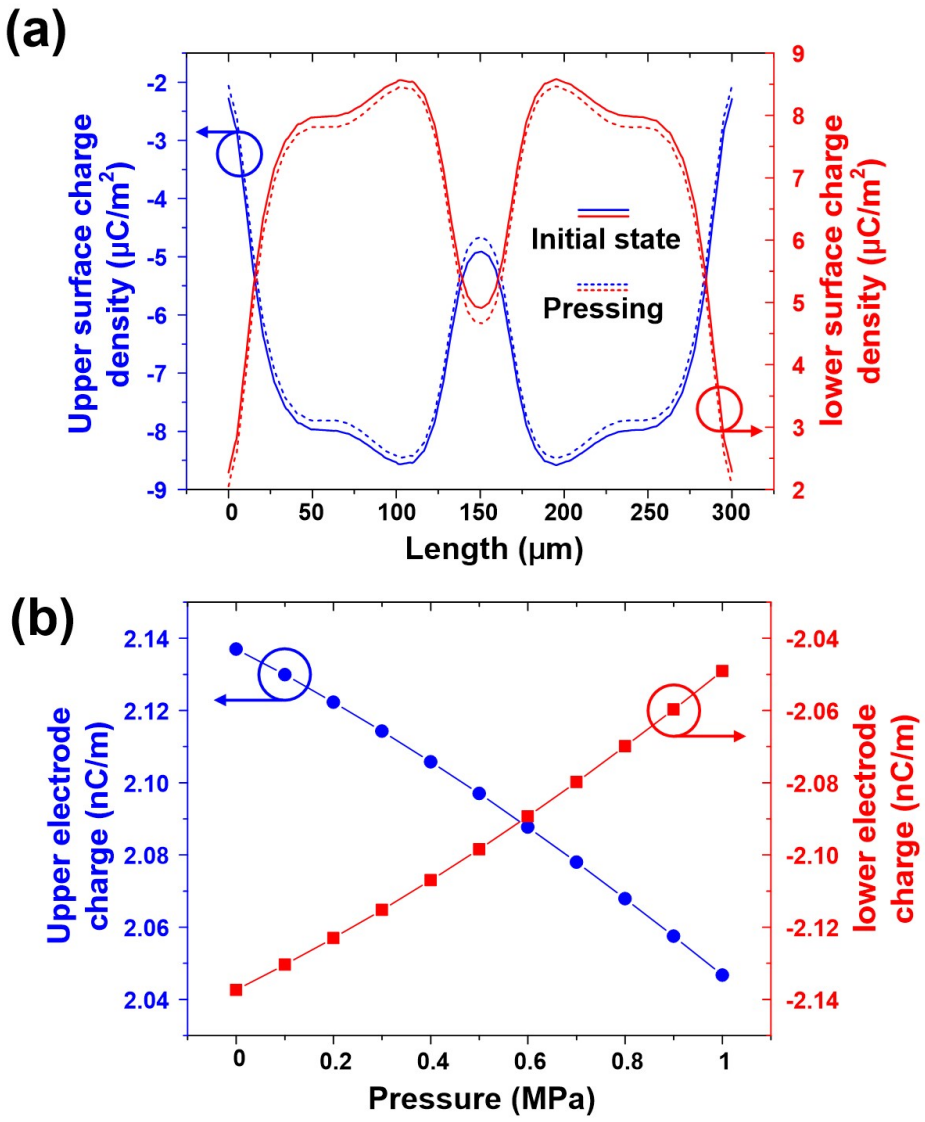

Figure 4.8 Charge variation of FENG. (a) Charge density distribution of the upper and lower surfaces before and after external pressure is applied. (b) Relationship between total accumulated charge at the upper and lower electrodes with applied pressure.

and positive charge on the lower electrode flow to ground simultaneously. When both electrodes are left floating, the accumulation of different charge between electrodes produces a difference in potential. By applying gradually increasing pressure on the upper surface of the model and integrating the surface charge density of upper and lower electrodes, the relationship between the total charges accumulating on both electrodes and the vertical pressure can be obtained as shown in Figure 4.8 (b). It can be seen that the accumulated charge on both

electrodes decreases proportionally with applied pressure. This "macroscopic" behavior of FENG resembles that of traditional piezoelectric materials.

4.4 Performance of FENG

4.4.1 Electrical Output of FENG

To investigate the performance of the FENG, V_{oc} and I_{sc} generated during periodical external pressure and release are measured. The pressure is provided by a stepper motor with 1.9 Nm holding torque via a linear motion stage (Figure 4.9 (a) and (b)). The pressing stage is mounted on an optical table for vibration isolation and with good electrical grounding.

Figure 4.10 (a) and (b) show the measurement results of the FENG with actual force contact area of 15 mm $\times$ 15 mm. A low noise nanovoltmeter and a low noise picoammeter were used to measured the V_{oc} and I_{sc}, respectively. It can be seen that the device exhibits typical piezoelectric-like behavior; i.e. when the FENG is pressed by the linear stage, V_{oc} and I_{sc} increase dramatically, and when the external pressure is released both signals experience very similar change, but with opposite sign. The measured peaks for V_{oc} and I_{sc} are $\sim$ 1 V and $\sim$ 0.1 μA, respectively. The switching polarity test [45] was carried out to confirm that the measured output signals are generated by the FENG rather than artifacts caused by the measurement instruments themselves.

4.4.2 Geometric Influence on FENG

The influence of the geometric form of FENG on the output electric signals is investigated herein. In order to increase the mechanical-electrical transformation efficiency of FENG, we folded the fabricated device along an axis of symmetry (Figure 4.11). When the film is folded once, the magnitudes of both V_{oc} and I_{sc} are doubled, which is tantamount to doubling the piezoelectric coefficient d_{33} of the unfolded state. When the FENG is folded three times, the

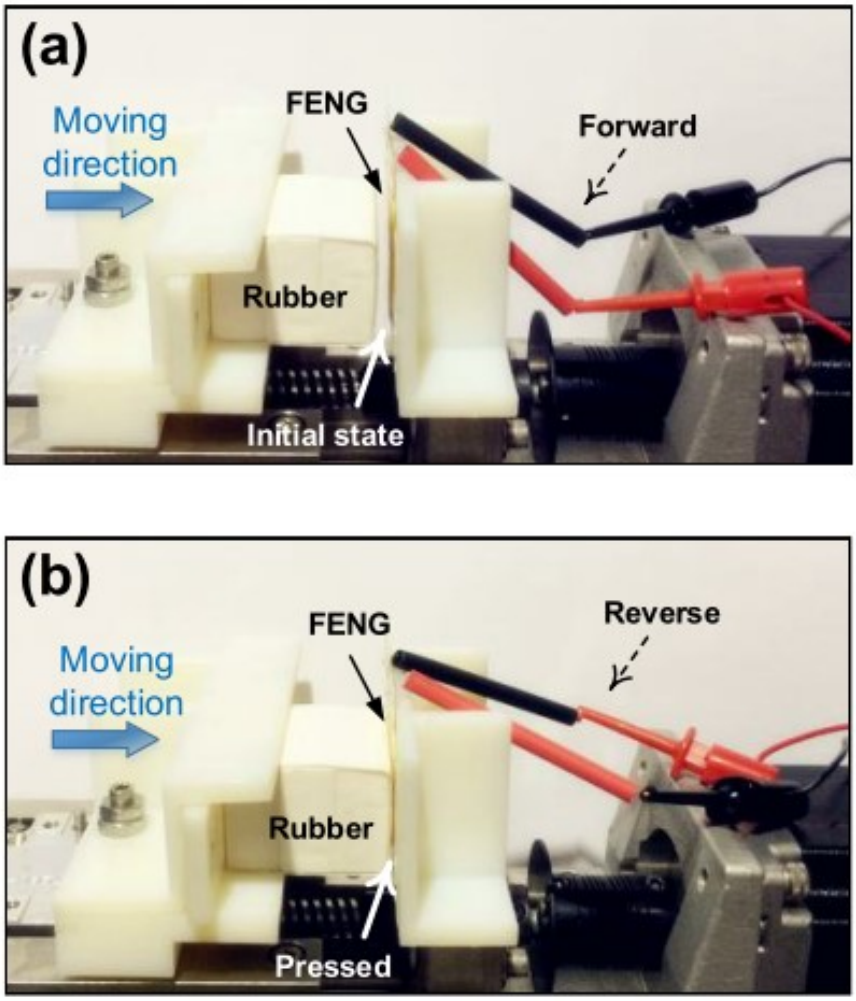

Figure 4.9 Photographs of mechanical loading test of FENG at (a) initial state while the electrodes are connected forward, and (b) pressed state while the electrodes are connected reverse. The FENG is fixed, and a step motor applies a pressure perpendicular to the FENG. The pressure applied to the FENG is real-time controlled. This set-up is also used to perform the pressure-dependent and frequency-dependent experiments discussed in this work.

measured electric signals are about 8 times as high as that of the unfolded state, suggesting that the output magnitude of V_{oc} and I_{sc} of FENG follows a 2^n relationship, where "n" represents the number of folds along an axis of symmetry. This suggests that the generated charge on the surface of PPFE is proportional to the pressured area, which increases by 2^n during the folding process. Hence, the mechanical-electric transformation efficiency of the FENG can be significantly enhanced by simple folding.

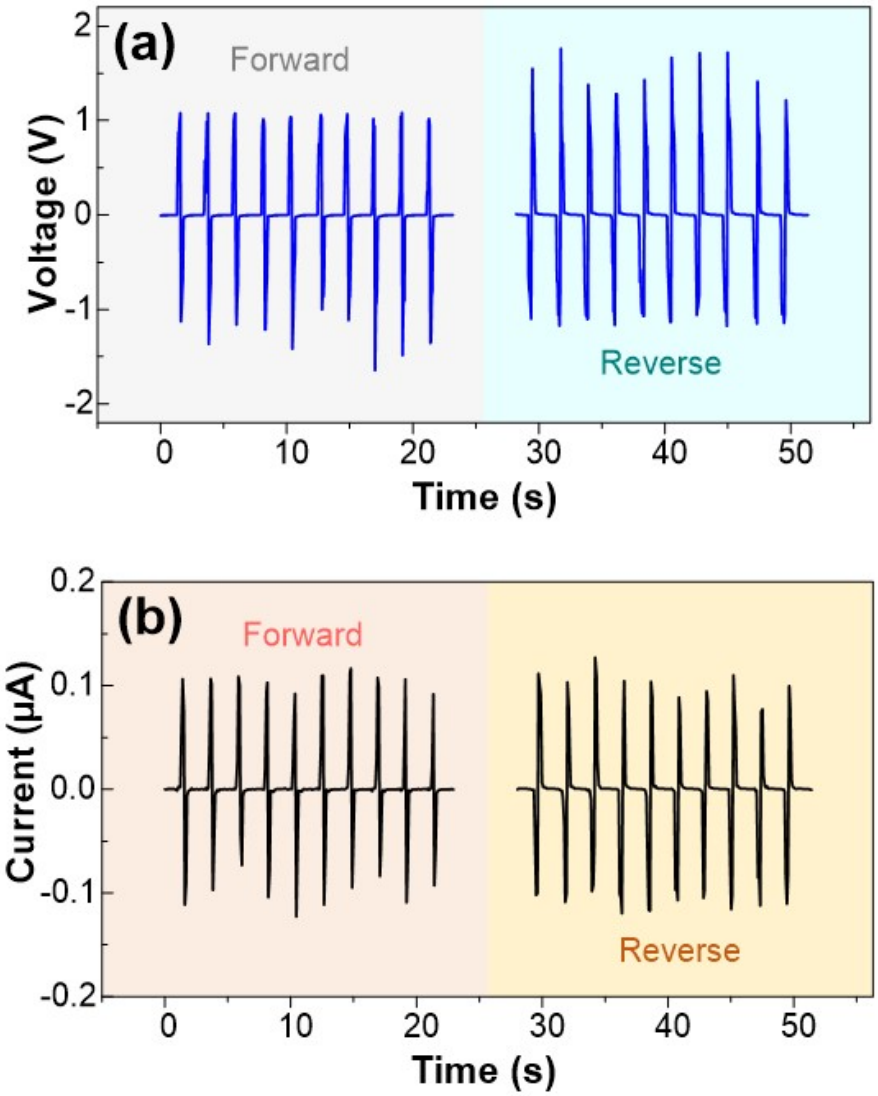

Figure 4.10 Experimental results of (a) V_{oc} and (b) I_{sc} of the FENG. Different sign in output for "pressing-releasing" sequence is observed when the electrical connections to the FENG are reversed.

4.4.3 FENG with Large-area

Use of a simple and low-cost bar-coating techniques (Figure 4.12 (a)) to form electrodes at both surfaces of a PPFE film, FENG with adjustable performance, overcoming the size limitation of the FENG caused by chamber growth and complicated transfer process [141] is able to be fabricated. Two layers of electrically conductive paint (Bare Conductive Inc.) were coated onto the PPFE film by using 3/8" × 16" wire wound lab rod with wet film

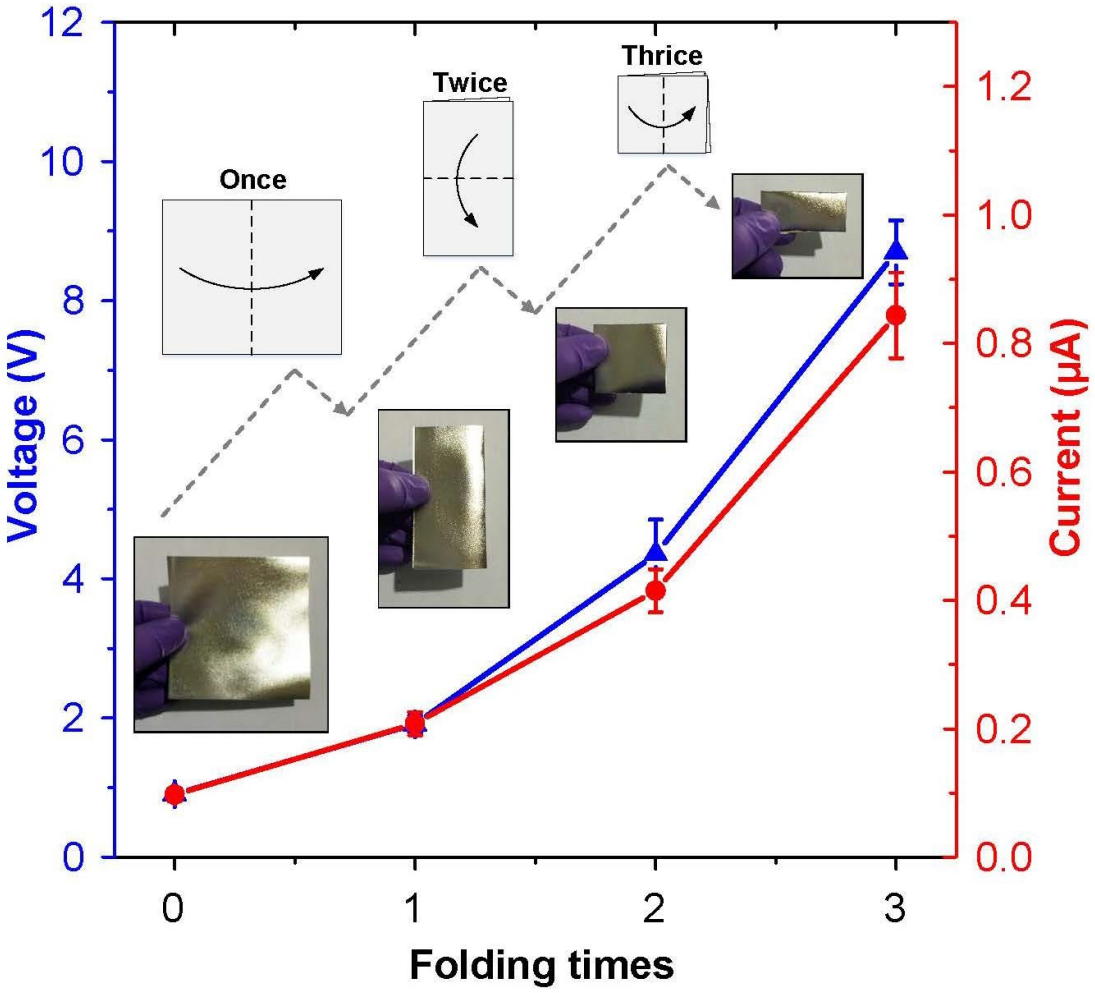

Figure 4.11 Performance of FENG with folding. Output voltage and current signals are amplified with each folding action along an axis of symmetry. The performance follows a 2^n behavior, where "n" is the number of folds.

thickness of 25.6 μm. A large-area FENG with dimensions of 180 mm $\times$ 180 mm was fabricated (Figure 4.12 (b)).

4.4.4 Stacked Multi-layers FENG

It is also possible to increase the output of the FENG by stacking single layers of PPFE separated by a conductive layer, to form a multi-layer structure where the giant dipoles in the adjacent film have opposite orientation. The surface of each single film having the same polarity are electrically connected in parallel to form a multi-layer device (Figure 4.13 (a)

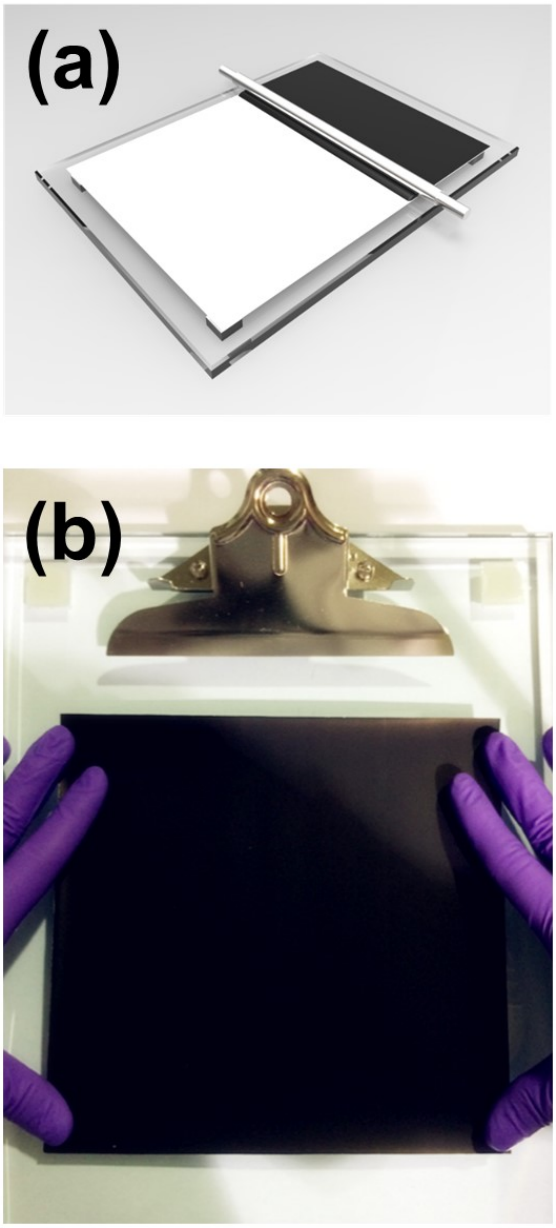

Figure 4.12 (a) Convenient bar-coating process for fabricating electrodes over large-area PPFEs. (b) Large-area FENG fabricated with simple bar-coating technique.

and (b)). It is noted that the increase in mechanical-electrical transformation efficiency by stacking single layers of PPFE follows the same rationale of the symmetric folding process – regardless of how you fold the film, the surfaces with the same polarity are always in electric contact. This folding characteristic of the FENG not only demonstrates a practical, flexible, and easy way to improve its performance, but also confirms the linear superposition behavior

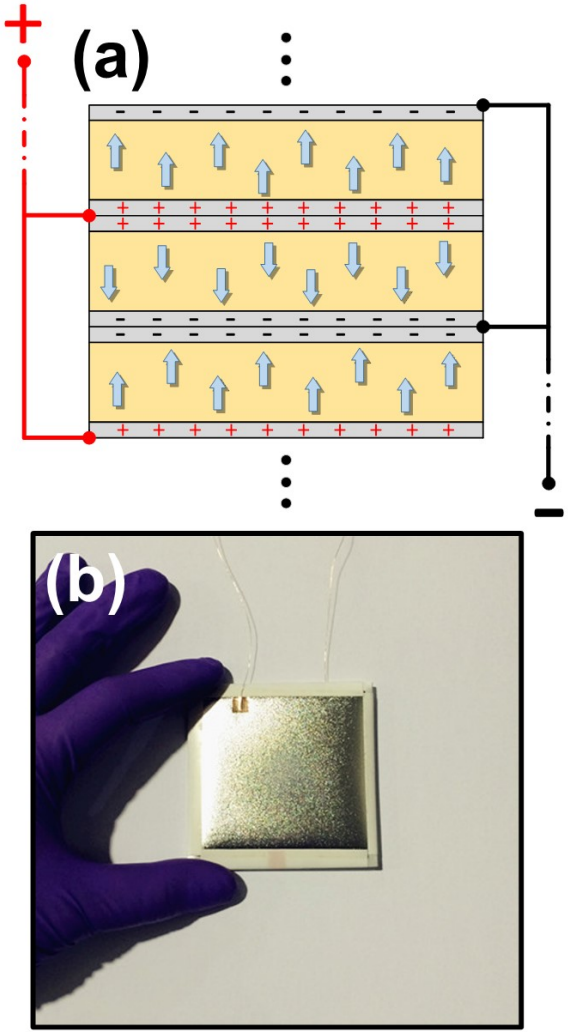

Figure 4.13 (a) Schematic illustration and (b) photograph of stacked FENG (∼40 mm^2) to increase magnitude of the generated electric signals. Common electrical contacts are made on alternating metal layers.

[154] of FENG; which also validates the "macroscopic" piezoelectric behavior of the material.

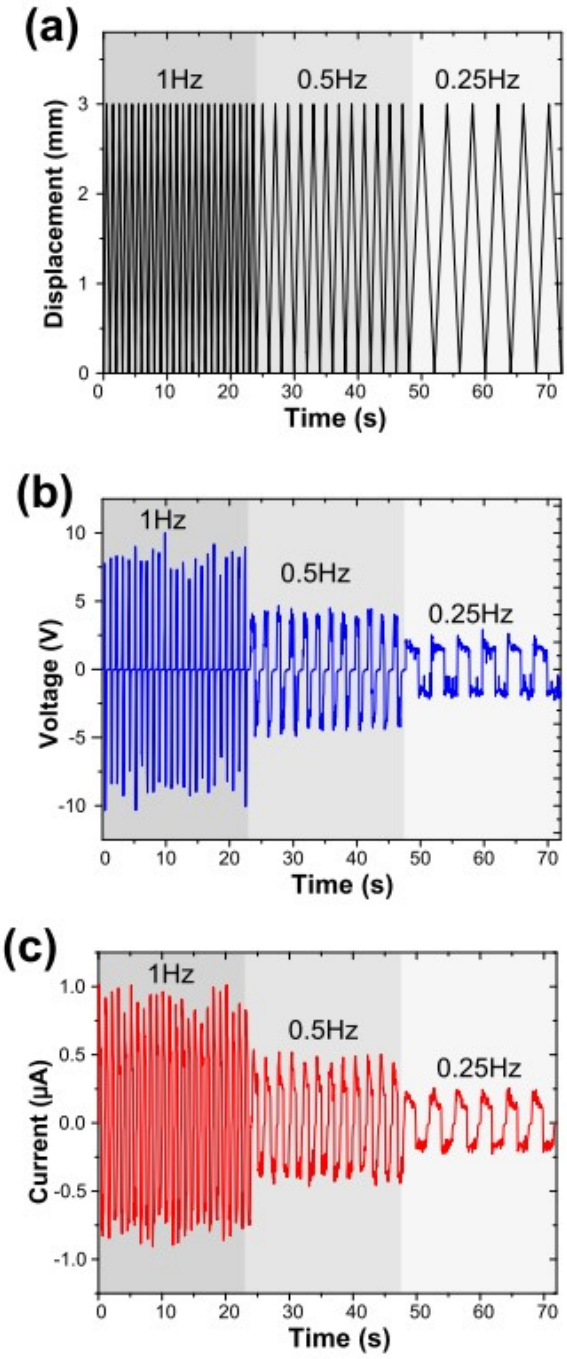

Figure 4.14 Time response of FENG. (a) Displacement of linear stage controlling the pressure on a FENG as a function of time. Three different displacement frequencies (1, 0.5, and 0.25 Hz) with same magnitude (3 mm) were used. (b), (c) Corresponding V_{oc} and I_{sc} generated from FENG. Magnitude of voltage and current peaks decrease with frequency.

4.5 Dynamic Response of FENG

4.5.1 Time Response of FENG

Further characterization of the FENG was made by measuring the FENG's response for an oscillatory input as a function of frequency and magnitude. Figure 4.14 (a)-(c) shows the stage moving displacement, V_{oc}, and I_{sc} as a function of time of a FENG under pressing with frequencies of 1 Hz, 0.5 Hz, and 0.25 Hz. The tested FENG is periodically pressed by the real-time controlled motorized stage, which controlled the lateral displacement of a rubber cuboid parallel to the FENG surface (see Figure 4.10). It can be seen that increasing the frequency with the same load amplitude increases both V_{oc} and I_{sc} generated by FENG, similar to the phenomenon observed from piezoelectric based nanogenerators [26].

4.5.2 Amplitude Response of FENG

Figure 4.15 (a) and (b) show the V_{oc} and I_{sc}, respectively, as a function of time of a FENG under different stage displacement (3 mm, 1.5 mm, and 0.75 mm), which corresponds to different pressures applied on the device. It can be seen that the amplitude of both V_{oc} and I_{sc} are proportional to the stage moving displacement or the applied pressure.

4.5.3 Electrical Energy Storage

To demonstrate the energy harvesting capability of the device, a Schottky bridge rectifier (DB102, RECTRON Inc.) is connected between the FENG and a low leak capacitor (22 μF, 50 V, Nichicon). The nanovoltmenter is used to measure the voltage across the capacitor. In this configuration, the voltage generated by the FENG (during pressing and releasing) is used to charge the capacitor. It can be seen that the stored voltage increases continuously with each cycle of loading and releasing process. As the process continues, the stored voltage keep increasing to a maximum magnitude determined by the range of nanovoltmeter. According to

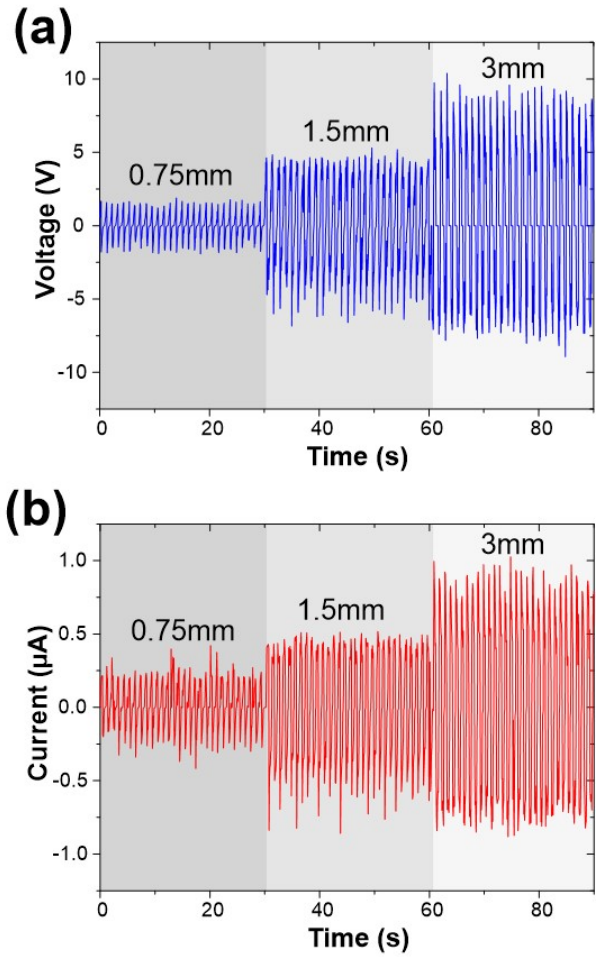

Figure 4.15 (a) V_{oc} and (b) I_{sc} generated from FENG for linear stage input of different displacements (i.e. different pressure magnitudes input) and same frequency (1 Hz).

the charging curve of Figure 4.16, it can be anticipated that the stored voltage has the trend to continue increasing for even higher values (the maximum stored energy will be ultimately determined by the capacitor). This demonstrates that the FENG could be integrated into autonomous electronic systems where harvested energy is used, for example, to charge a solid-state battery.

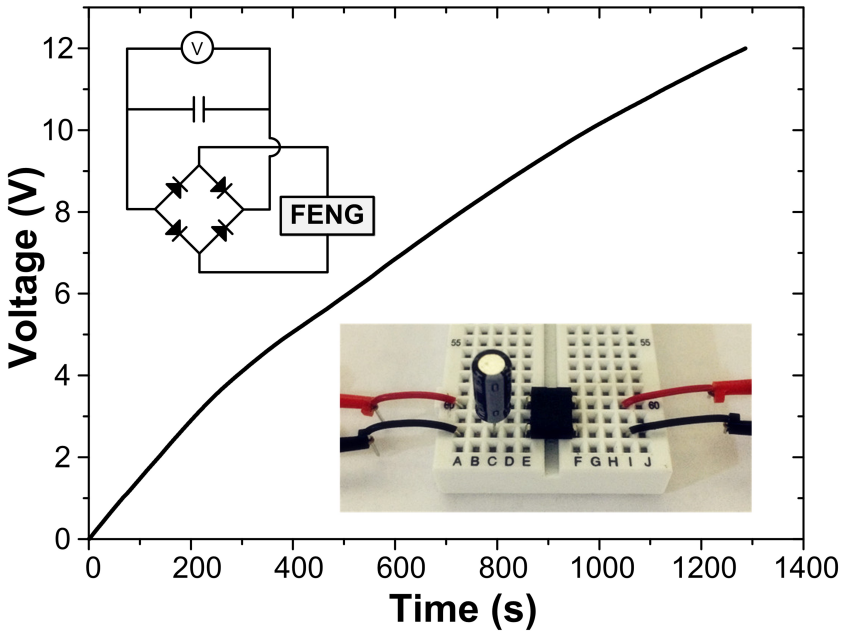

Figure 4.16 Plot of voltage stored in a 22 μF capacitor for a FENG under a periodic input (3 mm, 1 Hz) as a function of time. The maximum voltage that can be read by the nanovoltmeter was 12 V. Inserts in the plot show the electrical schematic of the circuit used and a photograph of the implemented circuit.

4.6 Several Demonstrations of FENG

4.6.1 LED Illumination

To demonstrate that the harvested energy can be utilized as an effective power source, a FENG consisting of a stack of 7 PPFE film layers is used to provide energy for commercial LEDs. Figure 4.17 (a) shows the device is connected with a Schottky bridge rectification circuit and 20 LEDs (green and blue, 3.0 - 3.4V) connected in series. Pressing the device with the hand, V_{oc} and I_{sc} can reach higher than $\sim$ 50 V and $\sim$ 5 μA, respectively. Figure 4.17 (b) shows the LEDs before and during hand's pressing on the FENG. The LEDs were simultaneously lit upon pressing. The results show that the mechanical energy harvesting ability of the FENG is capable of converting human motion to electrical energy, demonstrating the potential of the device to power wearable (or implantable) electronic devices.

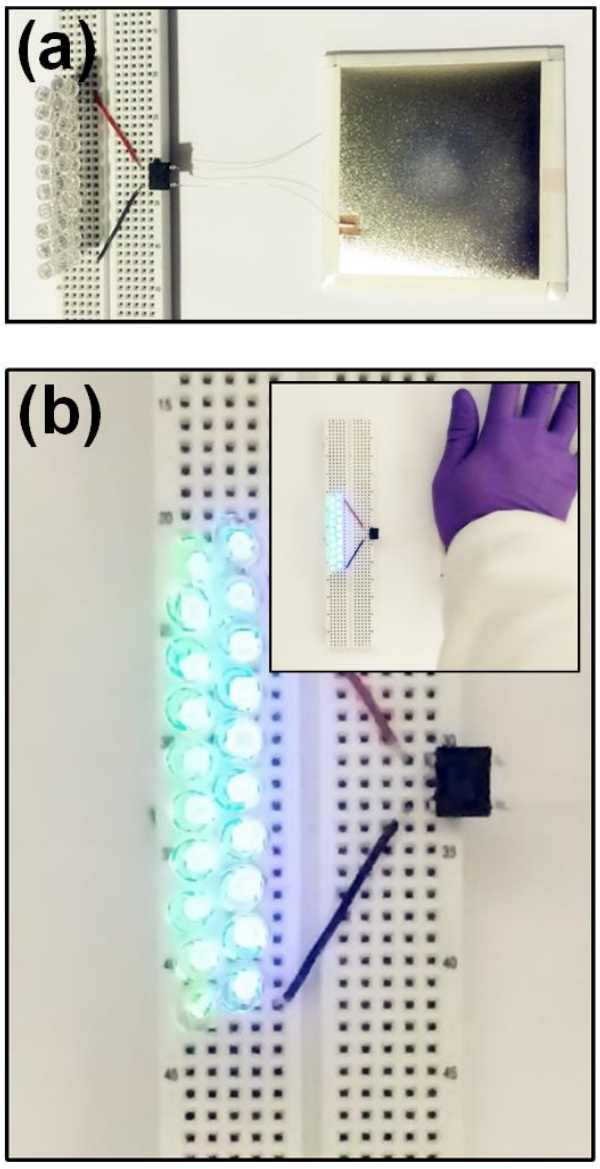

Figure 4.17 (a) A FENG consisting of a stack of 7 PPFE film layers connected to 20 green and blue commerical LEDs through a rectifier. (b) LEDs connected are lit by FENG just by one time hand-press.

4.6.2 Self-powered Touch LCD

Another promising application of the developed FENG is self-powered touchscreens, which could be used in smart phones, tablets, E-ink papers, or touch-screen panels. As a step towards such implementations, we demonstrated the integration of the device with a 4-bit LCD screen, as illustrated in Figure 4.18. When gently tap the self-powered LCD screen by

Figure 4.18 A self-powered LCD touch screen which is able to scavenge energy from finger touch. Word "PLAY" is displayed on the screen by touching a small area of the corners by the user.

the user, the word "PLAY" is displayed on the screen without rectifiers or charging circuits. The biomechanical harvested energy (converted to electrical energy) allows for the letters to be displayed. The developed self-powered FENG-based display could increase the energy efficiency of smart phones and wearable devices by scavenging energy from the users' touch during regular operation – thus reducing the frequency of required battery charges from external energy sources.

4.6.3 Flexible/Foldable Self-powered Keyboard

Another demonstration of the applicability of the FENG is on what can be considered as one of the most common, reliable, accessible and effective tools used for human-machine interfacing and information exchange: a keyboard [40]. We fabricated a flexible, foldable, and self-powered keyboard which converts the mechanical stimuli applied to the keyboard upon key-punching into an electric signal that is used to display the pressed letter on a computer monitor. The structural design and photograph of the thin film keyboard are

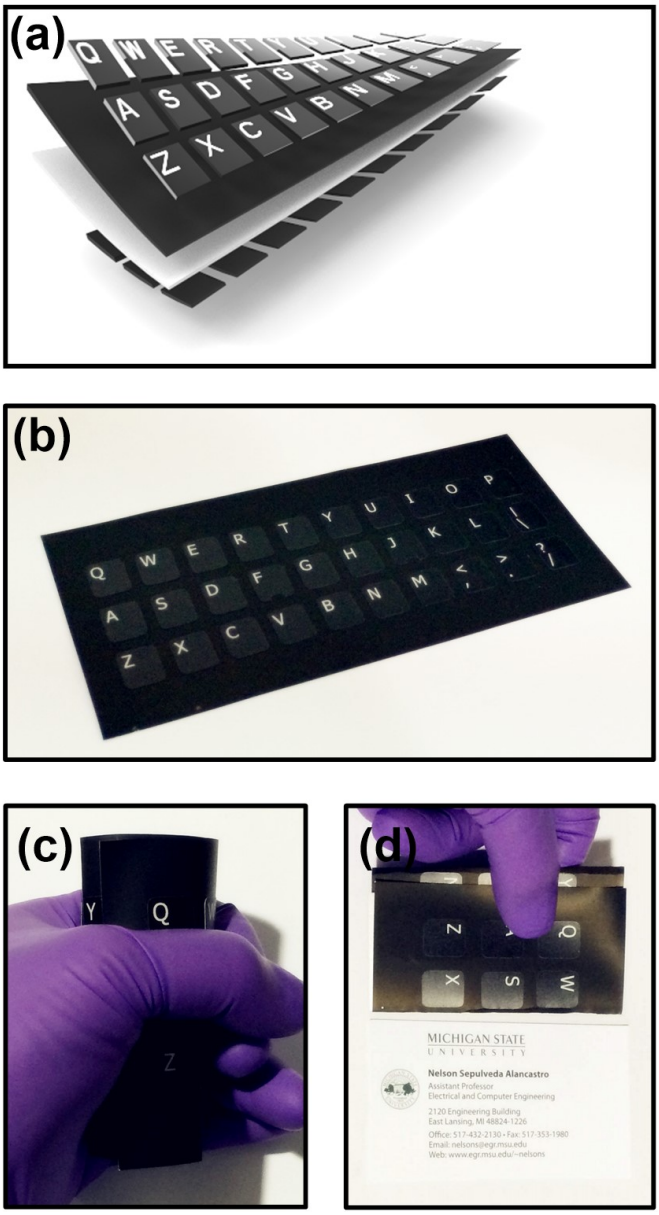

Figure 4.19 Exploded view (a) and photograph (b) of developed FENG-based flexible/foldable self-powered keyboard. Rollability and foldability of the developed keyboard is shown by (c) rolling it with hand or (d) folding it to the size of a business card.

shown in Figure 4.19 (a) and (b), respectively. By using bar-coating technique (like the one shown in Figure 4.12), the top and bottom surface of a PPFE film is uniformly coated by electrically conductive paint without mask and with patterned shadow mask, respectively. The real-time keystroke tracing and recording. As the user types the word "SPARTANS", the output is displayed (in real-time) on a computer monitor (Figure 4.20). The developed

FENG-based keyboard can also be rolled (Figure 4.19 (a)) or folded (Figure 4.19 (b)) while keeping its functionality. This could offer a way to change today's large volume battery-operated keyboards into power-less portable devices that can be folded to the size of a business card.

Figure 4.20 Real-time keystroke tracing and recording. As the user types the word "SPARTANS", the output is displayed on a computer monitor.

4.7 Summary

In summary, a new type of energy harvesting method that takes advantage of ferroelectric phenomenon is introduced. Based on PPFE, we demonstrated the fabrication of lightweight, flexible, foldable, and biocompatible thin film FENG which is able to be power source for commercial electronics such as colorful LEDs. By adapting bar-coating technique, a large-area FENGs is fabricated. One of the compelling characteristics of FENG is that both of the V_{oc} and I_{sc} would be doubled with each folding of the FENG along an axis of symmetry, allowing the FENG to reach very high voltage if needed. Niche applications of FENGs are further demonstrated including a self-powered touching screen LCD which is capable of scavenging energy from users' touch, leading to vast prospect in today's abundant touch screen devices; and the flexible/foldable, self-powered keyboard which can be folded as business

card size. Advantages such as lightweight, flexible, foldable, biocompatible, scalable, low cost and robustness could make FENG a promising and alternative method in the field of mechanical energy harvesting for various of autonomous electronics.

CHAPTER 5

FENG-BASED DUAL-FUNCTIONAL THIN PATCH LOUDSPEAKER AND MICROPHONE FOR FLEXIBLE ELECTRONICS

The interest in ultrathin, flexible paper-like personal electronics is growing at an accelerated pace, and the pursuit of multifunctionality and wearability has become a major technological trend [155, 156, 157, 158, 159, 160, 161, 162, 163, 164, 165, 166]. The continuous, aggressive, and multidisciplinary research efforts from multiple groups has created a sustained stream of innovation that has been constantly evolving and improving; making a large number of innovative products, such as wearable computer screens, electronic newspapers, flexible light-emitting diodes (LEDs), artificial skin, and smart gloves within the foreseeable future [167, 168, 169, 170, 171, 172, 173, 174, 175]. User-device interaction is a very important aspect of wearable technologies. It is understandable that from the five recognized human senses (i.e. vision, audition, gustation, olfaction, and somatosensation [176]), most of the current advances are focused on the use of sight and touch. However, the optimal wearable system designs should consider all human senses, since this will enable all the possible user-device interactions and allow for the use of the most appropriate one, depending on the application. Besides vision and touch, acoustic interaction (i.e. hearing and speaking) also has good potential of becoming an essential and convenient bridge between human and flexible personal electronics in the coming years. In a way, we are experiencing this already through the voice-activated gadgets, speech-to-text converters, and audio recognition systems.

The prevailing loudspeakers used today consist at least of a diaphragm, a voice coil attached to the apex of the diaphragm, a permanent magnet fixed to the loudspeaker's frame via a flexible suspension, and an enclosure [177]. When an audio current waveform is applied to the voice coil, an audio frequency movement of the diaphragm is produced

due to the magnetic interaction between the voice coil and the magnet, thereby reproducing the sound pressure waves [178]. Recently, a thermoacoustic superaligned carbon nanotube (CNT) loudspeaker was demonstrated, which uses thermal expansion and contraction of the medium to generate sound waves [177, 179, 180, 181]. A microphone is a reversely operating device, in which sound waves are converted to electrical signals, functions and it can be considered as the "ears" of flexible personal devices. Recently, the use of a thin, rollable, triboelectric nanogenerator (TENG) was demonstrated to harvest sound waves [182]. The further advance of human-computer interaction (HCI) in wearable electronics would benefit from thin film, flexible, light-weight and robust devices that can serve as both: loudspeaker and microphone.

In this chapter, a dual-functional and self-powered thin film flexible acoustic transducer, which operates as both loudspeaker and microphone is reported. Based on ferroelectret nanogenerator (FENG) reported recently [183], the device has the ability to produce power as well. By means of microplasma discharging, the artificial voids inside the foam-structured FENG forms numerous giant dipole which enable the FENG with outstanding electromechanical transformation efficiency. We describe the mechanisms for direct and reverse interaction effects (i.e. using mechanical energy to produce electrical energy, and using electrical energy to produce mechanical energy), which are the cornerstones of the present FENG-based loudspeaker/microphone device. Characterization of the performance of the FENG-based loudspeaker is done by sound pressure level (SPL) directivity measurements for three developed configurations: free-standing FENG, FENG attached to a soft substrate, and rolled FENG in cylindrical shape. Moreover, the amplitude-frequency response (10–20,000 Hz) for the present FENG-based loudspeaker is characterized as a function of functional area, number of layers, and for cases with or without substrate. To demonstrate the applicability and functionality of the device, I fabricated a FENG-based music-playing flag which can operate under regular wind conditions. Due to the electro-mechanical coupling of the device, the operation of the FENG-based loudspeaker can be reversed, to result in a FENG-based

microphone that converts acoustic vibration (sound) into an electrical signal. The FENG-based microphone is highly sensitive to a broad range of frequency. This is shown by the other two demonstrations presented in this work; which include the recording of a symphony by a piece of paper-like FENG-based microphone with high fidelity, and the security of a personal computer by the voiceprint identity recognition through a FENG-based device that can easily be integrated secretly within a computer or personal device for added subtlety.

5.1 Structural Configuration of Flexible FENG-based Acoustic Transducers

The functional material of the FENG-based acoustic transducers is prepared by starting with polypropylene film containing tiny foreign silicates particles (0.1 μm to 10 μm), as shown in Figure 5.1. Polypropylene (PP) is a type of commodity plastic with the merits of low density, high flexibility and good resistance to fatigue [184, 185]. Once the PP film experiences stretching in two perpendicular directions, the inorganic particles serve as stress concentrators or micocracks, allowing the film to be filled with lens-shaped voids with diameters ranging from 1 μm to 100 μm. During this process, high pressure (e.g. 5 MPa) nitrogen or carbon dioxide gas is diffused into the PP film, so that the internal pressure within the voids becomes equal to the external pressure. Next, the external gas pressure is suddenly released, resulting in dramatically swell of those voids in PP film. For the purpose of stabilizing and stiffening the swelling voids at room temperature, thermal treatment (usually higher than 100°C) is carried out to increase the crystallinity of the polymer matrix [186, 187, 188]. Subsequently, by applying a large electric field to the treated film, Paschen-breakdown occurs inside the voids. The current within the air gap transfers a sheet charge density across the air gap. During microplasma discharge, charges separated by the ionization of the gas transportation under the charging field, and light flashes can be observed with the naked eye, forming a "microstorm".

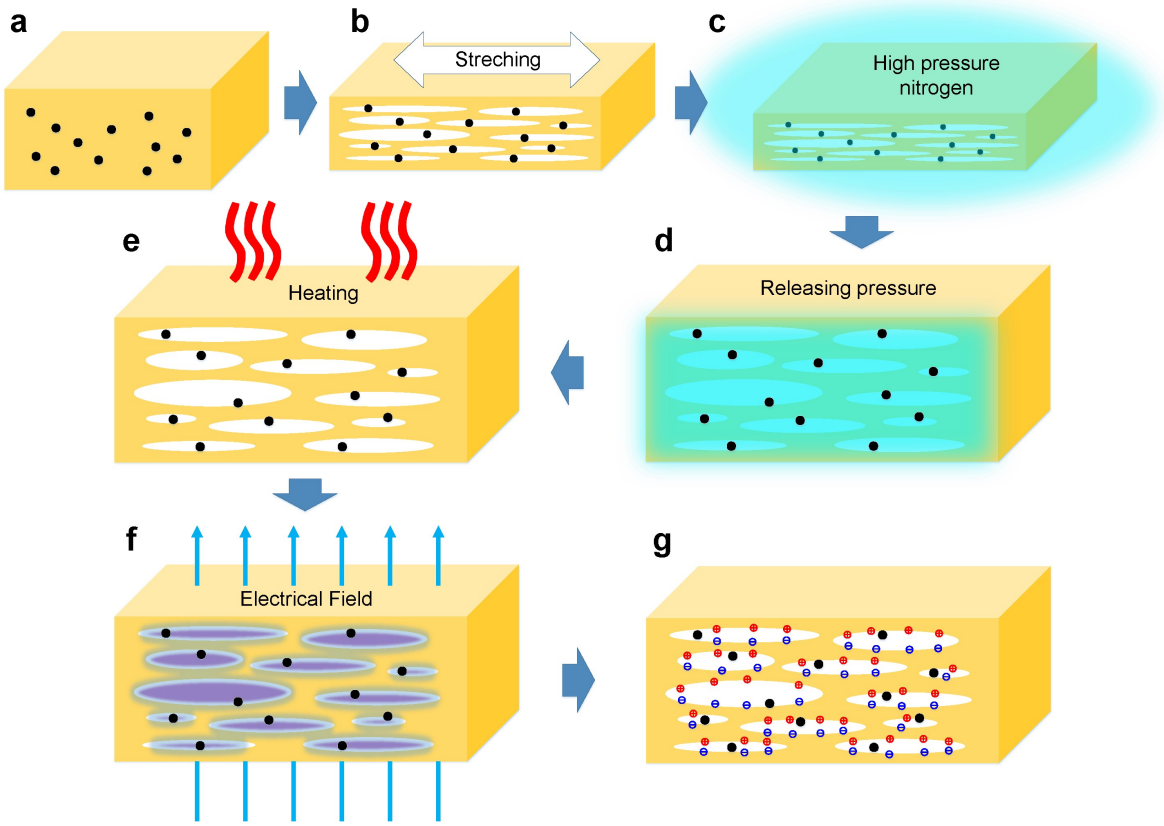

Figure 5.1 Schematic illustration of the fabrication process of polypropylene ferroelectric film. (a) Polypropylene film is filled with silicate particles. (b) Film is under stretching. (c) Film is in high pressure (5 MPa) nitrogen environment, and nitrogen eventually diffuse into the internal voids. (d) Suddenly release the high pressure of nitrogen, results in the swell of the internal voids. (e) Film experience 100 °C heat treatment. (f) Microplasma discharging inside the voids by applying high electric field to ionize the gas molecules. (g) Positive charge and negative charge separated and located at the surfaces of the voids after discharge, forming the giant dipoles.

The schematic structure of the flexible FENG-based acoustic transducer is shown in Figure 5.2 (a). The total thickness of the device is less than 100 μm. After microplasma discharging, two thin layers of silver (500 nm) were deposited on both top and bottom side of PP film (80 μm) by sputtering. Scanning electron microscopy (SEM) images of the cross-section of PP foam are shown in Figure 5.2 (b). Herein, backscattered electrons are used for revealing good contrast and clear definition of the structure. As the production of backscattered electrons is strongly dependent on the average atomic number of the sample,

silicate particles appeared to be much brighter than their surrounding structure. Figure 5.2 (c) shows the optical images of FENG-based acoustic device rolled along the axial of a glass tube. The highly flexible fabricated device consists of a stacked metal-insulator-metal (MIM) thin film structure without moving parts or microfabrication features or suspended structures, which makes the process easily scalable to large-scale fabrication.

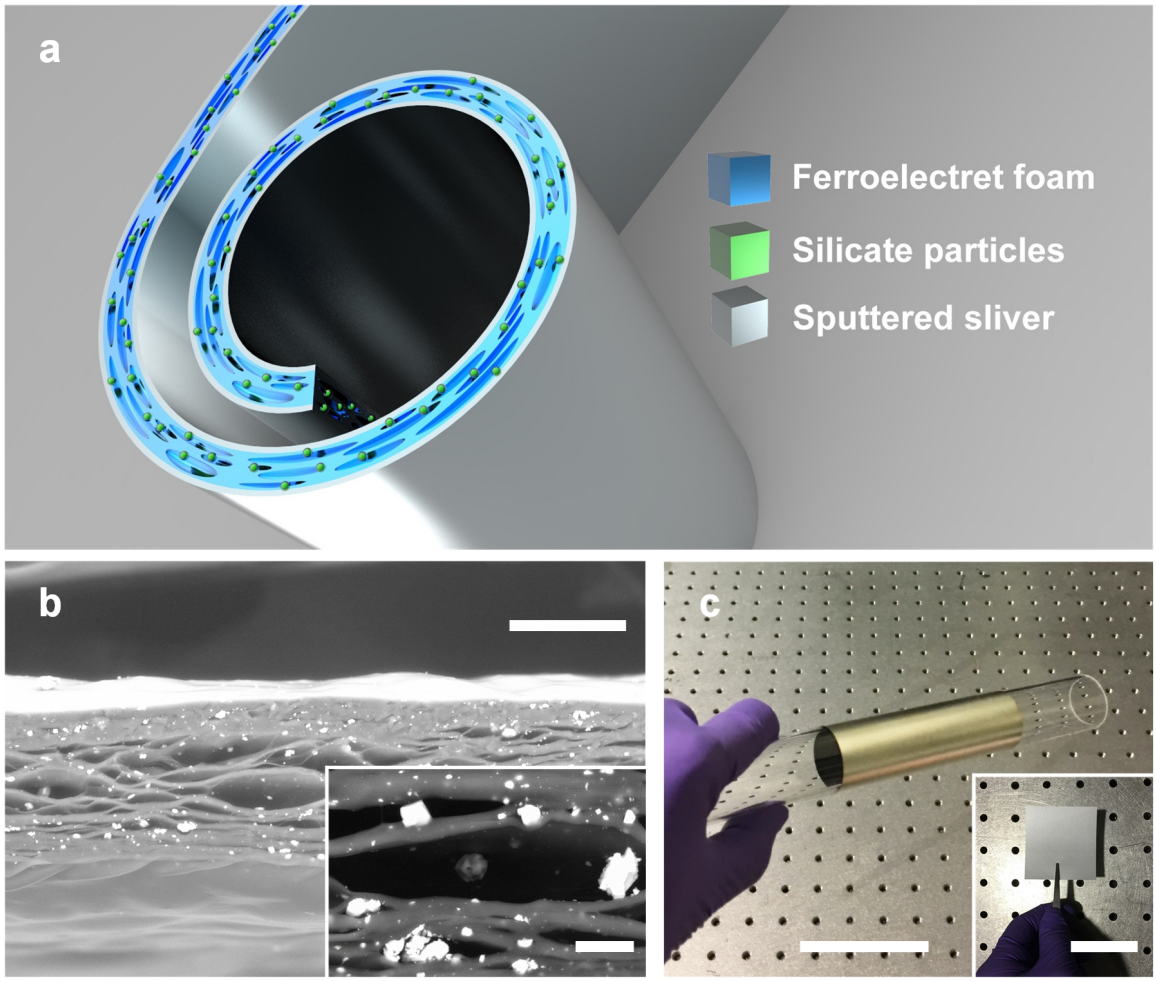

Figure 5.2 Schematic and experimental structure of FENG-based acoustic device. (a) Schematic structure of a large area flexible FENG-based acoustic device. (b) Cross-sectional backscattered SEM image of the PP foam (scale bar, 20 μm). The inset shows the expanded view (scale bar, 10 μm), where the silicate particles can more easily be identified as the brighter regions. (c) Optical images of FENG-based acoustic device along the axial of a glass tube (scale bar, 5 cm). The inset shows the top-view of PP foam inset (scale bar, 5 cm).

5.2 Working Mechanisms of Direct Effect and Reverse Effect of FENG

By means of microplasma discharges in the fabricated foam structure in PP film, opposite charges accumulate on the upper and lower surfaces of the artificial voids, which in turn form numerous highly oriented giant dipoles. Once two layers of silver are sputtered on both outer surfaces of PP film, the giant dipoles in the PP film induce charges of opposite polarity in each silver film. Unlike piezoelectric material which have spontaneous electric polarization, micro-discharging treatment turns the PP film from completely non-polar materials into artificial intelligent material which mimics both the microscopic molecular structure and macroscopic electromechanical behavior of the piezoelectric material. Furthermore, in comparison with traditional piezoelectric materials, FENG features with flexibility and internally charged cellular structures, which makes them highly efficient in charge storage and more sensitive to mechanical stress.

The direct electromechanical interaction effect of FENG is illustrated in Figure 5.3. When the FENG experiences compression or expansion in the thickness direction, the internal dipole moments simultaneously change in magnitude according to the applied pressure. Consequently, the change of dipole moments drive the compensation electrons from the electrode with negative charge to the electrode with positive charge, creating a potential between the two electrodes under open-circuit condition, or a flow of charges under closed-circuit condition.

On the reverse case, if extra charges are transferred to surface electrodes (or if there is a potential difference between them), the change of the charge density on the surface electrodes (or the electric field field across the thickness) reshape the giant dipoles inside the FENG, showing the reverse electromechanical interaction effect, as shown in Figure 5.4. Depending on the extra charge or magnitude of the applied voltage, numerous giant dipoles contract or expand at the same time, which results in a change in the thickness of FENG.

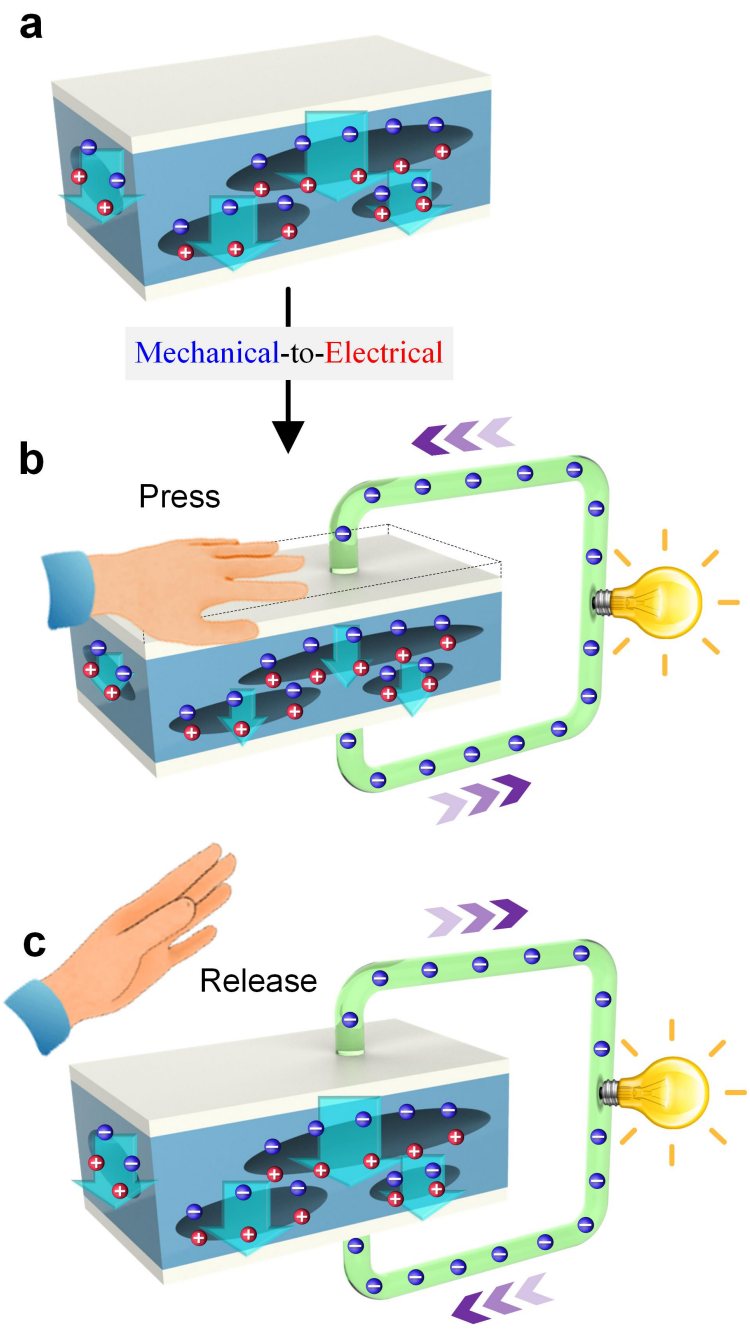

Figure 5.3 FENG's electrical-to-mechanical energy conversion mechanisms. (a) Charge distribution and giant dipoles of FENG after microplasma discharging, showing that the upper and lower surfaces of voids are oppositely charged. (b-c) Direct electromechanical interaction effect. (b) Pressed by human hand on the surface of FENG. (c) Pressure released and giant dipoles restore original sizes.

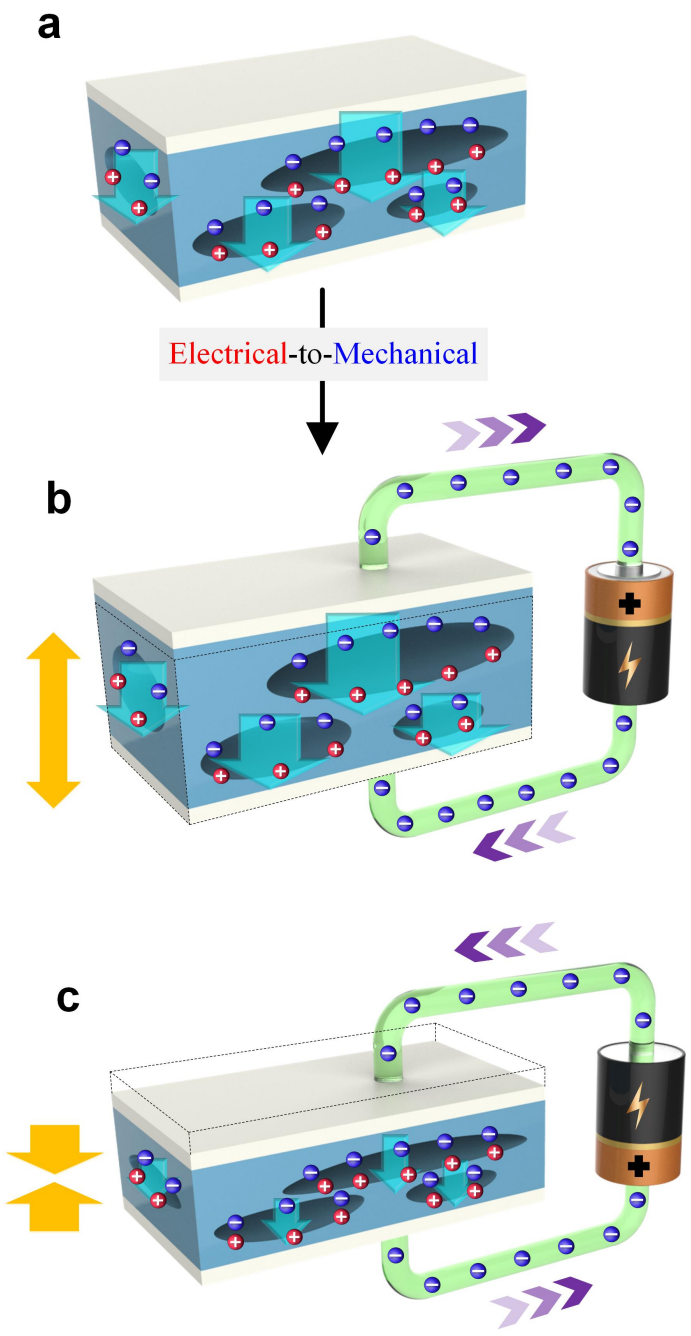

Figure 5.4 FENG's mechanical-to-electrical energy conversion mechanisms. (a) Charge distribution and giant dipoles of FENG after microplasma discharging, showing that the upper and lower surfaces of voids are oppositely charged. (b-c) Reverse electromechanical interaction effect. (b) Giant dipoles further expand as positive potential is applied. (c) Giant dipoles shrink as negative potential is applied.

If the added charge or electric field is varied as a function of time, the changes in thickness of the FENG will also occur as a function of time, producing vibrations of its surfaces. This electromechanical coupling endows the FENGs with the capability of efficiently converting energy between the electrical and mechanical domains. This bi-directional capacity of the FENG adds to the list of device attributes (e.g. simplicity, flexibility, softness, durability, lightweight, easy scaled-up structure), which not only broadens the device applicability from energy harvesting devices [183] to electro-acoustic flexible devices, but also establishes a new operating principle for flexible loudspeakers and microphones.

5.3 SPL Directivity of FENG-based Thin Film Loudspeaker

SPL directivity is a quantitative measure of the focusing of acoustic or sound energy. To investigate the frequency response change of FENG-based loudspeaker at off-axis angles, SPL directivity measurements were performed for three types of configurations: free-standing flat structure, flat structure with a transparent soft layer as the substrate, and cylindrical structure. Since the proposed paper-like FENG-based thin film loudspeaker is able to produce sound levels comparable to those produced by bulky commercial voice-coil loudspeakers, the acoustic performance can be directly tested by using the same measurement equipment for conventional acoustic products.

The measurement setup for the SPL directivity is shown in Figure 5.5. The configuration shown in the setup is the free-standing FENG-based loudspeaker, but the same setup was used for the other two configurations. A piece of circular free-standing FENG-based loudspeaker (diameter of 8 cm) is clamped in the center of a frame. A circular shape is chosen due to its central symmetry which aims at avoiding boundary effect during the film's movement. In the measurement, a prepolarized microphone system pointing to the center of the FENG-based loudspeaker was rotated continuously and smoothly around the device. During rotation, the corresponding angle between the microphone and a vector normal to

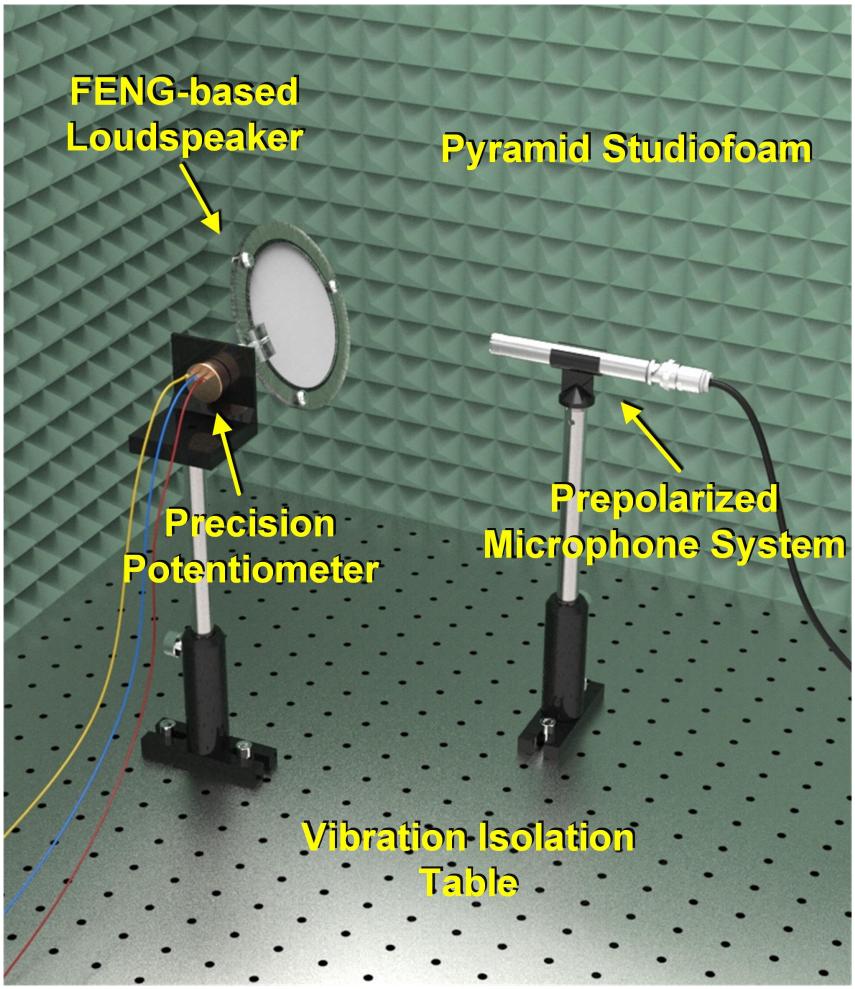

Figure 5.5 Experimental setup for free-standing FENG-based loudspeaker.

the device was recorded by precision potentiometer synchronously. In principle, keeping the device stationary while rotating the microphone will result in the same sound pattern measurement than keeping the microphone stationary, while rotating the device.

Figure 5.6 illustrates the equivalent SPL directivity measurement process, the hardware used, and their connections. The FENG-based loudspeaker was considered as a circular radiator, while the microphone measured SPL along a complete ring (i.e. 360 degrees) of uniform radius centered at the device, which is also the origin of the polar plot. SPL directivity measurements indicate how much sound is directed towards a specific area, compared to all the sound energy being generated by a source.

Polar plots of SPL directivity of circular free-standing FENG-based loudspeaker Figure

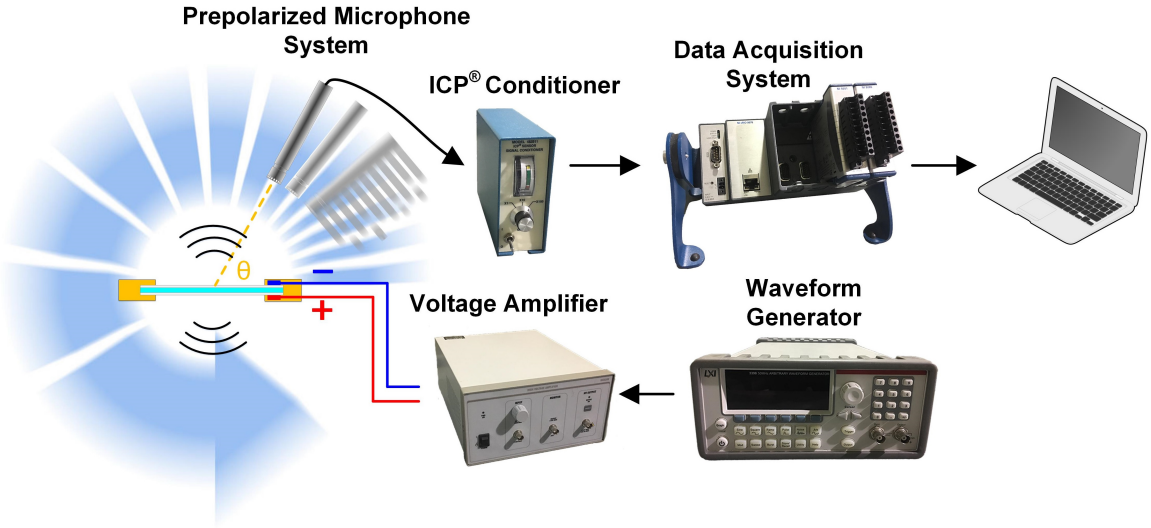

Figure 5.6 Lateral view illustration of measurement process with hardware connections. For the experiments, the FENG loudspeaker remained static, while the microphones was rotated.

5.7 (a) with amplitude of 300 V and frequencies of 500 Hz, 2 kHz and 10 kHz are shown in Figure 5.7 (b). It can be noticed that the directional pattern of flat paper-like FENG loudspeaker is symmetric along the horizontal line, which indicates it can produce identical sound pressure from both surfaces. In comparison with most directional loudspeaker in the market, radiating sound from not only the front-side, but also the back-side at same level could allow more sound to be directed to more listeners in practical applications. The SPL for the free-standing configuration is related to the relative position between the device and the microphone. Overall, a larger projected area results in more sound wave radiated into the microphone and a larger SPL. In addition, the SPL directivity under 500 Hz, 2 kHz, and 10 kHz shares similar directivity patterns except for their envelope sizes, which is due to the amplitude-frequency characteristics.

Figure 5.8 (a) and (b) show a circular FENG-based loudspeaker (diameter of 8 cm) firmly adhered to a soft acrylic layer and the SPL directivity, respectively. The acrylic layer blocks sound radiation produced from the attached device's surface, which increases the directivity of the FENG loudspeaker. For frequencies of 500 Hz, 2 kHz and 10 kHz,

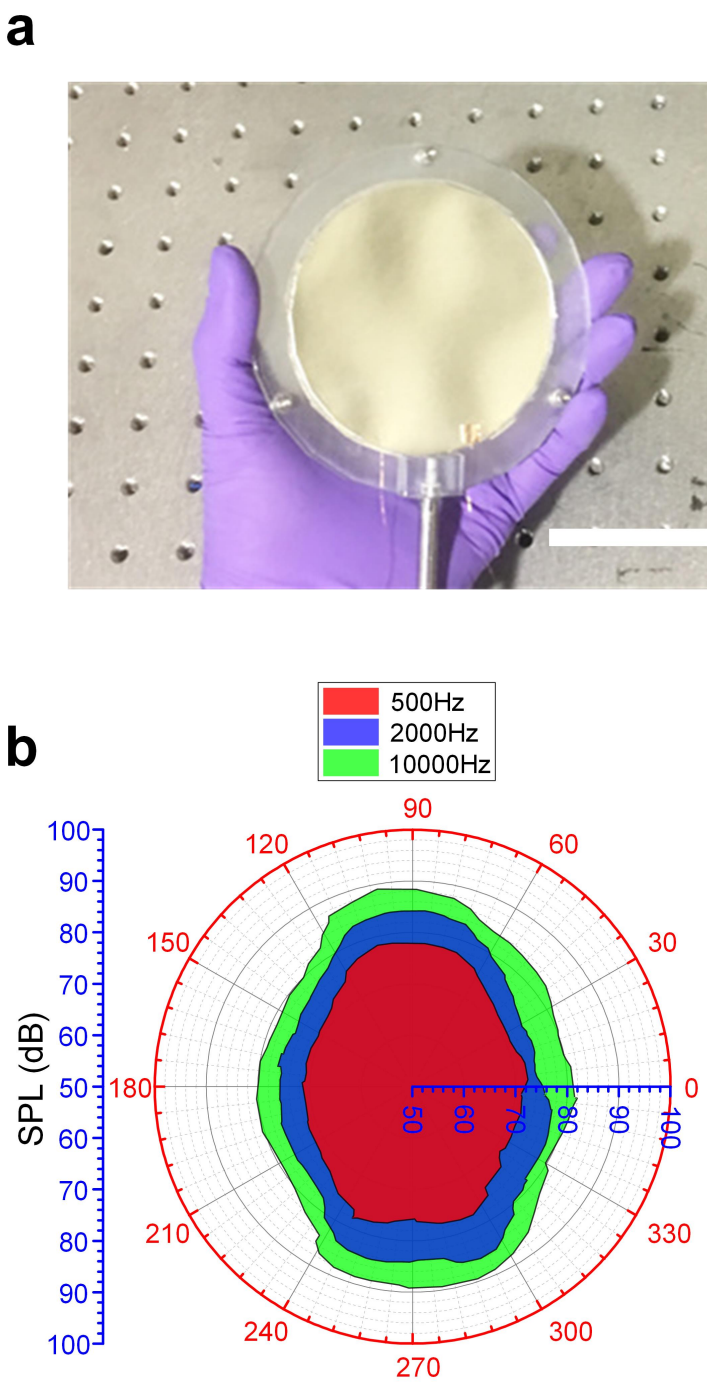

Figure 5.7 (a) Optical images and (b) SPL polar plots of circular free-standing type under different frequency or voltage (scale bar, 5 cm).

the SPL acquired from the back-side are at the same level, whereas the SPL acquired from the front-side shows higher levels than the back-side and with higher envelopes for higher

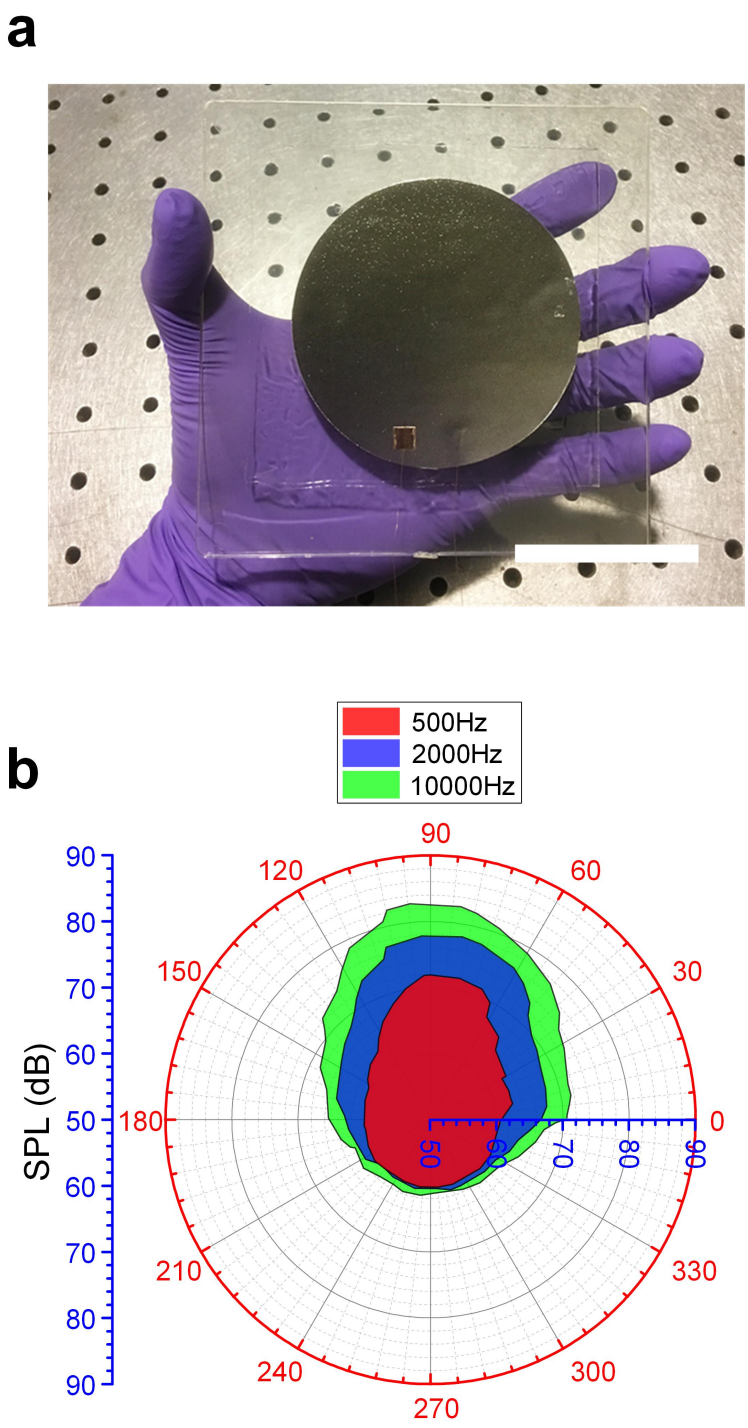

Figure 5.8 (a) Optical images and (b) SPL polar plots of circular type with soft acrylic as substrate under different frequency or voltage (scale bar, 5 cm).

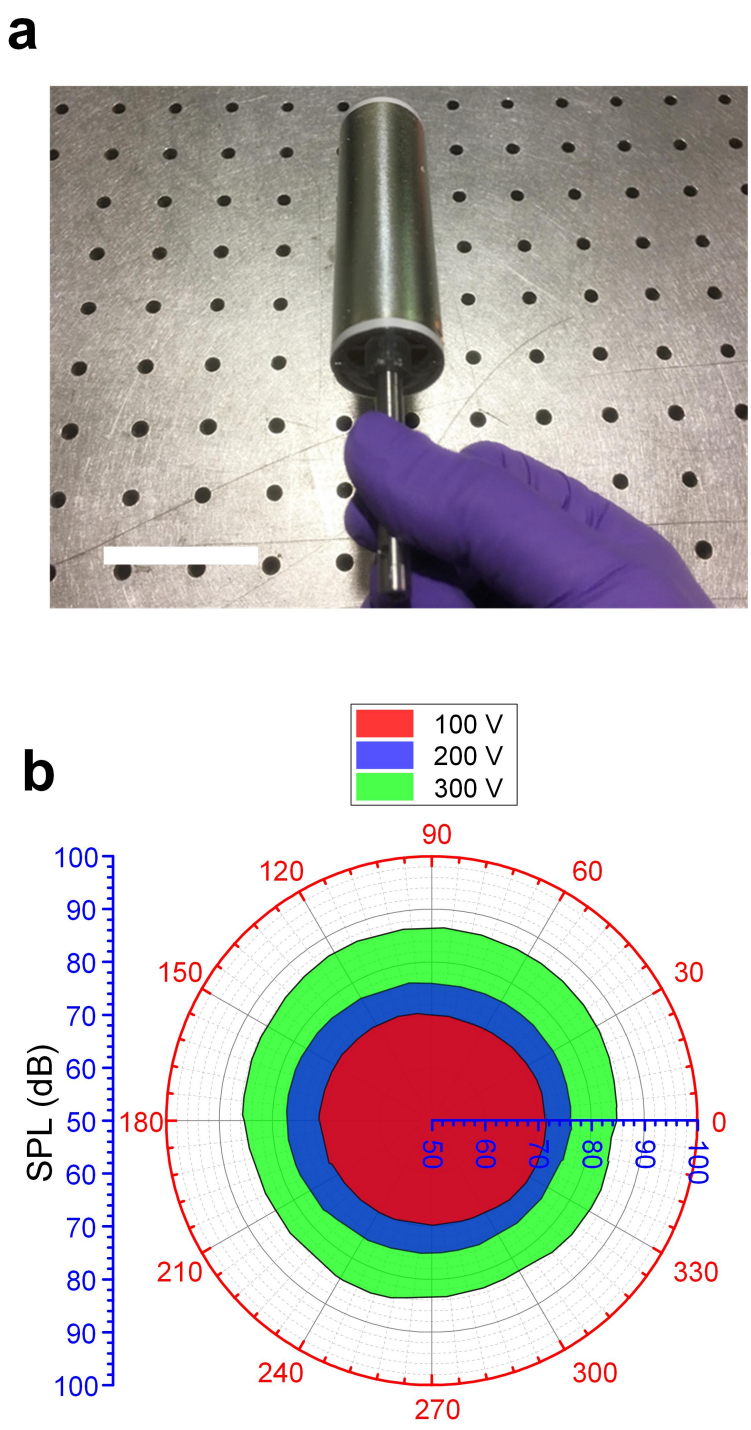

Figure 5.9 (a) Optical images and (b) SPL polar plots of rolled cylindrical type under different frequency or voltage (scale bar, 5 cm).

frequencies. Compared to the free-standing configuration, the one-surface blocked FENG-based loudspeaker attenuates great part of the radiation emitted in the substrate's direction; but it has the added advantages of robustness, and ease for installation, which could be found very beneficial for industry and civil applications.

The third FENG loudspeaker configuration consists of a rolled-up device in a cylindrical shape (Figure 5.9(a)) with both perimeter and length of 8 cm. The SPL directivity 5 kHz for different input voltages (100 V, 200 V and 300 V) is shown in Figure 5.8 (b). The central symmetry makes this device an omnidirectional loudspeaker, which theoretically would have the same directivity factor at every listener angle. Moreover, the SPL increases with the input voltage because larger voltage would increase the amplitudes of expansion or contraction of giant dipoles inside the FENG, so as to produce larger displacement in thickness direction and create larger sound pressure.

5.4 Amplitude-Frequency Response and Music-playing Flag

Further characterization is carried out by measuring SPL versus frequency response from 10 Hz to 20 kHz (Figure 5.10). In this case, the positions of both FENG-based loudspeakers and the microphone system are fixed. A network/spectrum analyzer is used for sweeping the frequency of an voltage signal applied to the FENG-based loudspeaker through a low-noise voltage amplifier and also to measure the output voltage of the microphone system. The curve displayed in the network analyzer represents the SPL spectrum.

The first FENG-based loudspeaker configuration consists of squared free-standing configurations with different areas: 4 cm $\times$ 4 cm, 5.7 cm $\times$ 5.7 cm, and 8 cm $\times$ 8 cm. Figure 5.11 shows the SPL frequency spectrum for the three devices. It can be seen that the amplitude of SPL increases with the input frequency at the relatively low frequency range ($10-5000$ Hz), after which the amplitude of SPL approaches saturation. As shown, The FENG-based loudspeaker has a wide coverage of frequency which is sufficient to overlay the auditory per-

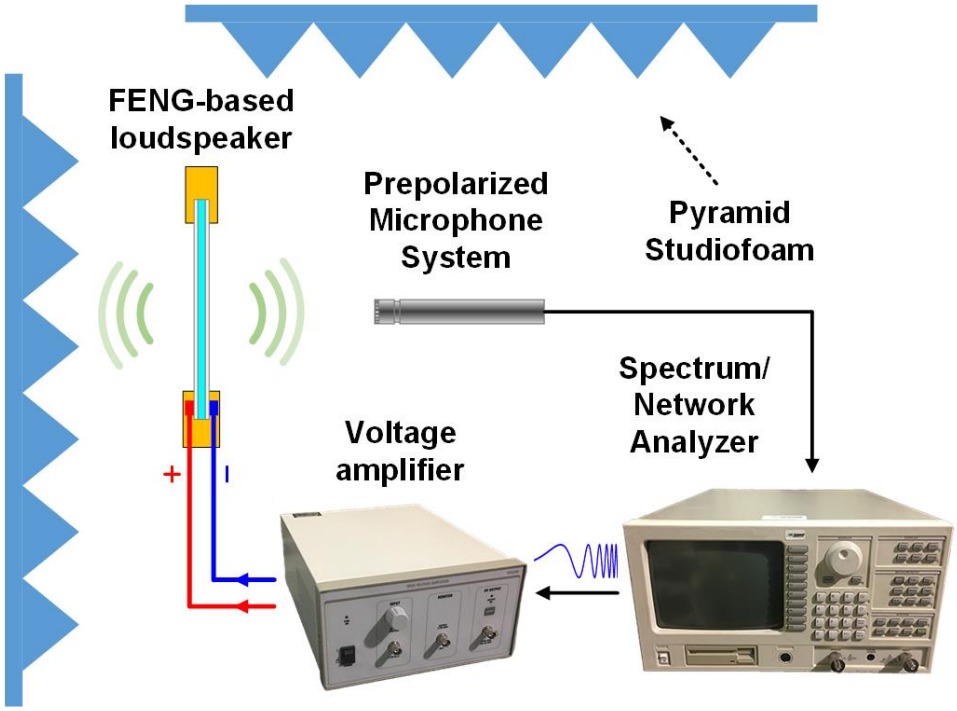

Figure 5.10 Measurement and connection scheme of SPL amplitude-frequency response for FENG-based loudspeaker.

ception frequency range of human, which is $\sim$ 20 Hz to 20,000 Hz [189, 190]. Moreover, it can be observed that the larger FENG-based loudspeakers produced larger SPL, which is expected, since larger devices represent larger "point sources". Due to the paper-like flexible thin film structure of the FENG-based loudspeaker, a single-layer device can be folded and stacked to form a multi-layers structure, where the giant dipoles in adjacent layers (in contact after folding) have same charge polarity orientation. After stacking, the polarity of each layer (now composed of two FENG surfaces with same polarity) will be opposite to the one below and above, resulting in electric fields pointing to (or leaving from) alternating layers across the device's thickness.

In the SPL directivity measurement, 1/2" prepolarized Microphone & preamplifier system (378A06, PCB Inc.) with sensitivity of 12.6 mV/Pa, and sensor signal condintioner (484B06, PCB Inc.) were used to measure the sound pressure. Precision potentiometer (Rourns Inc.) read the angle of FENG-based loudspeaker during the rotation process. The input

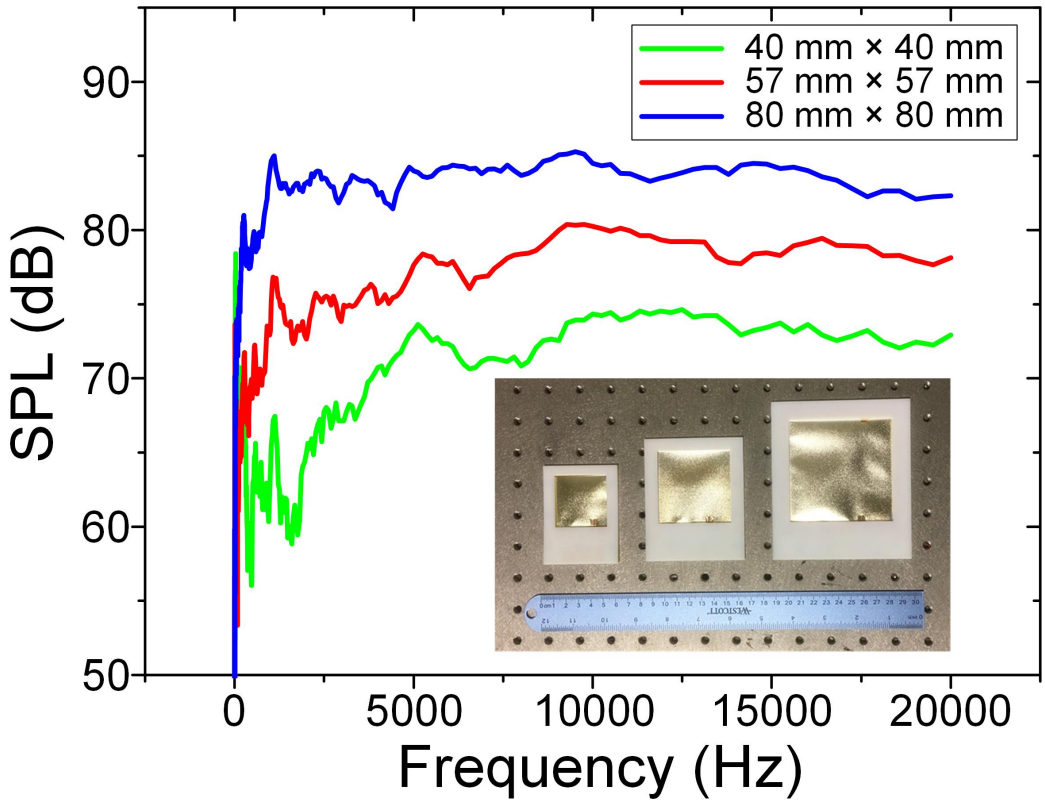

Figure 5.11 SPL frequency spectrum measurements from 10 Hz to 20 kHz for free-standing configuration of FENG-based loudspeaker. The insets show optical images of the configuration with the size ratio of 1:2:4.

signal is generated by an arbitrary Waveform generator (3390, Keithley Inc.) through a voltage amplifier (HVA 200, Thorlabs Inc.). Up to 300 V and 60 V are used for SPL directivity and frequency-response measurements, respectively. In the frequency-response measurement, a spectrum/network analyzer (3589A, Hewlett-Packard Inc.) is employed. The distance between the center of FENG-based device and the head of microphone system for all the measurement is 12 cm. The output signals of all measurement were acquired by an integrated real-time Controller (cRIO-9075) with an analog input module (NI 9201, National Instruments Inc.).

Figure 5.12 shows the relationship between SPL and the layers of FENG loudspeaker with same area (8 cm × 8 cm). For the stacked multi-layers FENG-based loudspeaker, we can see that the SPL increases with the number of layers, which is similar to the effect we obtained

from increasing size of one layer structure. This indicates that the performance of FENG loudspeaker can be enhanced by increasing layers through simple folding or stacking. The third configuration is designed to obtain the effects of adding a substrate on the frequency response of the FENG.

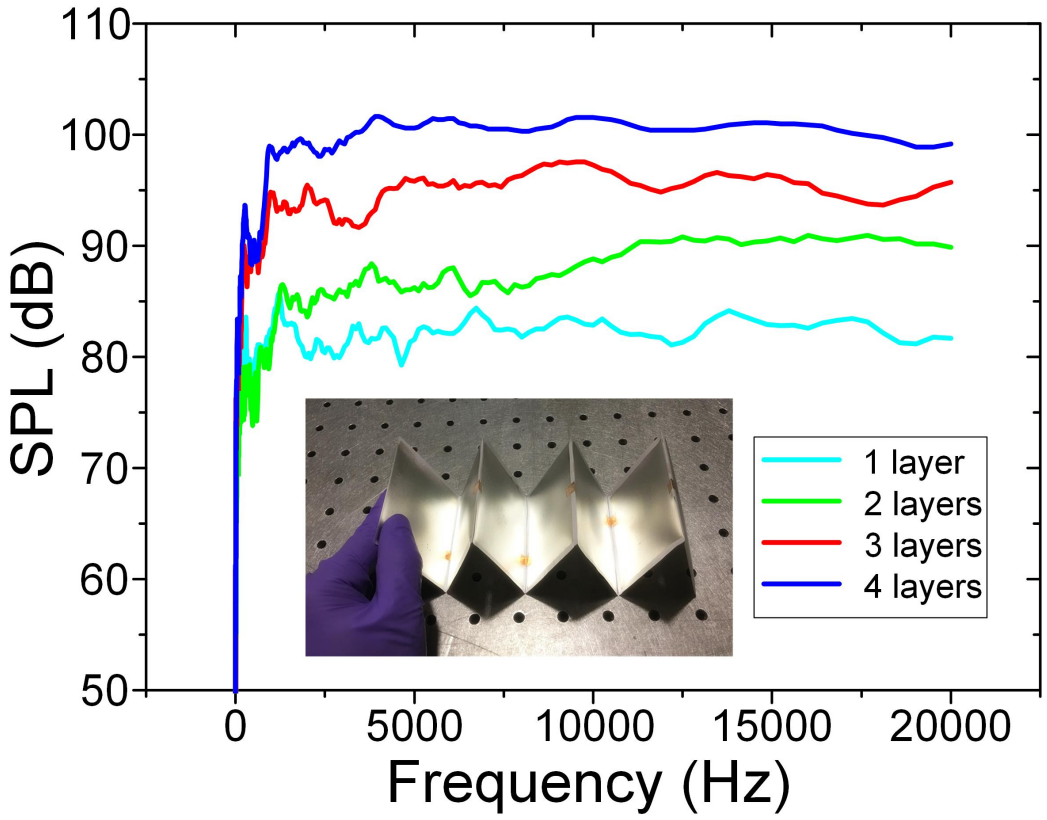

Figure 5.12 SPL frequency spectrum measurements from 10 Hz to 20 kHz for folded or stacked multi-layers configuration of FENG-based loudspeaker. The insets show optical images of the configuration

Figure 5.13 shows the SPL frequency spectrum of a free-standing FENG-based loudspeaker, with and without an acrylic substrate. Although there is a difference between these two SPL amplitude-frequency responses caused by the substrate, the FENG-based loudspeaker adhered to soft acrylic still produces an SPL of $\sim$ 73 dB (a decrease of $\sim$ 8 dB in comparison with free-standing configuration) while keeping a similar amplitude-frequency behavior.

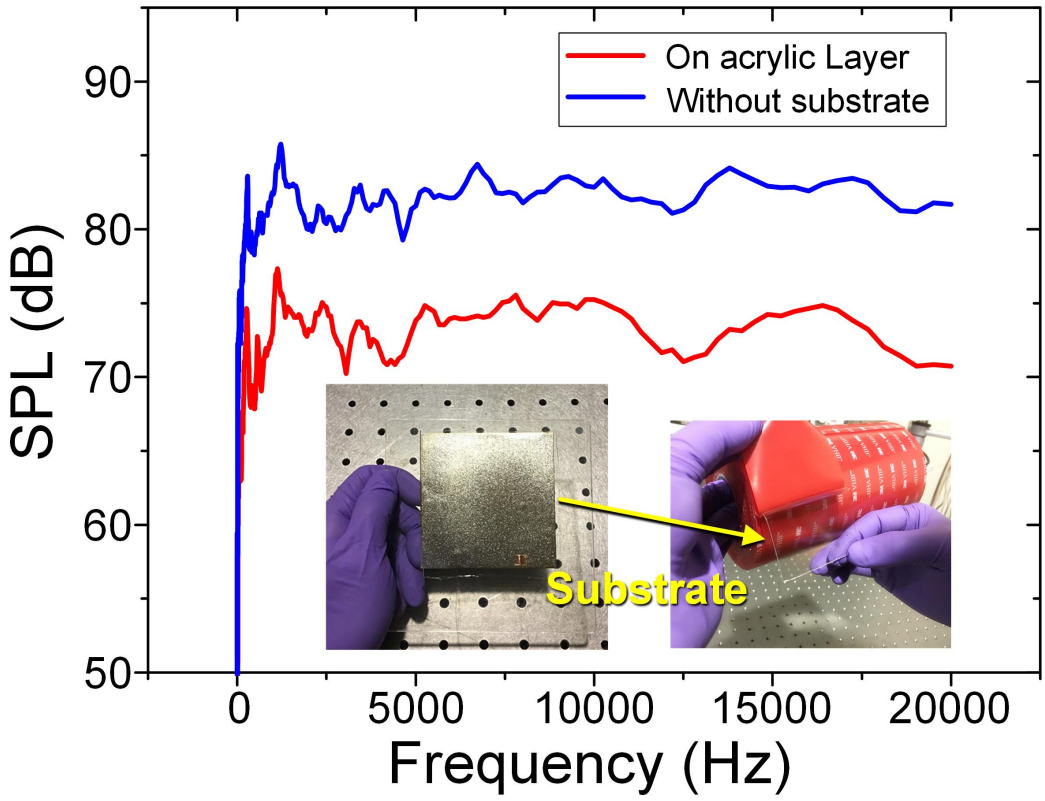

Figure 5.13 SPL frequency spectrum measurements from 10 Hz to 20 kHz for with and without substrate configuration configuration of FENG-based loudspeaker. The insets show optical images of the configuration

To demonstrate the performance and the potential applications of flexible FENG loudspeaker, we fabricated a music-playing Michigan State University (MSU) flag, as shown in Figure 5.14. Nine patches of single layer FENG-based loudspeaker (7 cm × 8 cm) were arranged to form a 3 × 3 matrix. The electrical positive surface and negative surface of all patches are aligned to the same flag's surface end connected tot the same electrical node. In other words, all the positive sides of the FENG-based loudspeaker are facing one side of the flag and electrically connected in series; while the negative sides are facing the other side and also electrically connected in series. Copper wires are used for the electrical connections inside the flag. The whole matrix was then embedded into two fabric layers of flag (28 cm × 33 cm). For the multi-layers structure, the surfaces with the same polarity of single FENG-based loudspeaker are stacked face-to-face (i.e. in electrical contact). Copper tapes

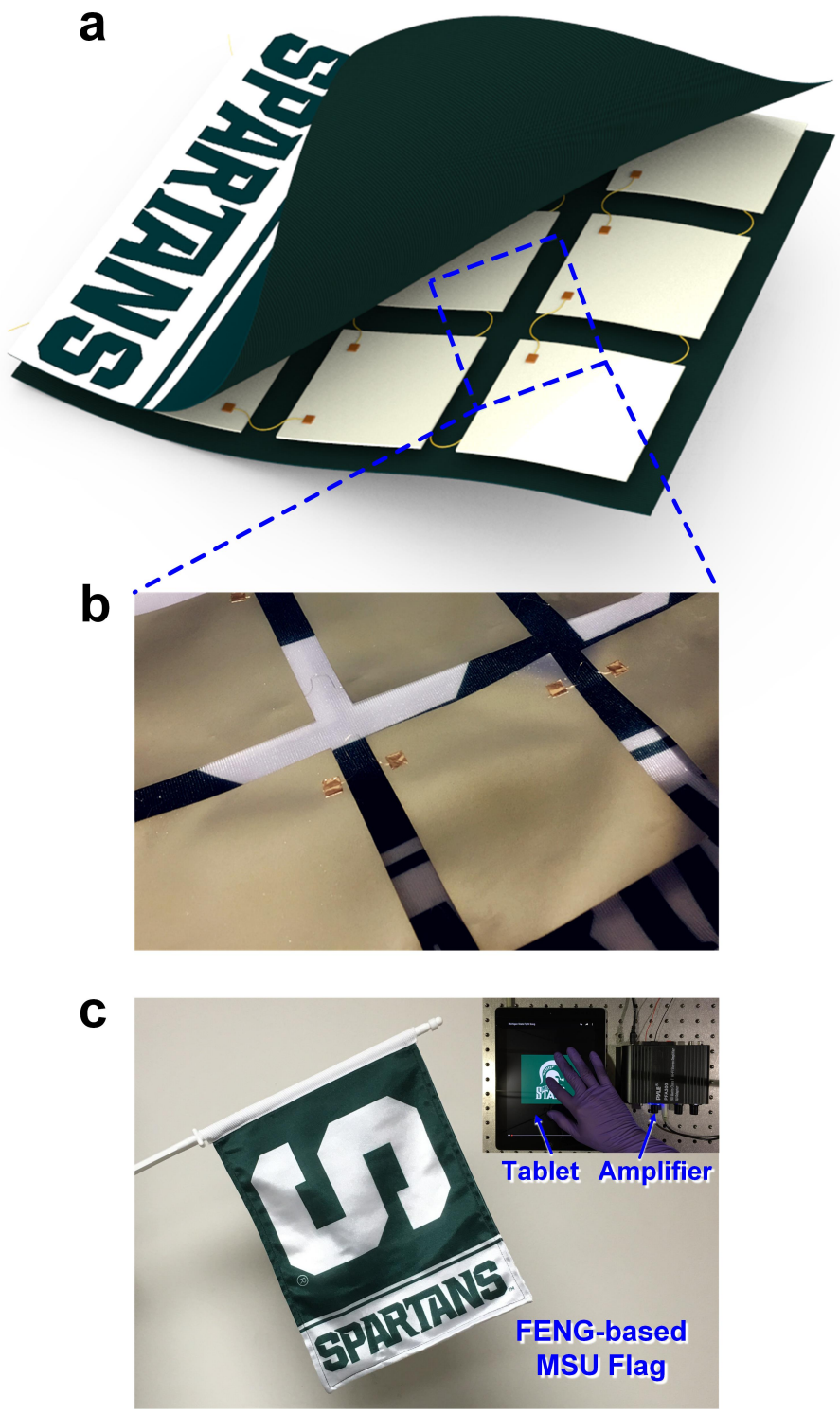

Figure 5.14 Design and demonstration of MSU music-playing flag. (a) Schematic diagrams. (b) Expanded optical image of the matrix. (c) Functionality demonstration.

were used to connected adjacent faces. Last, two copper wires were used as positive and negative electrodes.

The developed flag can be waved, rolled, or folded –just like any other flag– and has no evident physical or cosmetic difference from any other. A matrix of FENG-based loudspeakers is embedded between two fabric layers. It consists of nine patches of single layer free-standing FENG-based loudspeakers with area of 7 cm $\times$ 8 cm. Both sides of their surfaces are electrically connected by copper wires. Like free-standing single layer structure, the matrix of FENG-based loudspeaker is capable of producing sound pressure from both sides (Figure 5.14 (a) and (b)), which easily transmits through the fabric layers. This FENG-based music-playing flag features high output SPL and wide audio frequency range, as well as lightweight, flexibility which derive from the nature of thin film and the separated matrix configuration. As a demonstration (Figure 5.14 (c)), a marching band music with a variety of instruments is played by the developed music-playing flag while waving in the air. In addition, the layered thin film configuration allows the merits of not only being tailored into different shapes and sizes according to applications, but also being placed on a variety of rigid or flexible surfaces, as well as their free-standing use.

5.5 Principle and Performance of FENG-based Thin Film Microphone

Microphones operate, essentially, in the opposite way than a loudspeaker. Microphones are electroacoustic transducers that transform acoustic vibrations into electrical signals. Today, acoustic sensing has been dominated by electret microphones which has permanently charged dielectric avoiding the use of DC bias [191, 192, 193]. The reversible electromechanical interaction between the electrical and mechanical states of FENG allows the device to operate as a microphone, while still keep its loudspeaker functionality. There are two particularities of FENG that makes its use as a microphone very promising. First, the large

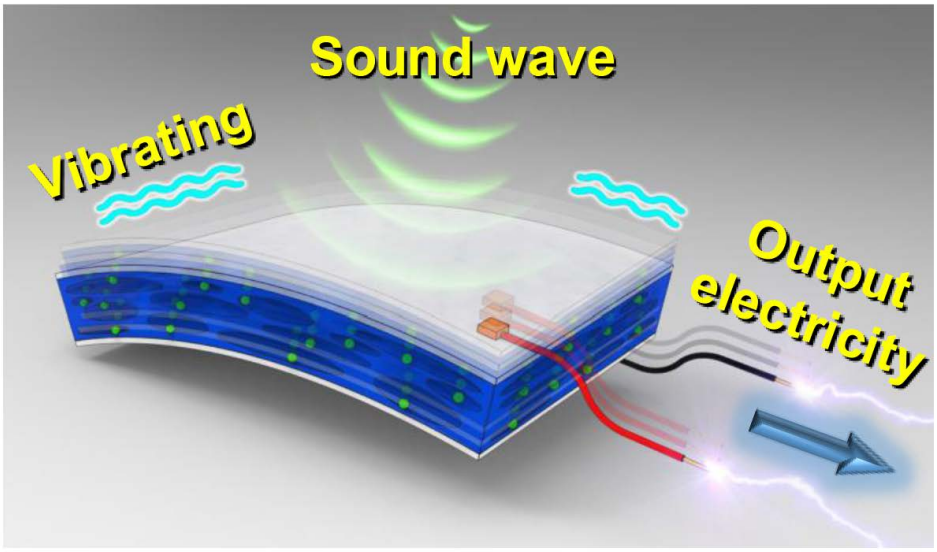

Figure 5.15 Mechanism of the transformation from acoustic energy to electric energy.

charge accumulation on its surfaces give the device a high electromechanical transformation efficiency; which means that large electrical signals can be produced from small mechanical vibrations. Second, the massive giant voids make it a hollow foam film with a low Young's modulus (1500 N mm^{-2}) [185] in its thickness direction. Therefore, the external sound pressure generated from music or voice is sufficient to create vibrations along the FENG's thickness large enough to produce detectable electrical signals (Figure 5.15). In other words, sound vibrations from voice or music generate a similar effect on the FENG than applying mechanical pressure perpendicular to the surface.

The sensitivity of the FENG-based microphone can be demonstrated by recording the electrical signals produced due to external sound or music, and then comparing the quality of the recorded sound to the original. To this end, a FENG-based microphone system was built to record a famous aria "La Traviata, Brindisi (Verdi)", as shown in Figure 5.16. This testing song is originally performed by a soprano and a tenor, accompanied by symphony orchestra. Thus, different pitches from the two artists and a variety of instruments are included in the test. The tablet's output electrical signal is sent to an audio amplifier, which drives a traditional electromagnetic loudspeaker to produce sound wave. The sound wave compresses

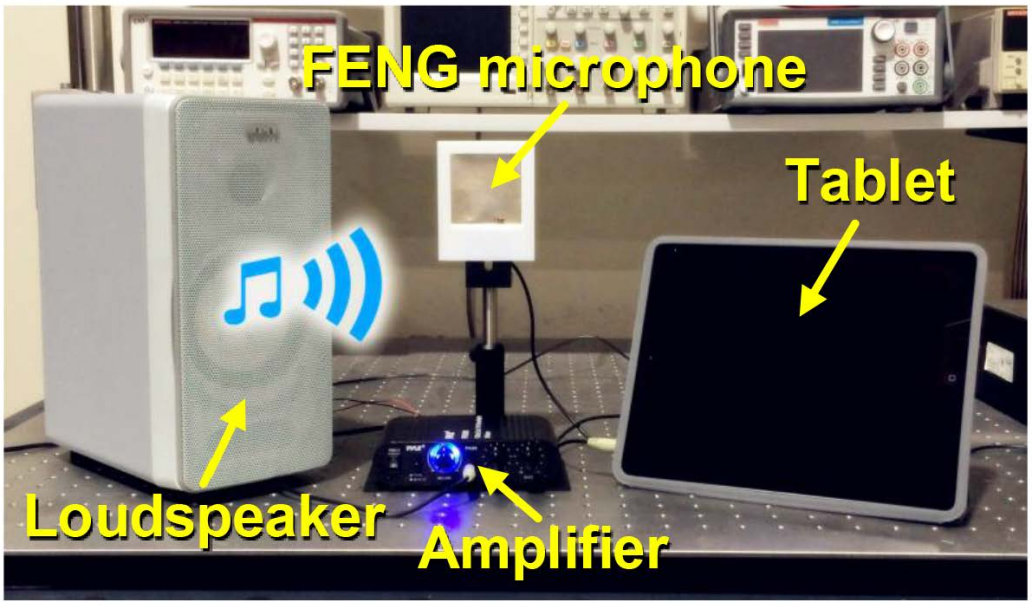

Figure 5.16 Experiment of FENG-based microphone system for recording music "La Traviata, Brindisi (Verdi)".

the nearby air, which in turn presses the FENG-based microphone. The generated electric signals from the FENG microphone are then recorded. This setup resembles the typical use of a commercially available microphone, where an AUX cable is connected to a PC with an audio card that can record audio. The direct mechanical-to-electrical energy conversion allows the use of the FENG-based microphone for the real-time recording of the music played by the tablet.

The time-domain sound wave signals and the acoustic spectrograms for the original music (tablet's output) and the recorded music (FENG-based microphone's output) are shown in Figs. Figure 5.17 and Figure 5.18, respectively. It can be seen that the acoustic information of the recorded music is highly similar to that of the original music, even for a small piece. A video demonstrates the FENG-based microphone effectively copies the music or voice it "hears" with high quality and fidelity. It is worth mentioning that the FENG-based microphone and loudspeaker are essentially the same structure, but employ opposite reversible electromechanical interaction effects, which means the FENG-based loudspeaker/microphone

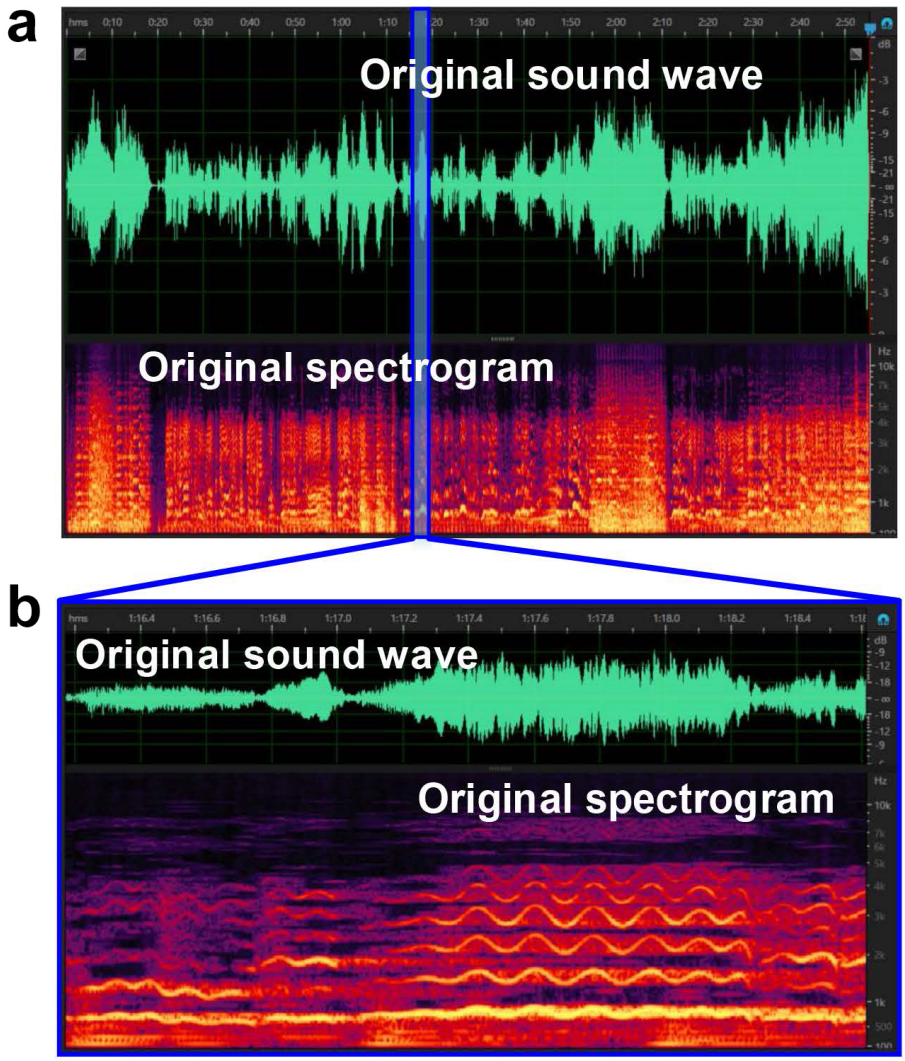

Figure 5.17 (a) Sound wave and acoustic spectrogram of original music. (b) Expanded and detailed view of a small piece of original music.

is genuinely a dual-functional acoustics device. According to the user's requirement, FENG could conveniently switch its functionality.

5.6 FENG-based Identity Recognition for Privacy Security Application

Driven by the rapidly increasing demand of global markets, wearable/portable device are continuously pursuing for improvements of human-machine interactions. Along with this trend,

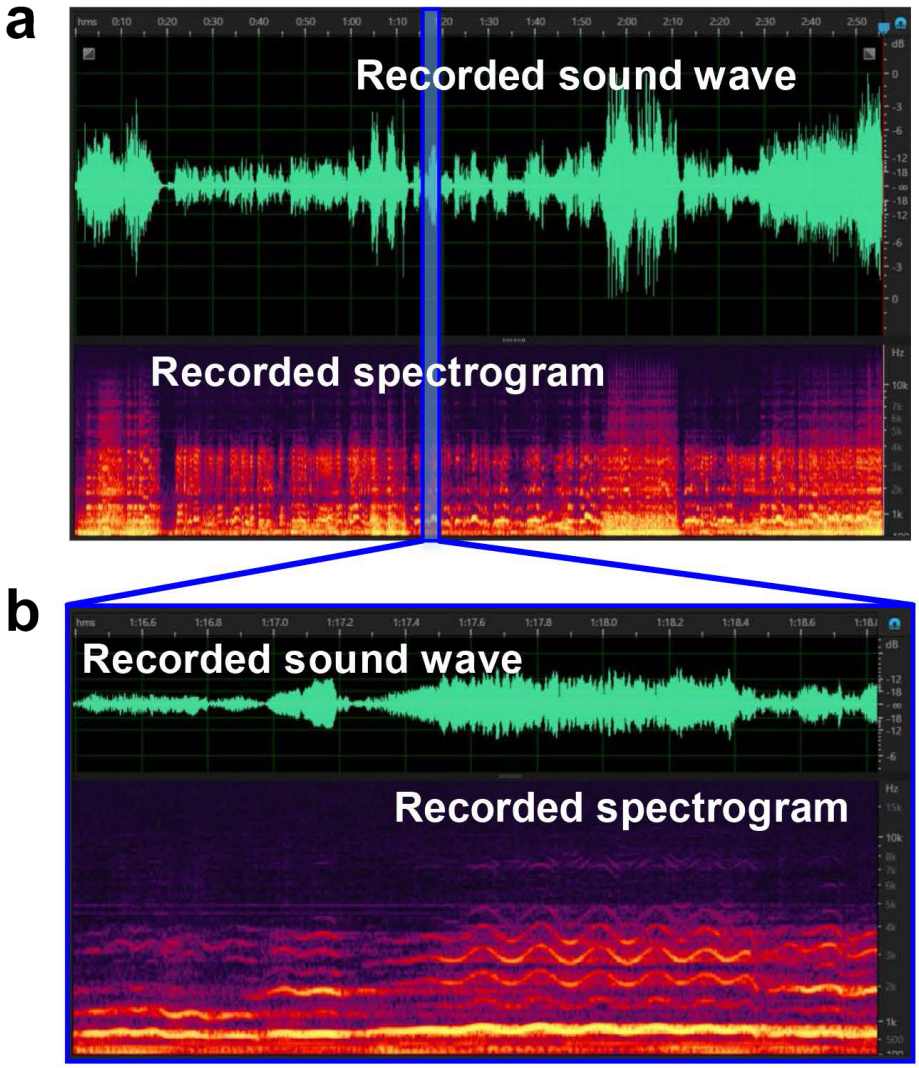

Figure 5.18 (a) Sound wave and acoustic spectrogram of recorded music. (b) Expanded and detailed view of a small piece of recorded music.

wearable/portable flexible electronic devices are poised to collect more and more personal information (e.g. social contact information, daily GPS positioning, or even physical activity and healthy status) from users. Therefore, privacy and security will become performance parameters that need to be addressed.

The excellent voice recording performance of FENG, as well as its light-weight and flexible thin film structure may open up new possibilities in privacy and security applications of flexible electronics. The most typical security protocol standing between an unauthorized

user and a personal computer or a portable/wearable personal gadget with private information is a "typed password". In this security protocol, the password text can be either compromised or hacked. The high sensitivity of the FENG-based microphone allows for voice recognition, which enables an extra security layer by replacing the "password typing" process by a "password speaking" process. In this security application, the system recognizes both, the text password and the authorized user's voice. Given the FENG's flexibility and demonstrated wearability, a FENG device can be discreet and even unnoticeably installed within the wearable gadget or personal computer, and then used to determine the user's identity and grant access. Figure 5.19 show the process of using FENG as a "watch-dog" to prevent unauthorized users from accessing to the owner's personal PC even in the case when unauthorized users obtain the correct voice code.

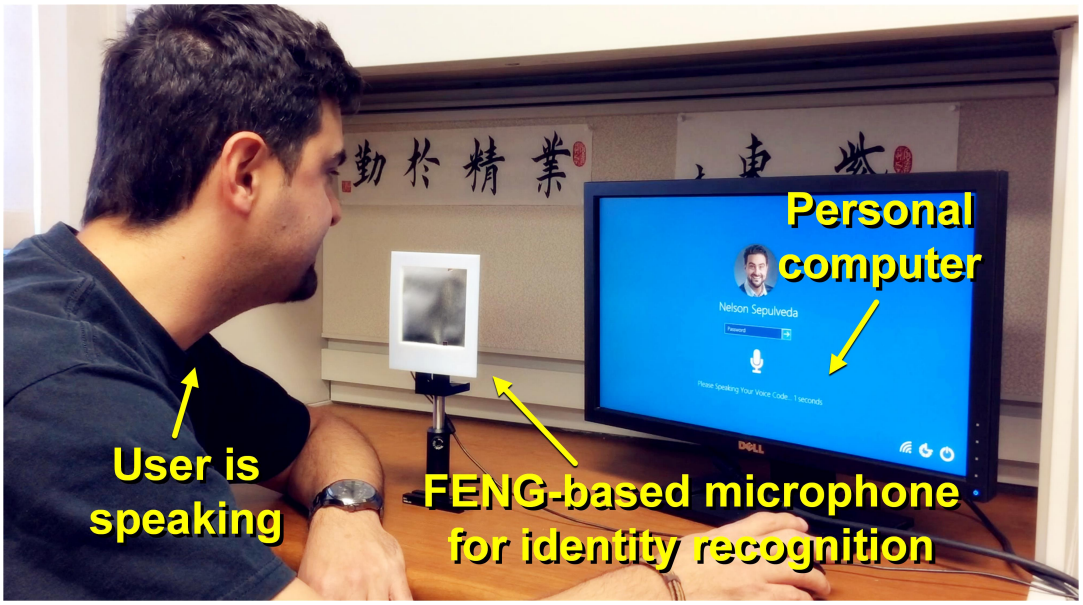

Figure 5.19 Demonstration of FENG-based identity recognition along with other potential applications of FENG.

Although all testers in this demonstration spoke the correct voice password "OPEN SESAME", the FENG-based microphone was used to analyze their voiceprints according to designed algorithm and ultimately only give access to the one with voiceprint matching the previously saved database, which is the authentic user. Herein, we designed Mel-frequency

cepstral analysis with artificial neural networks model [194, 195, 196] to realize the users' identity recognition based on FENG (Figure 5.20).

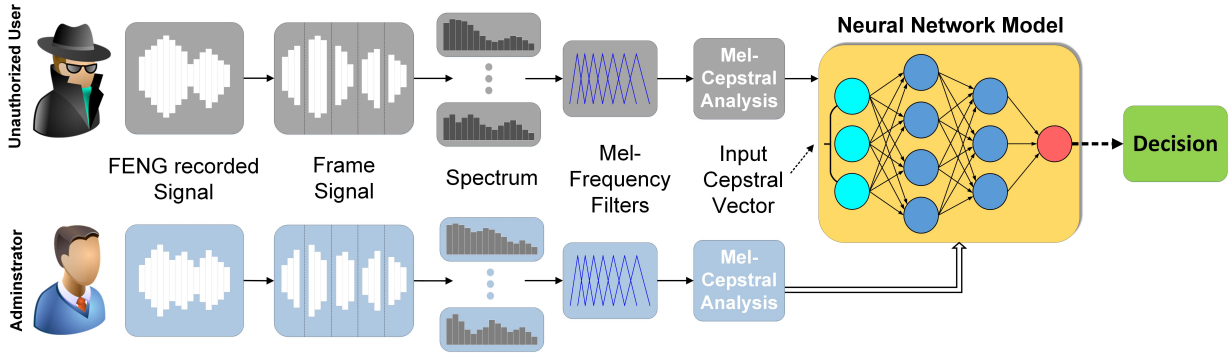

Figure 5.20 Schematics of recognition algorithms based on Mel-frequency cepstral analysis with artificial neural networks model.

As the unauthorized user spoke to FENG in request for access, his or her voiceprint information (Figure 5.21, 5.22, 5.23) was analyzed, which reflected individual's discrepancy of physical shape of vocal tract [197, 198]. The generated voltage due to sound pressure (Figure 5.21) reflects time-domain acoustic information; the spectrogram (Figure 5.22) shows the frequency-domain acoustic information; and the periodogram power spectral density estimate (Figure 5.23) reflects the acoustic energy information. It can be observed that when two testers spoke the same voice code, the FENG-based microphone records their three key voice information, and accurately reveals the user's identity, which is indispensable for further privacy protection.

Such a simple paper-like, dual-functional acoustic devices will have broad and various promising applications (Figure 5.24). The flexibility of the FENG-based microphone allows for identity recognition system to be integrated not only in a variety of flexible electronic devices, but also portable thin cards, such as ID cards and debit or credit cards. Besides, such advantages might open up new prospects to the design and fabrication of new-style loudspeakers, and the improvement of current active noise cancellations technology for automobiles, aircrafts and submarines, etc.

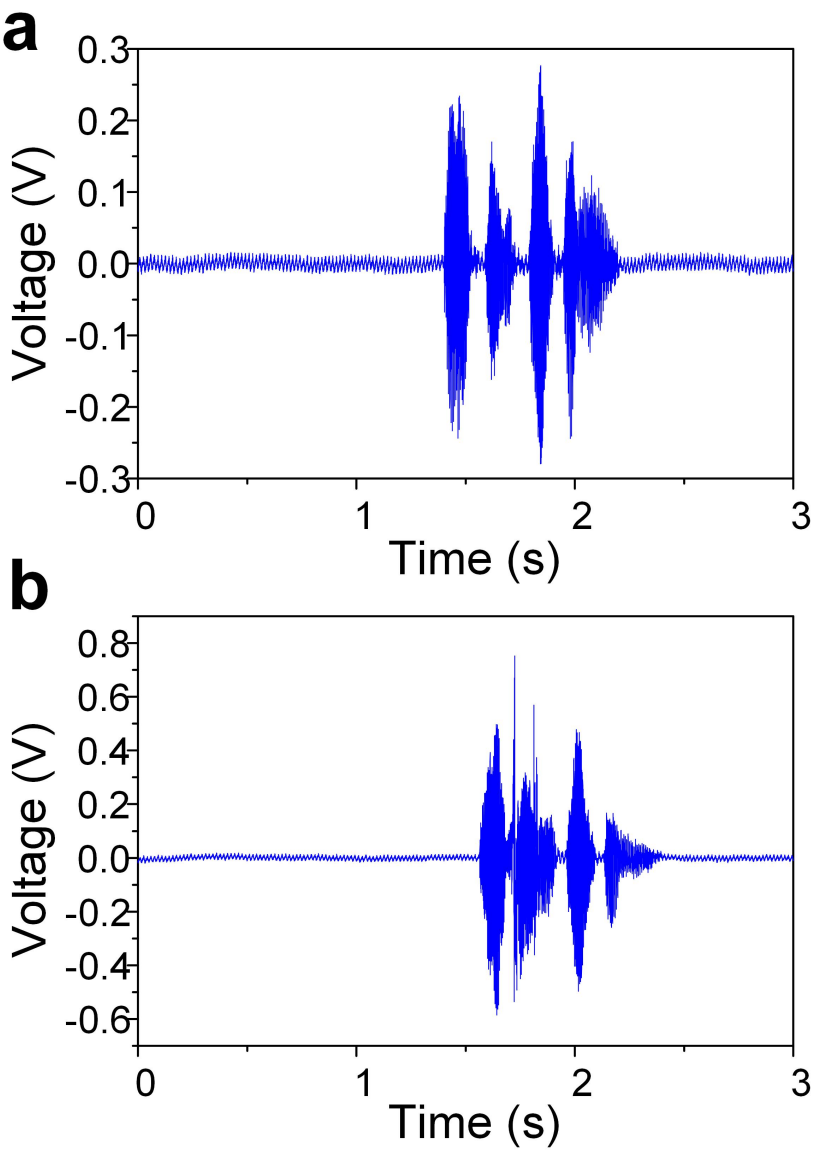

Figure 5.21 Sound wave of voice code "OPEN SESAME" spoken by the (a) administrator and (b) an unauthorized user.

5.7 Summary

The applicability of the FENG device is here expanded beyond energy harvesting applications. The strong electromechancial coupling of FENG gives the device the particular dual-functional capability of using sound to produce electricity, and using electricity to produce sound. The SPL for three different FENG configurations (free-standing, substrate-held,

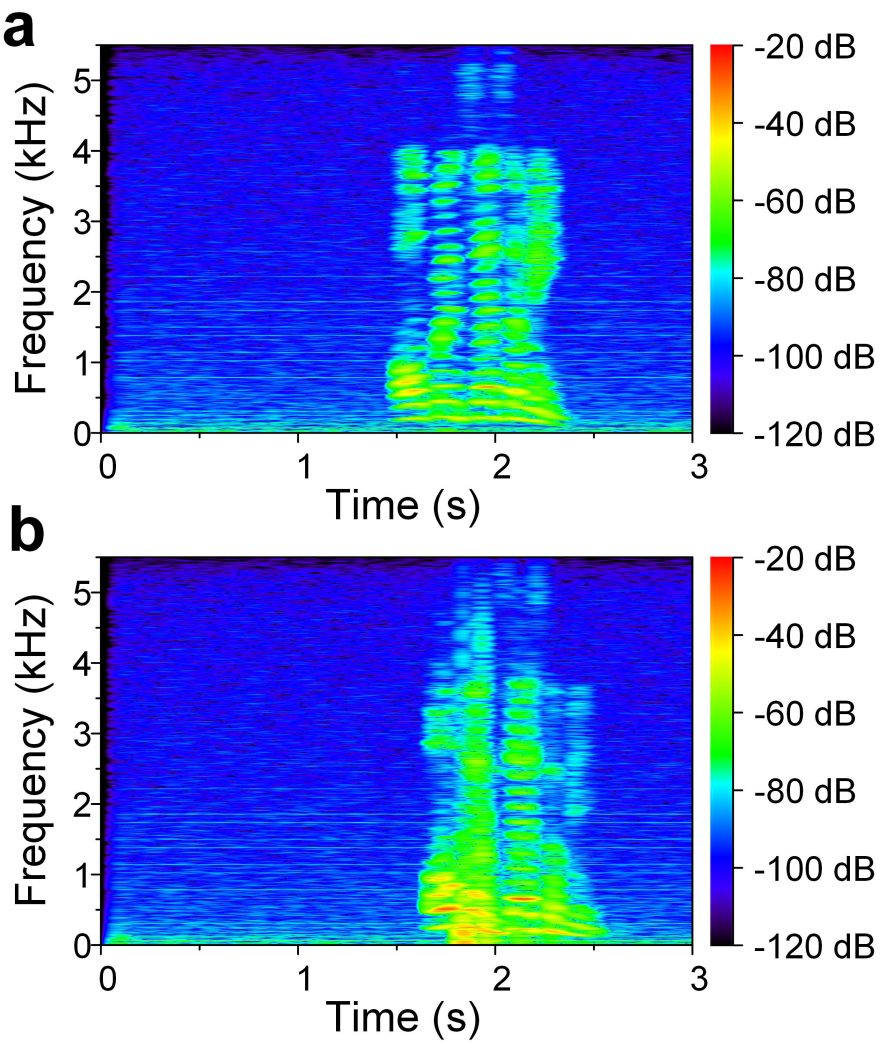

Figure 5.22 Spectrogram of voice code "OPEN SESAME" spoken by the (a) administrator and (b) an unauthorized user.

and rolled-up FENGs) is characterized as a function of space and frequency in the range of the human audible range. The device is implemented in three systems, which demonstrated the application of the device for developing music-playing flexible flags, and flexible patches that can be used for recording music with high fidelity or discreet devices that can reveal the identity of individuals trying to gain access to a personal computer.

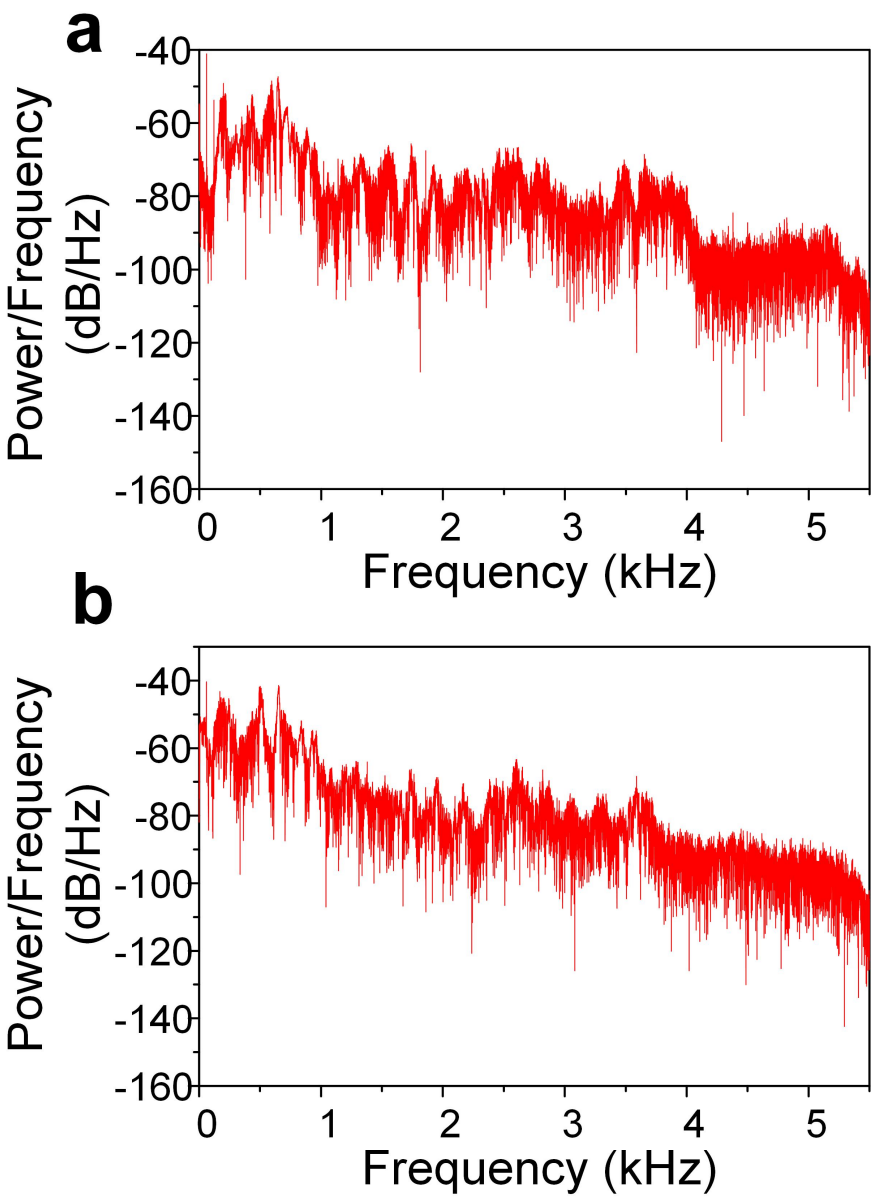

Figure 5.23 Periodogram power spectral density estimate of voice code "OPEN SESAME" spoken by the (a) administrator and (b) an unauthorized user.

Figure 5.24 Various applications of FENG-based acoustic device.

CHAPTER 6

CONCLUSIONS AND FUTURE WORK

6.1 Summary of Thesis

In this thesis, ferroelectret nanogenerator (FENG) is introduced in the field of thin film nanogenerator which aims at harvesting mechanical energy from environment. The designs, fabrications, simulations, characterizations and applications of this technology is explored. Theoretical and experimental results, as well as a couple of prototype devices shown in thesis offer a glimpse into a potential future for this technology. The accomplishments of this thesis are summarized as follows:

1. *Preliminary Work – Flexible Nanogenerator Based on Nanocrystalline AlN Thin Film:* the development of a flexible nanogenerator based on nanocrystalline aluminum nitride (AlN) thin films deposited at room temperature is reported. The AlN thin film was grown by pulsed laser deposition (PLD) on a thin aluminum layer. X-ray diffraction and transmission electron miscroscope images show that the AlN films consist of crystalline columnar grains oriented in the (100)-direction. A polyimide thin film encapsulated the flexible NG to further improve mechanical robustness, protecting the device from abrasion, and enhance its potential biocompaibility.

2. *Flexible and Biocompatible FENG – Rationale & Applications:* a different operating mechanism to the field of flexible thin film nanogenerators based on polypropylene ferroelectret (PPFE) which harvests mechanical energy from human motion is introduced. Flexible, foldable, biocompatible, highly efficient thin film ferroelectret nanogenerators (FENGs) is demonstrated. The devices comply with the flexibility, wearability, lightweight, and portability demands mentioned earlier. A FENG with

surface area more than 300 cm^2 is demonstrated in this paper by using bar-coating technique [141]; they can also be folded to sizes smaller than 1 cm^2 and generate higher electric potentials. Furthermore, their simple fabrication allows for encapsulated low-cost devices. In view of the environment, health, and safety, the fabrication of encapsulated FENG avoids the use of harmful elements (e.g. lead) or toxic materials (e.g. carbon nanotubes), making it more attractive for biocompatible and perhaps even implantable applications. Through FEM, the mechanical-electrical energy conversion mechanism of FENG was studied; and the relationship between internal stress, change of electric filed, and charge transport are investigated. Due to its thin film structure, the device can be bent or even folded easily. Further experiments show that both the open-circuit voltage (V_{oc}) and short-circuit current (I_{sc}) are doubled with each folding along an axis of symmetry. Since V_{oc} and I_{sc} are doubled with each folding action, the output power of the FENG can be easily and significantly increased. Electrical output produced by the device for time-dependent mechanical input is also studied. Additionally, device electrical output for different pressure input magnitudes (while keeping the frequency constant), and for different frequencies (while keeping the magnitude constant) are investigated. The results revealed the frequency- and pressure-dependent properties of the developed device. Finally, we developed FENG-based systems for three niche applications: *1) Illumination:* we demonstrate that the energy harvested by a stacked FENG (60 mm × 60 mm, 7 layers) is able to power 20 commercial green and blue LEDs connected in series; *2) Self-powered touch liquid crystal display (LCD):* this touch screen scavenges energy from finger touch to supply power during operation; and *3) Flexible/foldable keyboard:* this thin film-based keyboard is powered by harvested energy from each keystroke, and its size can be reduced by simple folding, thus enabling portability.

3. *FENG-based dual-functional thin patch loudspeaker/microphone for flexible electronics:* a dual-functional and self-powered thin film flexible acoustic transducer,

which operates as both loudspeaker and microphone is reported. Based on ferro-electret nanogenerator (FENG), the device has the ability to produce power as well. By means of microplasma discharging, the artificial voids inside the foam-structured FENG forms numerous giant dipole which enable the FENG with outstanding electromechanical transformation efficiency. The thesis describes the mechanisms for direct and reverse interaction effects (i.e. using mechanical energy to produce electrical energy, and using electrical energy to produce mechanical energy), which are the cornerstones of the present FENG-based loudspeaker/microphone device. Characterization of the performance of the FENG-based loudspeaker is done by SPL directivity measurements for three developed configurations: free-standing FENG, FENG attached to a soft substrate, and rolled FENG in cylindrical shape. Moreover, the amplitude-frequency response (10 – 20,000 Hz) for the present FENG-based loudspeaker is characterized as a function of functional area, number of layers, and for cases with or without substrate. To demonstrate the applicability and functionality of the device, a FENG-based music-playing flag which can operate under regular wind conditions is fabricated. Due to the electro-mechanical coupling of the device, the operation of the FENG-based loudspeaker can be reversed, to result in a FENG-based microphone that converts acoustic vibration (sound) into an electrical signal. The FENG-based microphone is highly sensitive to a broad range of frequency. This is shown by the other two demonstrations presented in this work; which include the recording of a symphony by a piece of paper-like FENG-based microphone with high fidelity, and the security of a personal computer by the voiceprint identity recognition through a FENG-based device that can easily be integrated secretly within a computer or personal device for added subtlety.

6.2 Future works

Although a couple of promising applications of ferroelectret nanogenerators has been demonstrated herein, however, this thesis may just takes a peek under the hood at its enormous potential. There is no doubt that there exist other attractive topics or interesting applications waiting for being discovered. To assist future research, several possible investigation topics are summarized as follows:

1. In 2010, a new mechanism for actuation was introduced [199]. The mechanism is based on the use of the crystallographic changes of vanadium dioxide (VO_2) thin film across its structural phase transition (SPT) which occurs at 68°C, and the VO_2-based device can be easily driven by electric signals (i.e. joule heating) [200]. Due to the generation of electric signals and thin film structure, FENG could be a good candidate of power supplier for smart material VO_2. By integrating FENG and VO_2, perhaps a couple of interesting devices could be proposed in the future.

2. Polymer light-emitting electrochemical cells (PLECs) have been widely studied for various applications, including flexible flat panel display, signage and lighting [201]. PLEC can be fabricated into a thin film structure by using all-solution-based processes which are easily scaled up. Since both FENGs and PLECs are thin film, and FENGs have already been demonstrated to be able to provide power for commerical LEDs, if FENGs and PLECs could be integrated into one device with a thin film structure, it would open a way to develop a thin film structure, flexible and rollable, self-powered colorful display for flexible electronic devices.

3. As introduced in previous chapter, triboelectric nanogenerator (TENG) is also promising technology for mechanical-to-electrical energy conversion. Since TENG currently dominates the field of nanogenerator, not only a lot of amazing experiments and device has been made, but also deep theoretical study has been done. If FENG and TENG could be integrated by taking advantages of both of their own merits,

it's possible that future researchers would come up with innovative nanogenerator with higher efficiency, smaller size, and wider range of application.

BIBLIOGRAPHY

BIBLIOGRAPHY

[1] V. Smil, "Energy in world history," 1994.

[2] "Difference engine: The nuke that might have been," *The Economist*, vol. Nov. 11, 2013.

[3] "Nuclear power: When the steam clears," *The Economist*, vol. Mar. 24, 2011.

[4] E. Simpson and I. Fairlie, "Dealing with nuclear waste is so difficult that phasing out nuclear power would be the best option," *London Free Press*, Feb. 26, 2016.

[5] O. Ellabban, H. Abu-Rub, and F. Blaabjerg, "Renewable energy resources: Current status, future prospects and their enabling technology," *Renewable and Sustainable Energy Reviews*, vol. 39, pp. 748–764, 2014.

[6] "Green gold," *Nature Energy*, vol. 1, p. 16011, 2016.

[7] S. Priya and D. J. Inman, *Energy harvesting technologies*, vol. 21. Springer, 2009.

[8] *http://www.iop.org/resources/energy/*.

[9] Y. Hu and Z. L. Wang, "Recent progress in piezoelectric nanogenerators as a sustainable power source in self-powered systems and active sensors," *Nano Energy*, vol. 14, pp. 3–14, 2015.

[10] J. A. Paradiso and T. Starner, "Energy scavenging for mobile and wireless electronics," *IEEE Pervasive computing*, vol. 4, no. 1, pp. 18–27, 2005.

[11] E. Romero, *Energy Harvesting from Body Motion using Rotational Micro-Generation*. PhD thesis, PhD Dissertation, Michigan Technological University, 2010.

[12] H. Häberlin, *Photovoltaics system design and practice*. John Wiley & Sons, 2012.

[13] G. J. Snyder, J. R. Lim, C.-K. Huang, and J.-P. Fleurial, "Thermoelectric microdevice fabricated by a MEMS-like electrochemical process," *Nature materials*, vol. 2, no. 8, pp. 528–531, 2003.

[14] F. Peano and T. Tambosso, "Design and optimization of a mems electret-based capacitive energy scavenger," *IEEE/ASME Journal of Microelectromechanical Systems*, vol. 14, no. 3, pp. 429–435, 2005.

[15] S. Meninger, J. O. Mur-Miranda, R. Amirtharajah, A. Chandrakasan, and J. H. Lang, "Vibration-to-electric energy conversion," *IEEE Transactions on Very Large Scale Integration (VLSI) Systems*, vol. 9, no. 1, pp. 64–76, 2001.

[16] S.-G. Kim, S. Priya, and I. Kanno, "Piezoelectric MEMS for energy harvesting," *MRS bulletin*, vol. 37, no. 11, pp. 1039–1050, 2012.

[17] K. C. Pradel, W. Wu, Y. Ding, and Z. L. Wang, "Solution-derived ZnO homojunction nanowire films on wearable substrates for energy conversion and self-powered gesture recognition," *Nano Letters*, vol. 14, no. 12, pp. 6897–6905, 2014.

[18] Y. Xie, S. Wang, S. Niu, L. Lin, Q. Jing, J. Yang, Z. Wu, and Z. L. Wang, "Grating-structured freestanding triboelectric-layer nanogenerator for harvesting mechanical energy at 85% total conversion efficiency," *Advanced Materials*, vol. 26, no. 38, pp. 6599–6607, 2014.

[19] P. Bai, G. Zhu, Q. Jing, J. Yang, J. Chen, Y. Su, J. Ma, G. Zhang, and Z. L. Wang, "Membrane-based self-powered triboelectric sensors for pressure change detection and its uses in security surveillance and healthcare monitoring," *Advanced Functional Materials*, vol. 24, no. 37, pp. 5807–5813, 2014.

[20] C. Dagdeviren, B. D. Yang, Y. Su, P. L. Tran, P. Joe, E. Anderson, J. Xia, V. Doraiswamy, B. Dehdashti, and X. Feng, "Conformal piezoelectric energy harvesting and storage from motions of the heart, lung, and diaphragm," *Proceedings of the National Academy of Sciences*, vol. 111, no. 5, pp. 1927–1932, 2014.

[21] Q. Zheng, B. Shi, F. Fan, X. Wang, L. Yan, W. Yuan, S. Wang, H. Liu, Z. Li, and Z. L. Wang, "In vivo powering of pacemaker by breathing-driven implanted triboelectric nanogenerator," *Advanced Materials*, vol. 26, no. 33, pp. 5851–5856, 2014.

[22] C. Dagdeviren, Y. Shi, P. Joe, R. Ghaffari, G. Balooch, K. Usgaonkar, O. Gur, P. L. Tran, J. R. Crosby, and M. Meyer, "Conformal piezoelectric systems for clinical and experimental characterization of soft tissue biomechanics," *Nature Materials*, vol. 14, no. 7, pp. 728–736, 2015.

[23] C. Dagdeviren, Y. Su, P. Joe, R. Yona, Y. Liu, Y.-S. Kim, Y. Huang, A. R. Damadoran, J. Xia, and L. W. Martin, "Conformable amplified lead zirconate titanate sensors with enhanced piezoelectric response for cutaneous pressure monitoring," *Nature Communications*, vol. 5, p. 4496, 2014.

[24] L. Persano, C. Dagdeviren, Y. Su, Y. Zhang, S. Girardo, D. Pisignano, Y. Huang, and J. A. Rogers, "High performance piezoelectric devices based on aligned arrays of nanofibers of poly (vinylidenefluoride-co-trifluoroethylene)," *Nature Communications*, vol. 4, p. 1633, 2013.

[25] D. Damjanovic, "Ferroelectric, dielectric and piezoelectric properties of ferroelectric thin films and ceramics," *Reports on Progress in Physics*, vol. 61, no. 9, p. 1267, 1998.

[26] J. Li, C. Wang, J. Ma, and M. Liu, "Micromachined ultrasonic transducers based on lead zirconate titanate (PZT) films," *Microsystem technologies*, vol. 19, no. 2, pp. 211–218, 2013.

[27] J. S. Pulskamp, R. G. Polcawich, R. Q. Rudy, S. S. Bedair, R. M. Proie, T. Ivanov, and G. L. Smith, "Piezoelectric PZT MEMS technologies for small-scale robotics and rf applications," *MRS bulletin*, vol. 37, no. 11, pp. 1062–1070, 2012.

[28] R. Maeda, J. Tsaur, S. Lee, and M. Ichiki, "Piezoelectric microactuator devices," *Journal of Electroceramics*, vol. 12, no. 1-2, pp. 89–100, 2004.

[29] M. S. Zarnik, D. Belavic, S. Macek, and J. Holc, "Feasibility study of a thick-film PZT resonant pressure sensor made on a prefired 3d ltcc structure," *International journal of applied ceramic technology*, vol. 6, no. 1, pp. 9–17, 2009.

[30] J. Soman and C. B. O'Neal, "Fabrication and testing of a PZT strain sensor for soil applications," *IEEE Sensors Journal*, vol. 11, no. 1, pp. 78–85, 2011.

[31] C. Dagdeviren, Y. Su, P. Joe, R. Yona, Y. Liu, Y.-S. Kim, Y. Huang, A. R. Damadoran, J. Xia, and L. W. Martin, "Conformable amplified lead zirconate titanate sensors with enhanced piezoelectric response for cutaneous pressure monitoring," *Nature Communications*, vol. 5, 2014.

[32] X. Chen, S. Xu, N. Yao, and Y. Shi, "1.6 V nanogenerator for mechanical energy harvesting using PZT nanofibers," *Nano Letters*, vol. 10, no. 6, pp. 2133–2137, 2010.

[33] K.-I. Park, J. H. Son, G.-T. Hwang, C. K. Jeong, J. Ryu, M. Koo, I. Choi, S. H. Lee, M. Byun, and Z. L. Wang, "Highly-efficient, flexible piezoelectric PZT thin film nanogenerator on plastic substrates," *Advanced Materials*, vol. 26, no. 16, pp. 2514–2520, 2014.

[34] Y. Qi, N. T. Jafferis, K. Lyons Jr, C. M. Lee, H. Ahmad, and M. C. McAlpine, "Piezoelectric ribbons printed onto rubber for flexible energy conversion," *Nano Letters*, vol. 10, no. 2, pp. 524–528, 2010.

[35] C. Dagdeviren, B. D. Yang, Y. Su, P. L. Tran, P. Joe, E. Anderson, J. Xia, V. Doraiswamy, B. Dehdashti, and X. Feng, "Conformal piezoelectric energy harvesting and storage from motions of the heart, lung, and diaphragm," *Proceedings of the National Academy of Sciences*, vol. 111, no. 5, pp. 1927–1932, 2014.

[36] C. Dagdeviren, Y. Shi, P. Joe, R. Ghaffari, G. Balooch, K. Usgaonkar, O. Gur, P. L. Tran, J. R. Crosby, and M. Meyer, "Conformal piezoelectric systems for clinical and experimental characterization of soft tissue biomechanics," *Nature Materials*, vol. 14, no. 7, pp. 728–736, 2015.

[37] Z. L. Wang and J. Song, "Piezoelectric nanogenerators based on zinc oxide nanowire arrays," *Science*, vol. 312, no. 5771, p. 242, 2006.

[38] Y. Gao and Z. L. Wang, "Electrostatic potential in a bent piezoelectric nanowire. the fundamental theory of nanogenerator and nanopiezotronics," *Nano Letters*, vol. 7, no. 8, pp. 2499–2505, 2007.

[39] X. Wang, J. Song, J. Liu, and Z. L. Wang, "Direct-current nanogenerator driven by ultrasonic waves," *Science*, vol. 316, no. 5821, p. 102, 2007.

[40] J. Liu, P. Fei, J. Song, X. Wang, C. Lao, R. Tummala, and Z. L. Wang, "Carrier density and schottky barrier on the performance of dc nanogenerator," *Nano Letters*, vol. 8, no. 1, pp. 328–332, 2008.

[41] Y. Gao and Z. L. Wang, "Equilibrium potential of free charge carriers in a bent piezoelectric semiconductive nanowire," *Nano Letters*, vol. 9, no. 3, pp. 1103–1110, 2009.

[42] C. Falconi, G. Mantini, A. DAmico, and Z. L. Wang, "Studying piezoelectric nanowires and nanowalls for energy harvesting," *Sensors and Actuators B: Chemical*, vol. 139, no. 2, pp. 511–519, 2009.

[43] R. Yang, Y. Qin, C. Li, G. Zhu, and Z. L. Wang, "Converting biomechanical energy into electricity by a muscle-movement-driven nanogenerator," *Nano Letters*, vol. 9, no. 3, pp. 1201–1205, 2009.

[44] S. Xu, Y. Qin, C. Xu, Y. Wei, R. Yang, and Z. L. Wang, "Self-powered nanowire devices," *Nature Nanotechnology*, vol. 5, no. 5, pp. 366–373, 2010.

[45] P. X. Gao, J. Song, J. Liu, and Z. L. Wang, "Nanowire piezoelectric nanogenerators on plastic substrates as flexible power sources for nanodevices," *Advanced Materials*, vol. 19, no. 1, pp. 67–72, 2007.

[46] S. Xu, Y. Wei, J. Liu, R. Yang, and Z. L. Wang, "Integrated multilayer nanogenerator fabricated using paired nanotip-to-nanowire brushes," *Nano Letters*, vol. 8, no. 11, pp. 4027–4032, 2008.

[47] G. Zhu, A. C. Wang, Y. Liu, Y. Zhou, and Z. L. Wang, "Functional electrical stimulation by nanogenerator with 58 V output voltage," *Nano Letters*, vol. 12, no. 6, pp. 3086–3090, 2012.

[48] K. C. Pradel, W. Wu, Y. Ding, and Z. L. Wang, "Solution-derived ZnO homojunction nanowire films on wearable substrates for energy conversion and self-powered gesture recognition," *Nano Letters*, vol. 14, no. 12, pp. 6897–6905, 2014.

[49] M. Lee, C.-Y. Chen, S. Wang, S. N. Cha, Y. J. Park, J. M. Kim, L.-J. Chou, and Z. L. Wang, "A hybrid piezoelectric structure for wearable nanogenerators," *Advanced Materials*, vol. 24, no. 13, pp. 1759–1764, 2012.

[50] N. Jackson, L. Keeney, and A. Mathewson, "Flexible-CMOS and biocompatible piezoelectric AlN material for MEMS applications," *Smart Materials and Structures*, vol. 22, no. 11, p. 115033, 2013.

[51] M. Akiyama, Y. Morofuji, T. Kamohara, K. Nishikubo, Y. Ooishi, M. Tsubai, O. Fukuda, and N. Ueno, "Preparation of oriented aluminum nitride thin films on polyimide films and piezoelectric response with high thermal stability and flexibility," *Advanced Functional Materials*, vol. 17, no. 3, pp. 458–462, 2007.

[52] S. Petroni, G. Maruccio, F. Guido, M. Amato, A. Campa, A. Passaseo, M. T. Todaro, and M. De Vittorio, "Flexible piezoelectric cantilevers fabricated on polyimide substrate," *Microelectronic Engineering*, vol. 98, pp. 603–606, 2012.

[53] S. Petroni, F. Rizzi, F. Guido, A. Cannavale, T. Donateo, F. Ingrosso, V. M. Mastronardi, R. Cingolani, and M. De Vittorio, "Flexible aln flags for efficient wind energy harvesting at ultralow cut-in wind speed," *RSC Advances*, vol. 5, no. 18, pp. 14047–14052, 2015.

[54] K. S. Ramadan, D. Sameoto, and S. Evoy, "A review of piezoelectric polymers as functional materials for electromechanical transducers," *Smart Materials and Structures*, vol. 23, no. 3, p. 033001, 2014.

[55] S. Li, J. Yuan, and H. Lipson, "Ambient wind energy harvesting using cross-flow fluttering," *Journal of Applied Physics*, vol. 109, no. 2, p. 026104, 2011.

[56] J. Fang, H. Niu, H. Wang, X. Wang, and T. Lin, "Enhanced mechanical energy harvesting using needleless electrospun poly (vinylidene fluoride) nanofibre webs," *Energy & Environmental Science*, vol. 6, no. 7, pp. 2196–2202, 2013.

[57] K.-I. Park, M. Lee, Y. Liu, S. Moon, G.-T. Hwang, G. Zhu, J. E. Kim, S. O. Kim, D. K. Kim, Z. L. Wang, *et al.*, "Flexible nanocomposite generator made of BaTiO3 nanoparticles and graphitic carbons," *Advanced Materials*, vol. 24, no. 22, pp. 2999–3004, 2012.

[58] J. Hillenbrand and G. M. Sessler, "Quasistatic and dynamic piezoelectric coefficients of polymer foams and polymer film systems," *IEEE Transactions on Dielectrics and Electrical Insulation*, vol. 11, no. 1, pp. 72–79, 2004.

[59] J.-J. Wang, T.-H. Hsu, C.-N. Yeh, J.-W. Tsai, and Y.-C. Su, "Piezoelectric polydimethylsiloxane films for MEMS transducers," *Journal of Micromechanics and Microengineering*, vol. 22, no. 1, p. 015013, 2011.

[60] Y. Feng, K. Hagiwara, Y. Iguchi, and Y. Suzuki, "Trench-filled cellular parylene electret for piezoelectric transducer," *Applied Physics Letters*, vol. 100, no. 26, p. 262901, 2012.

[61] R. G. Horn and D. T. Smith, "Contact electrification and adhesion between dissimilar materials," *Science*, vol. 256, no. 5055, p. 362, 1992.

[62] R. G. Horn, D. T. Smith, and A. Grabbe, "Contact electrification induced by monolayer modification of a surface and relation to acid-base interactions," *Nature*, vol. 366, pp. 442–443, 1993.

[63] F.-R. Fan, Z.-Q. Tian, and Z. L. Wang, "Flexible triboelectric generator," *Nano Energy*, vol. 1, no. 2, pp. 328–334, 2012.

[64] Z. L. Wang, J. Chen, and L. Lin, "Progress in triboelectric nanogenerators as a new energy technology and self-powered sensors," *Energy & Environmental Science*, vol. 8, no. 8, pp. 2250–2282, 2015.

[65] Z. L. Wang, "Triboelectric nanogenerators as new energy technology for self-powered systems and as active mechanical and chemical sensors," *ACS Nano*, vol. 7, no. 11, pp. 9533–9557, 2013.

[66] Z. L. Wang, "Triboelectric nanogenerators as new energy technology and self-powered sensorscprinciples, problems and perspectives," *Faraday Discussions*, vol. 176, pp. 447–458, 2014.

[67] S. Wang, L. Lin, and Z. L. Wang, "Nanoscale triboelectric-effect-enabled energy conversion for sustainably powering portable electronics," *Nano Letters*, vol. 12, no. 12, pp. 6339–6346, 2012.

[68] G. Zhu, Z.-H. Lin, Q. Jing, P. Bai, C. Pan, Y. Yang, Y. Zhou, and Z. L. Wang, "Toward large-scale energy harvesting by a nanoparticle-enhanced triboelectric nanogenerator," *Nano Letters*, vol. 13, no. 2, pp. 847–853, 2013.

[69] G. Zhu, C. Pan, W. Guo, C.-Y. Chen, Y. Zhou, R. Yu, and Z. L. Wang, "Triboelectric-generator-driven pulse electrodeposition for micropatterning," *Nano Letters*, vol. 12, no. 9, pp. 4960–4965, 2012.

[70] S. Wang, L. Lin, Y. Xie, Q. Jing, S. Niu, and Z. L. Wang, "Sliding-triboelectric nanogenerators based on in-plane charge-separation mechanism," *Nano Letters*, vol. 13, no. 5, pp. 2226–2233, 2013.

[71] G. Zhu, J. Chen, Y. Liu, P. Bai, Y. S. Zhou, Q. Jing, C. Pan, and Z. L. Wang, "Linear-grating triboelectric generator based on sliding electrification," *Nano Letters*, vol. 13, no. 5, pp. 2282–2289, 2013.

[72] Y. Yang, H. Zhang, J. Chen, Q. Jing, Y. S. Zhou, X. Wen, and Z. L. Wang, "Single-electrode-based sliding triboelectric nanogenerator for self-powered displacement vector sensor system," *ACS Nano*, vol. 7, no. 8, pp. 7342–7351, 2013.

[73] Y. Yang, Y. S. Zhou, H. Zhang, Y. Liu, S. Lee, and Z. L. Wang, "A single-electrode based triboelectric nanogenerator as self-powered tracking system," *Advanced Materials*, vol. 25, no. 45, pp. 6594–6601, 2013.

[74] S. Wang, Y. Xie, S. Niu, L. Lin, and Z. L. Wang, "Freestanding triboelectric-layer-based nanogenerators for harvesting energy from a moving object or human motion in contact and non-contact modes," *Advanced Materials*, vol. 26, no. 18, pp. 2818–2824, 2014.

[75] G. Piazza, V. Felmetsger, P. Muralt, R. H. Olsson Iii, and R. Ruby, "Piezoelectric aluminum nitride thin films for microelectromechanical systems," *MRS bulletin*, vol. 37, no. 11, pp. 1051–1061, 2012.

[76] G. Piazza, P. J. Stephanou, and A. P. Pisano, "Piezoelectric aluminum nitride vibrating contour-mode MEMS resonators," *Journal of Microelectromechanical Systems*, vol. 15, no. 6, pp. 1406–1418, 2006.

[77] R. C. Ruby, P. Bradley, Y. Oshmyansky, A. Chien, and J. D. Larson, "Thin film bulk wave acoustic resonators (FBAR) for wireless applications," vol. 1, pp. 813–821, IEEE.

[78] B. P. Harrington and R. Abdolvand, "In-plane acoustic reflectors for reducing effective anchor loss in lateral – extensional MEMS resonators," *Journal of Micromechanics and Microengineering*, vol. 21, no. 8, p. 085021, 2011.

[79] J. Bjurstr?m, I. Katardjiev, and V. Yantchev, "Lateral-field-excited thin-film lamb wave resonator," *Applied Physics Letters*, vol. 86, no. 15, p. 4103, 2005.

[80] C. Zuo, N. Sinha, and G. Piazza, "Very high frequency channel-select MEMS filters based on self-coupled piezoelectric aln contour-mode resonators," *Sensors and Actuators A: Physical*, vol. 160, no. 1, pp. 132–140, 2010.

[81] M. Rinaldi, C. Zuniga, C. Zuo, and G. Piazza, "Super-high-frequency two-port aln contour-mode resonators for rf applications," *IEEE Transactions on Ultrasonics, Ferroelectrics, and Frequency Control*, vol. 57, no. 1, pp. 38–45, 2010.

[82] J. M. Rabaey, J. Ammer, T. Karalar, S. Li, B. Otis, M. Sheets, and T. Tuan, "Picoradios for wireless sensor networks: the next challenge in ultra-low power design," vol. 1, pp. 200–201, IEEE.

[83] R. Mahameed, N. Sinha, M. B. Pisani, and G. Piazza, "Dual-beam actuation of piezoelectric AlN RF MEMS switches monolithically integrated with AlN contour-mode resonators," *Journal of Micromechanics and Microengineering*, vol. 18, no. 10, p. 105011, 2008.

[84] N. Sinha, G. E. Wabiszewski, R. Mahameed, V. V. Felmetsger, S. M. Tanner, and R. W. Carpick, "Piezoelectric aluminum nitride nanoelectromechanical actuators," *Departmental Papers (MEAM)*, p. 165, 2009.

[85] N. Sinha, T. S. Jones, Z. Guo, and G. Piazza, "Body-biased complementary logic implemented using aln piezoelectric MEMS switches," *Journal of Microelectromechanical Systems*, vol. 21, no. 2, pp. 484–496, 2012.

[86] R. Elfrink, T. M. Kamel, M. Goedbloed, S. Matova, D. Hohlfeld, Y. Van Andel, and R. Van Schaijk, "Vibration energy harvesting with aluminum nitride-based piezoelectric devices," *Journal of Micromechanics and Microengineering*, vol. 19, no. 9, p. 094005, 2009.

[87] R. Elfrink, M. Renaud, T. M. Kamel, C. De Nooijer, M. Jambunathan, M. Goedbloed, D. Hohlfeld, S. Matova, V. Pop, and L. Caballero, "Vacuum-packaged piezoelectric vibration energy harvesters: damping contributions and autonomy for a wireless sensor system," *Journal of Micromechanics and Microengineering*, vol. 20, no. 10, p. 104001, 2010.

[88] T.-T. Yen, T. Hirasawa, P. K. Wright, A. P. Pisano, and L. Lin, "Corrugated aluminum nitride energy harvesters for high energy conversion effectiveness," *Journal of Micromechanics and Microengineering*, vol. 21, no. 8, p. 085037, 2011.

[89] A. Guedes, S. Shelton, R. Przybyla, I. Izyumin, B. Boser, and D. A. Horsley, "Aluminum nitride pmut based on a flexurally-suspended membrane," pp. 2062–2065, IEEE.

[90] S. Shelton, M.-L. Chan, H. Park, D. Horsley, B. Boser, I. Izyumin, R. Przybyla, T. Frey, M. Judy, and K. Nunan, "Cmos-compatible aln piezoelectric micromachined ultrasonic transducers," pp. 402–405, IEEE.

[91] R. Littrell and K. Grosh, "Modeling and characterization of cantilever-based MEMS piezoelectric sensors and actuators," *Journal of Microelectromechanical Systems*, vol. 21, no. 2, pp. 406–413, 2012.

[92] M. D. Williams, B. A. Griffin, T. N. Reagan, J. R. Underbrink, and M. Sheplak, "An aln MEMS piezoelectric microphone for aeroacoustic applications," *Journal of Microelectromechanical Systems*, vol. 21, no. 2, pp. 270–283, 2012.

[93] F. T. Goericke, M. W. Chan, G. Vigevani, I. Izyumin, B. E. Boser, and A. P. Pisano, "High temperature compatible aluminum nitride resonating strain sensor," pp. 1994–1997, IEEE.

[94] C. Zuniga, M. Rinaldi, S. M. Khamis, A. T. Johnson, and G. Piazza, "Nanoenabled microelectromechanical sensor for volatile organic chemical detection," *Applied Physics Letters*, vol. 94, no. 22, p. 223122, 2009.

[95] T. W. Grudkowski, J. F. Black, T. M. Reeder, D. E. Cullen, and R. A. Wagner, "Fundamental-mode vhf/uhf minature acoustic resonators and filters on silicon," *Applied Physics Letters*, vol. 37, no. 11, pp. 993–995, 1980.

[96] J. G. Rodriguez-Madrid, G. F. Iriarte, O. A. Williams, and F. Calle, "High precision pressure sensors based on saw devices in the ghz range," *Sensors and Actuators A: Physical*, vol. 189, pp. 364–369, 2013.

[97] A. Qualtieri, F. Rizzi, M. T. Todaro, A. Passaseo, R. Cingolani, and M. De Vittorio, "Stress-driven aln cantilever-based flow sensor for fish lateral line system," *Microelectronic Engineering*, vol. 88, no. 8, pp. 2376–2378, 2011.

[98] E. Kim, Y.-K. Choi, J. Song, and J. Lee, "Detection of various self-assembled monolayers by aln-based film bulk acoustic resonator," *Materials Research Bulletin*, vol. 48, no. 12, pp. 5076–5079, 2013.

[99] R. Eason, *Pulsed laser deposition of thin films: applications-led growth of functional materials*. John Wiley & Sons, 2007.

[100] H. N. Krogstad, "Deposition of thin film electrolyte by pulsed laser deposition (PLD) for micro-sofc development," *Master's thesis, Institutt for materialteknologi*, 2012.

[101] J. Zhang, E. Merced, N. Sepulveda, and X. Tan, "Modeling and inverse compensation of hysteresis in vanadium dioxide using an extended generalized prandtlcishlinskii model," *Smart Materials and Structures*, vol. 23, no. 12, p. 125017, 2014.

[102] R. Cabrera, E. Merced, and N. Sepulveda, "Performance of electro-thermally driven-based MEMS actuators," *Journal of Microelectromechanical Systems*, vol. 23, no. 1, pp. 243–251, 2014.

[103] D. Torres, T. Wang, J. Zhang, X. Zhang, S. Dooley, X. Tan, H. Xie, and N. Sepulveda, "Vo¡sub¿2¡/sub¿-based MEMS mirrors," *Journal of Microelectromechanical Systems*, vol. 25, no. 4, pp. 780–787, 2016.

[104] I. Petrov, P. B. Barna, L. Hultman, and J. E. Greene, "Microstructural evolution during film growth," *Journal of Vacuum Science & Technology A*, vol. 21, no. 5, pp. S117–S128, 2003.

[105] J. Greer, "Large-area commercial pulsed laser deposition," *Pulsed Laser Deposition of Thin Films: Applications-Led Growth of Functional Materials*, pp. 191–213, 2006.

[106] H.-U. Krebs, M. Weisheit, J. Faupel, E. Sske, T. Scharf, C. Fuhse, M. St?rmer, K. Sturm, M. Seibt, and H. Kijewski, *Pulsed Laser Deposition (PLD)–A Versatile Thin Film Technique*, pp. 505–518. Springer, 2003.

[107] M.-H. Zhao, Z.-L. Wang, and S. X. Mao, "Piezoelectric characterization of individual zinc oxide nanobelt probed by piezoresponse force microscope," *Nano Letters*, vol. 4, no. 4, pp. 587–590, 2004.

[108] K. Lefki and G. Dormans, "Measurement of piezoelectric coefficients of ferroelectric thin films," *Journal of Applied Physics*, vol. 76, no. 3, pp. 1764–1767, 1994.

[109] K. Tonisch, V. Cimalla, C. Foerster, H. Romanus, O. Ambacher, and D. Dontsov, "Piezoelectric properties of polycrystalline aln thin films for MEMS application," *Sensors and Actuators A: Physical*, vol. 132, no. 2, pp. 658–663, 2006.

[110] K. Tonisch, V. Cimalla, C. Foerster, H. Romanus, O. Ambacher, and D. Dontsov, "Piezoelectric properties of polycrystalline aln thin films for MEMS application," *Sensors and Actuators A: Physical*, vol. 132, no. 2, pp. 658–663, 2006.

[111] M.-A. Dubois and P. Muralt, "Properties of aluminum nitride thin films for piezoelectric transducers and microwave filter applications," *Applied Physics Letters*, vol. 74, no. 20, pp. 3032–3034, 1999.

[112] V. Mortet, M. Nesladek, K. Haenen, A. Morel, M. D'Olieslaeger, and M. Vanecek, "Physical properties of polycrystalline aluminium nitride films deposited by magnetron sputtering," *Diamond and related materials*, vol. 13, no. 4, pp. 1120–1124, 2004.

[113] J. G. Gualtieri, J. A. Kosinski, and A. Ballato, "Piezoelectric materials for acoustic wave applications," *IEEE Transactions on Ultrasonics, Ferroelectrics, and Frequency Control*, vol. 41, no. 1, pp. 53–59, 1994.

[114] J. Christman, H. Maiwa, S.-H. Kim, A. Kingon, and R. Nemanich, "Piezoelectric measurements with atomic force microscopy," in *MRS Proceedings*, vol. 541, p. 617, Cambridge Univ Press, 1998.

[115] K. Ellmer, A. Klein, and B. Rech, *Transparent conductive zinc oxide: basics and applications in thin film solar cells*, vol. 104. Springer Science & Business Media, 2007.

[116] C. Cibert, P. Dutheil, C. Champeaux, O. Masson, G. Trolliard, F. Ttard, and A. Catherinot, "Piezoelectric characteristic of nanocrystalline aln films obtained by pulsed laser deposition at room temperature," *Applied Physics Letters*, vol. 97, no. 25, p. 251906, 2010.

[117] E. Lee, J. Park, M. Yim, Y. Kim, and G. Yoon, "Characteristics of piezoelectric ZnO/AlN-stacked flexible nanogenerators for energy harvesting applications," *Applied Physics Letters*, vol. 106, no. 2, p. 023901, 2015.

[118] X. Pu, L. Li, M. Liu, C. Jiang, C. Du, Z. Zhao, W. Hu, and Z. L. Wang, "Wearable self-charging power textile based on flexible yarn supercapacitors and fabric nanogenerators," *Advanced Materials*, vol. 28, no. 1, pp. 98–105, 2016.

[119] T. Zhou, C. Zhang, C. B. Han, F. R. Fan, W. Tang, and Z. L. Wang, "Woven structured triboelectric nanogenerator for wearable devices," *ACS applied materials & interfaces*, vol. 6, no. 16, pp. 14695–14701, 2014.

[120] C. K. Jeong, J. Lee, S. Han, J. Ryu, G.-T. Hwang, D. Y. Park, J. H. Park, S. S. Lee, M. Byun, and S. H. Ko, "A hyper-stretchable elastic-composite energy harvester," *Advanced Materials*, vol. 27, no. 18, pp. 2866–2875, 2015.

[121] G.-T. Hwang, J. Yang, S. H. Yang, H.-Y. Lee, M. Lee, D. Y. Park, J. H. Han, S. J. Lee, C. K. Jeong, and J. Kim, "A reconfigurable rectified flexible energy harvester via solid-state single crystal grown PMN-PZT," *Advanced Energy Materials*, vol. 5, no. 10, p. 1500051, 2015.

[122] K.-I. Park, J. H. Son, G.-T. Hwang, C. K. Jeong, J. Ryu, M. Koo, I. Choi, S. H. Lee, M. Byun, and Z. L. Wang, "Highly-efficient, flexible piezoelectric PZT thin film nanogenerator on plastic substrates," *Advanced Materials*, vol. 26, no. 16, pp. 2514–2520, 2014.

[123] G.-T. Hwang, Y. Kim, J.-H. Lee, S. Oh, C. K. Jeong, D. Y. Park, J. Ryu, H. Kwon, S.-G. Lee, and B. Joung, "Self-powered deep brain stimulation via a flexible pimnt energy harvester," *Energy & Environmental Science*, vol. 8, no. 9, pp. 2677–2684, 2015.

[124] C. Wang, D. Hwang, Z. Yu, K. Takei, J. Park, T. Chen, B. Ma, and A. Javey, "User-interactive electronic skin for instantaneous pressure visualization," *Nature Materials*, vol. 12, no. 10, pp. 899–904, 2013.

[125] C. Wang, K. Takei, T. Takahashi, and A. Javey, "Carbon nanotube electronics?moving forward," *Chemical Society Reviews*, vol. 42, no. 7, pp. 2592–2609, 2013.

[126] L. Cai, S. Zhang, J. Miao, Z. Yu, and C. Wang, "Fully printed foldable integrated logic gates with tunable performance using semiconducting carbon nanotubes," *Advanced Functional Materials*, vol. 25, no. 35, pp. 5698–5705, 2015.

[127] C. Wang, J.-C. Chien, K. Takei, T. Takahashi, J. Nah, A. M. Niknejad, and A. Javey, "Extremely bendable, high-performance integrated circuits using semiconducting carbon nanotube networks for digital, analog, and radio-frequency applications," *Nano Letters*, vol. 12, no. 3, pp. 1527–1533, 2012.

[128] J. Zhang, C. Wang, and C. Zhou, "Rigid/flexible transparent electronics based on separated carbon nanotube thin-film transistors and their application in display electronics," *ACS Nano*, vol. 6, no. 8, pp. 7412–7419, 2012.

[129] T. Takahashi, Z. Yu, K. Chen, D. Kiriya, C. Wang, K. Takei, H. Shiraki, T. Chen, B. Ma, and A. Javey, "Carbon nanotube active-matrix backplanes for mechanically flexible visible light and x-ray imagers," *Nano Letters*, vol. 13, no. 11, pp. 5425–5430, 2013.

[130] X. Pu, L. Li, H. Song, C. Du, Z. Zhao, C. Jiang, G. Cao, W. Hu, and Z. L. Wang, "A self-charging power unit by integration of a textile triboelectric nanogenerator and a flexible lithium-ion battery for wearable electronics," *Advanced Materials*, vol. 27, no. 15, pp. 2472–2478, 2015.

[131] G.-T. Hwang, H. Park, J.-H. Lee, S. Oh, K.-I. Park, M. Byun, H. Park, G. Ahn, C. K. Jeong, and K. No, "Self-powered cardiac pacemaker enabled by flexible single crystalline PMN-PT piezoelectric energy harvester," *Advanced Materials*, vol. 26, no. 28, pp. 4880–4887, 2014.

[132] C. K. Jeong, K.-I. Park, J. H. Son, G.-T. Hwang, S. H. Lee, D. Y. Park, H. E. Lee, H. K. Lee, M. Byun, and K. J. Lee, "Self-powered fully-flexible light-emitting system enabled by flexible energy harvester," *Energy & Environmental Science*, vol. 7, no. 12, pp. 4035–4043, 2014.

[133] S. Kim, J. H. Son, S. H. Lee, B. K. You, K.-I. Park, H. K. Lee, M. Byun, and K. J. Lee, "Flexible crossbar-structured resistive memory arrays on plastic substrates via inorganic-based laser lift-off," *Advanced Materials*, vol. 26, no. 44, pp. 7480–7487, 2014.

[134] C.-H. Wang, W.-S. Liao, Z.-H. Lin, N.-J. Ku, Y.-C. Li, Y.-C. Chen, Z.-L. Wang, and C.-P. Liu, "Optimization of the output efficiency of gan nanowire piezoelectric nanogenerators by tuning the free carrier concentration," *Advanced Energy Materials*, vol. 4, no. 16, p. 1400392, 2014.

[135] W. Wu, L. Wang, Y. Li, F. Zhang, L. Lin, S. Niu, D. Chenet, X. Zhang, Y. Hao, and T. F. Heinz, "Piezoelectricity of single-atomic-layer MoS_2 for energy conversion and piezotronics," *Nature*, vol. 514, no. 7523, pp. 470–474, 2014.

[136] S. Xu, Y. Qin, C. Xu, Y. Wei, R. Yang, and Z. L. Wang, "Self-powered nanowire devices," *Nature Nanotechnology*, vol. 5, no. 5, pp. 366–373, 2010.

[137] J. Chen, G. Zhu, W. Yang, Q. Jing, P. Bai, Y. Yang, T.-C. Hou, and Z. L. Wang, "Harmonic-resonator-based triboelectric nanogenerator as a sustainable power source and a self-powered active vibration sensor," *Advanced Materials*, vol. 25, no. 42, pp. 6094–6099, 2013.

[138] Y. S. Zhou, G. Zhu, S. Niu, Y. Liu, P. Bai, Q. Jing, and Z. L. Wang, "Nanometer resolution self-powered static and dynamic motion sensor based on micro-grated triboelectrification," *Advanced Materials*, vol. 26, no. 11, pp. 1719–1724, 2014.

[139] Z. Lin Wang, "Triboelectric nanogenerators as new energy technology and self-powered sensors-principles, problems and perspectives," *Faraday discussions*, vol. 176, pp. 447–458, 2014.

[140] X. Li, Z.-H. Lin, G. Cheng, X. Wen, Y. Liu, S. Niu, and Z. L. Wang, "3d fiber-based hybrid nanogenerator for energy harvesting and as a self-powered pressure sensor," *ACS Nano*, vol. 8, no. 10, pp. 10674–10681, 2014.

[141] K.-I. Park, C. K. Jeong, J. Ryu, G.-T. Hwang, and K. J. Lee, "Flexible and large-area nanocomposite generators based on lead zirconate titanate particles and carbon nanotubes," *Advanced Energy Materials*, vol. 3, no. 12, pp. 1539–1544, 2013.

[142] H.-J. Kim, J.-H. Kim, K.-W. Jun, J.-H. Kim, W.-C. Seung, O. H. Kwon, J.-Y. Park, S.-W. Kim, and I.-K. Oh, "Silk nanofiber-networked bio-triboelectric generator: Silk Bio-TEG," *Advanced Energy Materials*, vol. 6, no. 8, 2016. 1502329.

[143] M. Wegener and S. Bauer, "Microstorms in cellular polymers: A route to soft piezoelectric transducer materials with engineered macroscopic dipoles," *ChemPhysChem*, vol. 6, no. 6, pp. 1014–1025, 2005.

[144] S. Bauer, R. Gerhard-Multhaupt, and G. M. Sessler, "Ferroelectrets: Soft electroactive foams for transducers," *Physics Today*, vol. 57, no. 2, pp. 37–44, 2004.

[145] J. Dring, V. Bovtun, M. Gaal, J. Bartusch, A. Erhard, M. Kreutzbruck, and Y. Yakymenko, "Piezoelectric and electrostrictive effects in ferroelectret ultrasonic transducers," *Journal of Applied Physics*, vol. 112, no. 8, p. 084505, 2012.

[146] Z. Luo, D. Zhu, J. Shi, S. Beeby, C. Zhang, P. Proynov, and B. Stark, "Energy harvesting study on single and multilayer ferroelectret foams under compressive force," *IEEE Transactions on Dielectrics and Electrical Insulation*, vol. 22, no. 3, pp. 1360–1368, 2015.

[147] K.-I. Park, M. Lee, Y. Liu, S. Moon, G.-T. Hwang, G. Zhu, J. E. Kim, S. O. Kim, D. K. Kim, and Z. L. Wang, "Flexible nanocomposite generator made of $Batio_3$ nanoparticles and graphitic carbons," *Advanced Materials*, vol. 24, no. 22, pp. 2999–3004, 2012.

[148] K. S. Ramadan, D. Sameoto, and S. Evoy, "A review of piezoelectric polymers as functional materials for electromechanical transducers," *Smart Materials and Structures*, vol. 23, no. 3, p. 033001, 2014.

[149] F.-C. Sun, A. M. Dongare, A. D. Asandei, S. P. Alpay, and S. Nakhmanson, "Temperature dependent structural, elastic, and polar properties of ferroelectric polyvinylidene fluoride (PVDF) and trifluoroethylene (TrFE) copolymers," *Journal of Materials Chemistry C*, vol. 3, no. 32, pp. 8389–8396, 2015.

[150] Z. Liu, C. Pan, L. Lin, J. Huang, and Z. Ou, "Direct-write pvdf nonwoven fiber fabric energy harvesters via the hollow cylindrical near-field electrospinning process," *Smart Materials and Structures*, vol. 23, no. 2, p. 025003, 2013.

[151] P. Pondrom, J. Hillenbrand, G. M. Sessler, J. Bos, and T. Melz, "Energy harvesting with single-layer and stacked piezoelectret films," *IEEE Transactions on Dielectrics and Electrical Insulation*, vol. 22, no. 3, pp. 1470–1476, 2015.

[152] Y. Feng, K. Hagiwara, Y. Iguchi, and Y. Suzuki, "Trench-filled cellular parylene electret for piezoelectric transducer," *Applied Physics Letters*, vol. 100, no. 26, p. 262901, 2012.

[153] J.-J. Wang, T.-H. Hsu, C.-N. Yeh, J.-W. Tsai, and Y.-C. Su, "Piezoelectric polydimethylsiloxane films for MEMS transducers," *Journal of Micromechanics and Microengineering*, vol. 22, no. 1, p. 015013, 2011.

[154] R. Yang, Y. Qin, L. Dai, and Z. L. Wang, "Power generation with laterally packaged piezoelectric fine wires," *Nature Nanotechnology*, vol. 4, no. 1, pp. 34–39, 2009.

[155] J. Wang, S. Li, F. Yi, Y. Zi, J. Lin, X. Wang, Y. Xu, and Z. L. Wang, "Sustainably powering wearable electronics solely by biomechanical energy," *Nature Communications*, vol. 7, p. 12744, 2016.

[156] X. Pu, L. Li, M. Liu, C. Jiang, C. Du, Z. Zhao, W. Hu, and Z. L. Wang, "Wearable self-charging power textile based on flexible yarn supercapacitors and fabric nanogenerators," *Advanced Materials*, vol. 28, no. 1, pp. 98–105, 2016.

[157] S. Niu, X. Wang, F. Yi, Y. S. Zhou, and Z. L. Wang, "A universal self-charging system driven by random biomechanical energy for sustainable operation of mobile electronics," *Nature Communications*, vol. 6, p. 8975, 2015.

[158] C. K. Jeong, J. Lee, S. Han, J. Ryu, G.-T. Hwang, D. Y. Park, J. H. Park, S. S. Lee, M. Byun, S. H. Ko, *et al.*, "A hyper-stretchable elastic-composite energy harvester," *Adv. Mater.*, vol. 27, no. 18, pp. 2866–2875, 2015.

[159] J. Chun, B. U. Ye, J. W. Lee, D. Choi, C.-Y. Kang, S.-W. Kim, Z. L. Wang, and J. M. Baik, "Boosted output performance of triboelectric nanogenerator via electric double layer effect," *Nature Communications*, vol. 7, p. 12985, 2016.

[160] Q. Jing, Y. Xie, G. Zhu, R. P. S. Han, and Z. L. Wang, "Self-powered thin-film motion vector sensor," *Nature Communications*, vol. 6, p. 8031, 2015.

[161] T. Zhou, C. Zhang, C. B. Han, F. R. Fan, W. Tang, and Z. L. Wang, "Woven structured triboelectric nanogenerator for wearable devices," *ACS Applied Materials & Interfaces*, vol. 6, no. 16, pp. 14695–14701, 2014.

[162] K.-I. Park, J. H. Son, G.-T. Hwang, C. K. Jeong, J. Ryu, M. Koo, I. Choi, S. H. Lee, M. Byun, Z. L. Wang, *et al.*, "Highly-efficient, flexible piezoelectric pzt thin film nanogenerator on plastic substrates," *Advanced Materials*, vol. 26, no. 16, pp. 2514–2520, 2014.

[163] G. Zhu, J. Chen, T. Zhang, Q. Jing, and Z. L. Wang, "Radial-arrayed rotary electrification for high performance triboelectric generator," *Nature Communications*, vol. 5, p. 3426, 2014.

[164] G.-T. Hwang, Y. Kim, J.-H. Lee, S. Oh, C. K. Jeong, D. Y. Park, J. Ryu, H. Kwon, S.-G. Lee, B. Joung, *et al.*, "Self-powered deep brain stimulation via a flexible pimnt energy harvester," *Energy & Environmental Science*, vol. 8, no. 9, pp. 2677–2684, 2015.

[165] Z. Wang, R. Yu, C. Pan, Z. Li, J. Yang, F. Yi, and Z. L. Wang, "Light-induced pyroelectric effect as an effective approach for ultrafast ultraviolet nanosensing," *Nature Communications*, vol. 6, p. 8401, 2015.

[166] G.-T. Hwang, J. Yang, S. H. Yang, H.-Y. Lee, M. Lee, D. Y. Park, J. H. Han, S. J. Lee, C. K. Jeong, J. Kim, K.-I. Park, and K. J. Lee, "A reconfigurable rectified flexible energy harvester via solid-state single crystal grown PMN?PZT," *Advanced Energy Materials*, vol. 5, no. 10, p. 1500051, 2015.

[167] X. Pu, L. Li, H. Song, C. Du, Z. Zhao, C. Jiang, G. Cao, W. Hu, and Z. L. Wang, "A self-charging power unit by integration of a textile triboelectric nanogenerator and a flexible lithium-ion battery for wearable electronics," *Advanced Materials*, vol. 27, no. 15, pp. 2472–2478, 2015.

[168] K. S. Kim, Y. Zhao, H. Jang, S. Y. Lee, J. M. Kim, K. S. Kim, J.-H. Ahn, P. Kim, J.-Y. Choi, and B. H. Hong, "Large-scale pattern growth of graphene films for stretchable transparent electrodes," *Nature*, vol. 457, no. 7230, pp. 706–710, 2009.

[169] Y. Chen, J. Au, P. Kazlas, A. Ritenour, H. Gates, and M. McCreary, "Electronic paper: Flexible active-matrix electronic ink display," *Nature*, vol. 423, no. 6936, pp. 136–136, 2003.

[170] K. Nomura, H. Ohta, A. Takagi, T. Kamiya, M. Hirano, and H. Hosono, "Room-temperature fabrication of transparent flexible thin-film transistors using amorphous oxide semiconductors," *Nature*, vol. 432, no. 7016, pp. 488–492, 2004.

[171] C. Wang, D. Hwang, Z. Yu, K. Takei, J. Park, T. Chen, B. Ma, and A. Javey, "User-interactive electronic skin for instantaneous pressure visualization," *Nature Materials*, vol. 12, no. 10, pp. 899–904, 2013.

[172] C. Wang, J.-C. Chien, K. Takei, T. Takahashi, J. Nah, A. M. Niknejad, and A. Javey, "Extremely bendable, high-performance integrated circuits using semiconducting carbon nanotube networks for digital, analog, and radio-frequency applications," *Nano Letters*, vol. 12, no. 3, pp. 1527–1533, 2012.

[173] R. J. Hamers, "Flexible electronic futures," *Nature*, vol. 412, no. 6846, pp. 489–490, 2001.

[174] J. Zhang, C. Wang, and C. Zhou, "Rigid/flexible transparent electronics based on separated carbon nanotube thin-film transistors and their application in display electronics," *ACS Nano*, vol. 6, no. 8, pp. 7412–7419, 2012.

[175] T. Takahashi, Z. Yu, K. Chen, D. Kiriya, C. Wang, K. Takei, H. Shiraki, T. Chen, B. Ma, and A. Javey, "Carbon nanotube active-matrix backplanes for mechanically flexible visible light and x-ray imagers," *Nano Letters*, vol. 13, no. 11, pp. 5425–5430, 2013.

[176] M. Serres, *The five senses: A philosophy of mingled bodies*. Bloomsbury Publishing, 2008.

[177] L. Xiao, Z. Chen, C. Feng, L. Liu, Z.-Q. Bai, Y. Wang, L. Qian, Y. Zhang, Q. Li, and K. Jiang, "Flexible, stretchable, transparent carbon nanotube thin film loudspeakers," *Nano Letters*, vol. 8, no. 12, pp. 4539–4545, 2008.

[178] J. Borwick, *Loudspeaker and Headphone Handbook*. CRC Press, 2012.

[179] H. Tian, T.-L. Ren, D. Xie, Y.-F. Wang, C.-J. Zhou, T.-T. Feng, D. Fu, Y. Yang, P.-G. Peng, L.-G. Wang, *et al.*, "Graphene-on-paper sound source devices," *ACS Nano*, vol. 5, no. 6, pp. 4878–4885, 2011.

[180] K. Jiang, J. Wang, Q. Li, L. Liu, C. Liu, and S. Fan, "Superaligned carbon nanotube arrays, films, and yarns: a road to applications," *Advanced Materials*, vol. 23, no. 9, pp. 1154–1161, 2011.

[181] M. F. De Volder, S. H. Tawfick, R. H. Baughman, and A. J. Hart, "Carbon nanotubes: present and future commercial applications," *Science*, vol. 339, no. 6119, pp. 535–539, 2013.

[182] X. Fan, J. Chen, J. Yang, P. Bai, Z. Li, and Z. L. Wang, "Ultrathin, rollable, paper-based triboelectric nanogenerator for acoustic energy harvesting and self-powered sound recording," *ACS Nano*, vol. 9, no. 4, pp. 4236–4243, 2015.

[183] W. Li, D. Torres, T. Wang, C. Wang, and N. Seplveda, "Flexible and biocompatible polypropylene ferroelectret nanogenerator (FENG): On the path toward wearable devices powered by human motion," *Nano Energy*, vol. 30, pp. 649–657, 2016.

[184] D. Tripathi, *Practical Guide to Polypropylene*. iSmithers Rapra Publishing, 2002.

[185] C. Maier and T. Calafut, *Polypropylene: The Definitive User's Guide and Databook*. William Andrew, 1998.

[186] M. Wegener and S. Bauer, "Microstorms in cellular polymers: A route to soft piezoelectric transducer materials with engineered macroscopic dipoles," *Chemphyschem*, vol. 6, no. 6, pp. 1014–1025, 2005.

[187] M. Wegener, W. Wirges, R. Gerhard-Multhaupt, M. Dansachmüller, R. Schwödiauer, S. Bauer-Gogonea, S. Bauer, M. Paajanen, H. Minkkinen, and J. Raukola, "Controlled inflation of voids in cellular polymer ferroelectrets: Optimizing electromechanical transducer properties," *Applied Physics Letters*, vol. 84, no. 3, pp. 392–394, 2004.

[188] J. Dring, V. Bovtun, M. Gaal, J. Bartusch, A. Erhard, M. Kreutzbruck, and Y. Yakymenko, "Piezoelectric and electrostrictive effects in ferroelectret ultrasonic transducers," *Journal of Applied Physics*, vol. 112, no. 8, p. 084505, 2012.

[189] S. Rosen and P. Howell, *Signals and Systems for Speech and Hearing*, vol. 29. Brill, 2011.

[190] M. Schroeder, T. D. Rossing, F. Dunn, W. Hartmann, D. Campbell, and N. Fletcher, "Springer Handbook of Acoustics," 2007.

[191] G. M. Sessler and J. E. West, "Foil-electret microphones," *Journal of the Acoustical Society of America*, vol. 40, no. 6, pp. 1433–1440, 1966.

[192] J. Fraden, *Handbook of Modern Sensors*, vol. 3. Springer, 2010.

[193] J. Hillenbrand, S. Haberzettl, and G. Sessler, "Electret microphones with stiff diaphragms," *Journal of the Acoustical Society of America*, vol. 134, no. 6, pp. EL499–EL505, 2013.

[194] E. L. Salomons and P. J. Havinga, "A survey on the feasibility of sound classification on wireless sensor nodes," *Sensors*, vol. 15, no. 4, pp. 7462–7498, 2015.

[195] F. Richardson, D. Reynolds, and N. Dehak, "Deep neural network approaches to speaker and language recognition," *IEEE Signal Processing Letters*, vol. 22, no. 10, pp. 1671–1675, 2015.

[196] T. N. Sainath, B. Kingsbury, G. Saon, H. Soltau, A.-r. Mohamed, G. Dahl, and B. Ramabhadran, "Deep convolutional neural networks for large-scale speech tasks," *Neural Networks*, vol. 64, pp. 39–48, 2015.

[197] P. Sinha, "Recognizing complex patterns," *Nature Neuroscience*, vol. 5, pp. 1093–1097, 2002.

[198] K. Von Kriegstein, A. Kleinschmidt, P. Sterzer, and A.-L. Giraud, "Interaction of face and voice areas during speaker recognition," *Journal of Cognitive Neuroscience*, vol. 17, no. 3, pp. 367–376, 2005.

[199] A. Rúa, F. E. Fernández, and N. Sepúlveda, "Bending in vo 2-coated microcantilevers suitable for thermally activated actuators," *Journal of Applied Physics*, vol. 107, no. 7, p. 074506, 2010.

[200] R. Cabrera, E. Merced, and N. Sepúlveda, "Performance of electro-thermally driven vo2-based mems actuators," *Journal of Microelectromechanical Systems*, vol. 23, no. 1, pp. 243–251, 2014.

[201] Z. Zhang, K. Guo, Y. Li, X. Li, G. Guan, H. Li, Y. Luo, F. Zhao, Q. Zhang, B. Wei, *et al.*, "A colour-tunable, weavable fibre-shaped polymer light-emitting electrochemical cell," *Nature Photonics*, vol. 9, no. 4, pp. 233–238, 2015.